# Ultrafast Investigations of Exciton Dynamics in 0D and 2D Hybrid Semiconductor Nanomaterials

by

Eric R. Powers

B.S. Chemical and Biomolecular Engineering
Georgia Institute of Technology, 2013

Submitted to the Department of Chemical Engineering
in partial fulfillment of the requirements for the degree of

DOCTOR OF PHILOSOPHY IN CHEMICAL ENGINEERING
at the
MASSACHUSETTS INSTITUTE OF TECHNOLOGY

February 2023



Authored by:_____
Eric R. Powers
Department of Chemical Engineering
January 9, 2023

Certified by:_____
William A. Tisdale
Associate Professor of Chemical Engineering
Thesis Supervisor

Accepted by:_____
Patrick S. Doyle
Robert T. Haslam (1911) Professor of Chemical Engineering
Chairman, Committee for Graduate Students

# Ultrafast Investigations of Exciton Dynamics in 0D and 2D Hybrid Semiconductor Nanomaterials

by

Eric R. Powers

Submitted to the Department of Chemical Engineering on January 9, 2023 in partial fulfillment of the requirements for the degree of Doctor of Philosophy in Chemical Engineering

## Abstract

The development of hybrid organic-inorganic semiconductor nanomaterials represents a major advance towards highly tunable and efficient optoelectronic devices. These materials are comprised of multiple chemical constituents arranged in nanoscale geometries, and they exhibit emergent properties such as quantum confinement and enhanced Coulombic interactions. Photoactive nanomaterials have potential applications in lighting, solar, lasing, and quantum information. However, their complex chemistry and nanometer-scale dimensionality present a barrier to understanding and controlling their structure-function relationships. In this thesis, I utilize ultrafast pump-probe spectroscopy to study the fundamental properties of hybrid semiconductor nanomaterials. This technique allows the electronic and vibrational dynamics of these materials to be investigated with femtosecond time resolution, providing new insights into their underlying physics.

I first employ impulsive vibrational spectroscopy to study exciton-phonon interactions in silver phenyl selenolate (AgSePh), a recently discovered hybrid 2D semiconductor. Combining this time-domain Raman technique with frequency-domain non-resonant Raman scattering, I measure the vibrational landscape of the system and identify a subset of vibrational modes that couple strongly to excitonic transitions. Density functional theory calculations are then utilized to pinpoint specific atomic displacements which couple to the excitonic transition. An investigation of temperature-dependent photoluminescence reveals the connection between atomic scale dynamics and macroscopic properties, showing the 99 $cm^{-1}$ mode strongly impacts emission frequency and linewidth in AgSePh. Finally, temperature-dependent impulsive vibrational spectroscopy is employed to probe vibrational anharmonicity in this material. These findings provide a roadmap for controlling exciton-phonon coupling in hybrid organic-inorganic semiconductors.

Next, I study charging and neutralization processes in lead halide perovskite nanocrystals (quantum dots) with transient absorption spectroscopy. A temperature-dependent study of $CsPbBr_3$ nanocrystals reveals that charging occurs in a significant fraction of photoexcited nanocrystals (>10%), which then exhibit a microsecond neutralization lifetime at cryogenic temperatures. The temperature-dependent dynamics are modeled to extract a ~100 meV energy barrier to re-neutralization. Additionally, photocharging shows a sublinear fluence dependence, excluding Auger recombination as the initiator of this process, in contrast with traditional nanocrystal systems. These results help illuminate the underlying mechanism of charging in perovskite nanocrystals, guiding future synthetic advances to improve nanocrystal performance in lighting and quantum information applications.

Thesis Supervisor: William A. Tisdale
Title: Associate Professor of Chemical Engineering

# Acknowledgements

As I near the completion of my five-year journey to a PhD, there are so many people I want to thank for helping me get here today. First and foremost is my advisor, Will Tisdale, who has been constantly supportive of me throughout the ups and downs of my PhD. Will has been a great motivator because he is genuinely excited about science and is someone I know I can elicit a "Wow!" out of when I show him an unexpected result. He has taught me how to think like a scientist, back up every conclusion with data, and consider alternative explanations to the prevailing theory. At the same time, Will has shown that it's possible to be a great researcher and still have a personal life. He sets a great example of a healthy work-life balance and is always focused on the wellbeing of our group members. I also want to thank the other two members of my thesis committee, Professors Jeff Grossman and Bill Green, who have asked insightful questions during our meetings, helped keep me focused on the broader picture of my thesis, and offered to assist me in any way they could.

I also appreciate the role many current and former members of the Tisdale research group have played in my growth as a researcher and as a person during my PhD. In particular, I would like to thank Matt Ashner, who acted as my mentor when I first joined the group and taught me much of what I know about being an ultrafast spectroscopist. Kris Williams and Katie Shulenberger taught me how to approach a research project and think critically about the results. Oat Paritmongkol has been my collaborator on multiple successful projects and also set a great example of scientific excellence during our time working together. Nannan Mao, Chana Honick, and Narumi Wong have been my fellow Spirit laser users and are always willing to share equipment and help troubleshoot issues. Wenbi Shcherbakov-Wu has worked with me on several projects studying perovskite nanocrystals, but more importantly has been a close friend, confidant, and one-time engagement photographer. Finally, thanks to everyone else in the Tisdale group for creating an environment where we can learn from and support one another, including Katie Mauck, Dahin Kim, Liza Lee, Aaron Goodman, Nabeel Dahod, Sam Winslow, SK Ha, Ruomeng Wan, Woo Seok Lee, Abby Taussig, Eliza Price, Thomas Sheehan, Niamh Brown, Alexia Stollmann, Alex Hernandez Oendra, Makhsud Saidaminov, Tomoaki Sakurada, Fabio Marangi, and our course our wonderful group administrator Barb Balkwill.

Outside of research, I'm grateful to the friends I've made in my incoming cohort in the Chemical Engineering Department. In particular, I'd like to thank Sarah Cowles and Jennifer Kaczmarek for being such kind and supportive friends; Duncan Morgan, Kevin Tenny, and Natalie Eyke for helping me survive the first semester; and Ani Nambiar for being a great teammate and captain on the department cricket team.

Finally, I've been successful in graduate school thanks to the support of family and friends across the country. I would especially like to thank Sam Amoroso, Jay Schwarzhoff, and my uncle, Randy Duran, for their guidance and mentorship as I decided to pursue my PhD, selected what school to attend, and found the right research group for my interests. I've also really appreciated the support from my extended family living nearby in Gloucester and the Boston area, who have always been happy to host me and cheer me on through graduate school, especially my ever encouraging grandmother, Joan.

I want to thank my immediate family for helping me become the person I am today. To my sister, Danielle, thank you for paving the way for me growing up, always looking out for me, and constantly inspiring me with your passion for new challenges and adventures. To my parents, Jeff and Michele, thank you for being great role models to look up to and for supporting me no matter what I wanted to do in life (and for editing parts of my thesis).

My final (and most important) acknowledgement is to my wife Julia. Thank you for taking the leap and moving to Boston with me at the start of my PhD. Thank you for supporting me throughout grad school, especially the hardest months at the start and near the finish. Thank you for putting up with my quirks, teaching me to be a kinder person, and making our lives together so joyful.

# Contents

# List of Figures

**Chapter 1**



**Chapter 2**



**Chapter 3**

**Chapter 4**

**Chapter 5**

# List of Tables

**Chapter 3**

# Chapter 1
# Introduction to Hybrid Semiconductor Nanomaterials

> *Things on a very small scale behave like nothing that you have any direct experience about. They do not behave like waves, they do not behave like particles, they do not behave like clouds, or billiard balls, or weights on springs, or like anything that you have ever seen.*
>
> Richard Feynman, The Feynman Lectures on Physics, Volume III, Chapter 1[1]

## 1.1 Motivation

Devices that absorb or emit light make much of modern technology possible. From the display screens that inform and entertain us, to the solar panels that power our industries, to the emerging technologies—like augmented reality headsets—that may transform the future, optically active semiconductor devices are an integral part of our lives. Advances in these technologies are being driven by next-generation materials that exhibit a step change in performance over current devices. These emerging materials often involve multiple elements arranged in complex structures, mixtures of different classes of materials (such as organic and inorganic components), or nanoscale dimensionality. Their increased complexity allows these materials to be engineered with desirable characteristics like efficient light absorption, tunable emission, low-cost manufacturing, and many other useful properties. Next-generation materials have proven effective in a variety of device applications including solar panels[2–5], LEDs[6–9], lasers[7,10–12], photodetectors[13–15], and quantum emitters[16–18].

However, the complex structures of many next-generation materials make it difficult to understand the underlying physical processes that drive their unique properties, and often these processes do not mirror their simpler inorganic crystalline predecessors. In addition, many emerging semiconductors are nanomaterials, exhibiting structural features on a 1-100 nanometer scale in one or more dimensions[8,19]. Compared to bulk semiconductors—which normally have grain sizes and dimensions on the ~micrometer scale[20]—these nanocrystals are orders of

magnitude smaller, greatly increasing interfacial effects and leading to non-intuitive physical phenomena like quantum confinement. This nanometer-scale dimensionality impacts macroscopic optoelectronic properties, such as electronic transport[21–23], optical bandgap[24,25], and emission linewidth[26,27]. Developing a complete picture of nanomaterial physics and understanding how this impacts device-level performance presents a formidable challenge.

In this thesis, I will report on several investigations of emergent physical properties in semiconductor nanomaterials using ultrafast transient absorption spectroscopy in addition to other experimental and computational techniques. Through these studies, I am able to make connections between spectroscopic observations and their causal physical mechanisms occurring on extremely small (~$10^{-9}$ meter) length scales and extremely fast (~$10^{-12}$ second) time scales. These results improve fundamental understanding of the distinctive properties of hybrid semiconductor nanomaterials, providing a pathway to improve nanomaterial design and optoelectronic device performance going forward.

## 1.2 Historical Development of Nanomaterials

Mankind has been taking advantage of the unique optical properties of nanoparticles to make colored glasses and dyes for thousands of years, albeit without understanding what they were or how they worked[8,19,28]. The modern history of nanoparticles began in the 1980s, when researchers grew nanocrystals (NCs) of controlled sizes from 1 to 40 nanometers (nm) as inclusions embedded in glass and noted their size-dependent optical properties[29]. It was also around this time that the theory of the quantum confinement effect in nanocrystals—or quantum dots (QDs), as they are often known—was rigorously developed[30]. Early syntheses of colloidal NCs (see **Figure 1.1a**) were soon reported[31], opening the door to a range of new production methods. With the first synthesis of highly monodisperse colloidal NCs *via* the hot injection method[32], more advanced studies of the underlying physics of NCs became possible. Since then, synthesis methods have continued to improve, leading to greater control over nanocrystal sizes and shapes[33], formation of well-ordered nanocrystal superlattices[25,34,35] (**Figure 1.1b**), implementation of more advanced core-shell structures[36,37] (**Figure 1.1c**), and expansion to a variety of new material systems[8,24,38,39]. Today, nanocrystals have an active research community

and are at or near commercialization in a number of applications including displays[40], solar cells[4], and lasers[12] among others.

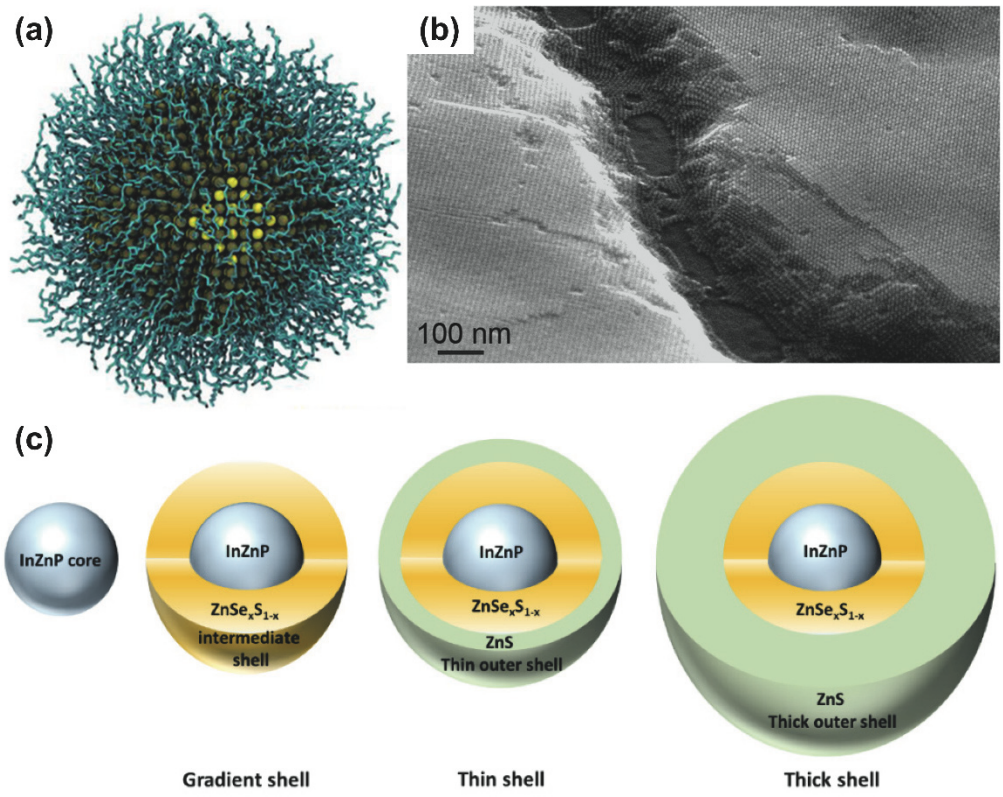


**Figure 1.1. Advances in semiconductor nanocrystal synthetic methods.** (a) Colloidal PbS nanocrystal coated in oleate capping ligands. Reprinted (adapted) with permission from *J. Phys. Chem. C* 2022, 126, 33, 14264–14274. Copyright 2022 American Chemical Society.[41] (b) Monodisperse PbS colloidal nanocrystals self-assembled into a three-dimensional superlattice. Reprinted (adapted) with permission from *Chem. Mater.* 2015, 27, 2, 474–482. Copyright 2014 American Chemical Society.[34] (c) Progression of increasingly passivated core-shell nanocrystals, showing the InZnP core (blue), $ZnSe_xS_{1-x}$ intermediate shell (yellow), and ZnS outer shell (green). Open Access figure reproduced from *Nanomaterials* 2022, *12,* 20, 3703.[42]

Adjacent to the quantum dot community—which is primarily focused on zero-dimensional (0D) nanocrystals that come in relatively isotropic shapes like spheres and cubes—many other research fields exist that are dedicated to nanomaterials found in various other geometries. These include 0D clusters and large molecules, 1D rods and nanotubes, 2D sheets and layered materials, and many other structures[19,43–51], some of which are illustrated in **Figure 1.2**. While different in structure and composition, these highly anisotropic nanomaterials nonetheless share many of the

same unique properties as their zero-dimensional counterparts, including quantum confinement effects and high surface area-to-volume ratios.

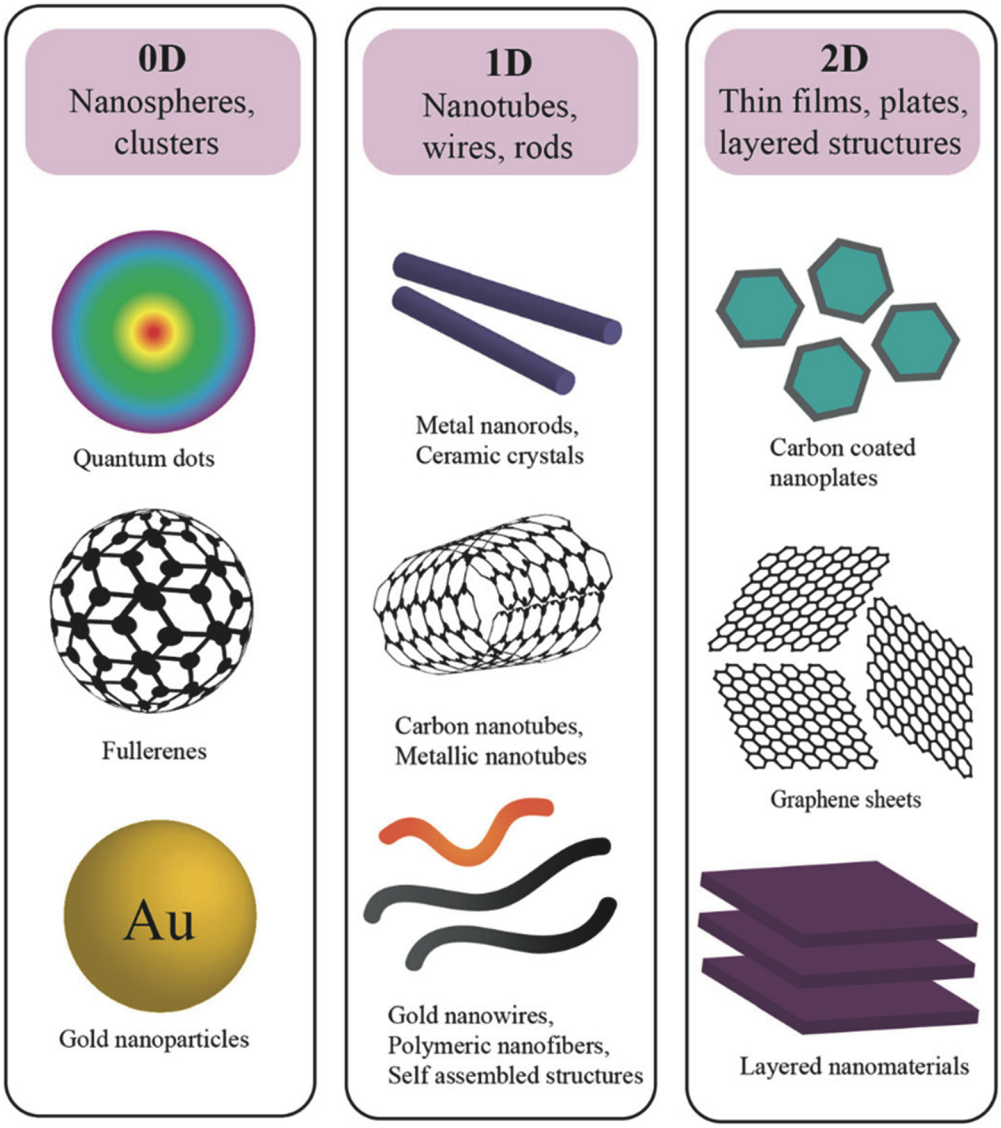


**Figure 1.2. Different low-dimensional geometries and structures of nanomaterials.** 0D (left), 1D (center), and 2D (right) geometries of nanomaterials, showing example material systems for each. Open access figure reproduced from *Particle and Fibre Toxicology* 2018, *15, 1*, 46 under Creative Commons License 4.0 (https://creativecommons.org/licenses/by/4.0/).[52]

Of particular relevance to this thesis is recent work studying 2D materials. The 2D materials research community has grown rapidly over the last two decades since the synthesis of

monolayer graphene *via* mechanical exfoliation in 2004[53]. The many fascinating and useful properties exhibited by monolayer graphene[21,54,55] have driven increased interest in other atomically thin 2D materials. Transition metal dichalcogenides (TMDs)[56], an optically active set of materials[51,57] that can be considered the semiconducting equivalent to graphene and similarly exhibit unique physical properties[51,58], is another 2D material family that has attracted considerable attention recently. Both graphene and TMDs are synthesized *via* top-down exfoliation or bottom up vapor deposition approaches[59,60], neither of which is optimal for large scale and low-cost production of high quality materials for commercial use. The thickness-dependent properties of these van der Waals 2D materials also present a challenge in scaling up to the device level as they require either the use of a single monolayer of material or the fabrication of a stacked heterostructure[61,62]. Addressing this issue, recent advances in 2D materials technology include the development of solution chemistry-based synthetic approaches. This methodology enables self-assembly of layered 2D semiconductors[63,64], bringing the properties of atomically thin 2D van der Waals materials to a more preferable 3D crystalline form.

### 1.3 Lead Halide Perovskites: A Hybrid Material System

Beyond nanoscale geometry, many next-generation semiconductor materials are notable for their complex chemical compositions, being comprised of many different elements and combining different chemical motifs into a single material. This can enable tunable properties *via* the substitution of an element with a related one, e.g. the replacement of chloride with other halide ions (fluoride, bromide)[24]. Different chemical moieties can also combine in interesting ways, such as hybrid materials that consist of repeating organic and inorganic layers which correspondingly alternate between insulating and semiconducting electrical properties[63]. As with nanomaterials, the benefits of these complex materials come with concomitant challenges in understanding their underlying physics. The two main hybrid material systems that comprise the focus of this thesis are lead halide perovskites and metal organic chalcogenolates (MOCs).

Lead halide perovskites are perhaps the most studied emerging material system of the last decade. Having first been identified as a potential photovoltaic material in 2009[65], perovskite solar cells have since been improved to the point of rivaling silicon photovoltaics, with a power conversion efficiency of over 25%[66]. Additionally, perovskites have been proven effective across

a growing array of optoelectronic applications including displays, lasers, photodetectors, and more[6,63]. Lead halide perovskites are a class of crystalline semiconductor materials with an $ABX_3$ stoichiometry that normally assumes a cubic, tetragonal, or orthorhombic structure, as shown in **Figure 1.3a**. The A site can be one of several cations, the most common being methylammonium, formamidinium, and cesium[2,24]. The B-site contains a $Pb^{2+}$ cation, although alternative (and less toxic) elements like tin have been explored[2]. Finally, the X-site halide ion can be iodide, bromide, chloride, or a mixture of the three.[2,67] By varying these compositional building blocks, the optoelectronic properties of the perovskite crystal, such as the absorption and emission spectra, can be tuned over the full visible light range, as shown in **Figure 1.3b**[24,68]. Additionally, parameters such as the crystal structural stability (e.g. *via* the Goldschmidt tolerance factor) can be optimized.[69,70]

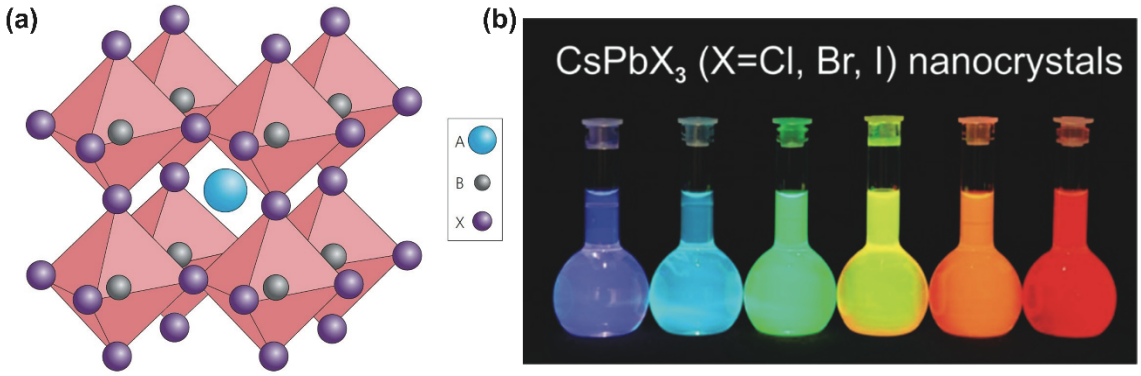


**Figure 1.3. Lead halide perovskite structure and tunability.** (a) Generic $ABX_3$ perovskite cubic structure, showing the B-site cation (gray) and X-site anion (purple) arranged in corner-sharing octahedra (pink), with the A-site cation (blue) located in the center. Reprinted by permission from Springer Nature: *Nature Photonics* "The emergence of perovskite solar cells," Martin A. Green *et al.* Copyright 2014.[2] (b) Emission tunability of $CsPbX_3$ perovskite nanocrystals covering the full visible light spectrum by varying the NC size and composition. Open Access figure reproduced from *Nano Lett.* 2015, *15,* 6, 3692-3696.[24]

Lead halide perovskites are a direct bandgap material with a high absorption coefficient[2,71], which is useful for device applications like photovoltaics. Lead halide perovskites are also noteworthy for their high defect tolerance, allowing perovskite devices to operate efficiently despite a high concentration of lattice vacancies, interstitial ions, and other structural defects.[72–74] This defect tolerance is reflected in the long carrier diffusion length of perovskites, with some reported values in excess of 100 micrometers (μm),[75,76] allowing charge carriers to travel

significant distances through the lattice without scattering or recombining. These properties contrast with many other semiconductor crystals like silicon, where such defects create energetic states within the bandgap that trap excited carriers and lead to non-radiative recombination.[77] The mechanism leading to defect tolerance in perovskites is still under investigation. It is possible that defects don't lead to the formation of midgap trap states[68,72,73], or strong electron-lattice interactions screening excited carriers (e.g. polaron formation) may be the driving factor[74,78,79]. Despite high defect tolerance, the major fault of lead halide perovskites is their instability when exposed to air, moisture, or heat[3,67].

Perovskite nanomaterials show great promise in combining the unique attributes of bulk perovskites with the emergent properties of low-dimensional systems, including 0D perovskite nanocrystals[6,24], 1D nanorods[48], 2D nanoplatelets[33], and layered 2D perovskites[63,80]. For example, perovskite nanocrystals have shown broad compositional tunability and quantum yields up to 90% in core-only structures not covered in a passivating shell layer[24]. They also show the potential for improved stability compared to their bulk counterparts[3,6,67,81,82], owing to their insulating organic sublayer. A study on the temperature-dependent exciton dynamics in $CsPbBr_3$ perovskite nanocrystals will be discussed in Chapter 4 of this thesis.

### 1.4 Metal Organic Chalcogenolates (MOCs)

A second hybrid material system which has played an important role in my thesis studies is metal organic chalcogenolates (MOCs), also variously known as MOChas, metal organic chalcogenides, or organic metal chalcogenides (OMCs). Contrasting with the many thousands of studies performed on lead halide perovskites, there have been only a few dozen reports on the properties of optically-active MOCs as of this writing. The prototypical MOC example is silver phenyl selenolate (AgSePh), a 2D layered material notable for its alternating inorganic and organic sub-layers, as illustrated in **Figure 1.4a** and **Figure 1.4b**. Each inorganic sub-layer is comprised of a covalently bonded AgSe network, with each of the Se atoms also covalently bonded to a phenyl ring either above or below the AgSe layer, forming the organic component. Adjacent 2D sheets are connected only by weak van der Waals interactions. AgSePh was first reported in a 2002 synthesis paper by the Corrigan group[83], but its optical properties were not recognized or studied

until its rediscovery in 2018 by the Hohman group[84]. AgSePh has a direct bandgap[85,86] and exhibits narrow bandwidth blue emission at 467 nm[84] (see **Figure 1.4c** and **Figure 1.4d**) with sub-nanosecond exciton lifetimes[87,88]. Combining these optical properties with its straightforward synthesis, air stability, and heavy-metal free composition, AgSePh shows great potential for use in a variety of optoelectronic applications.

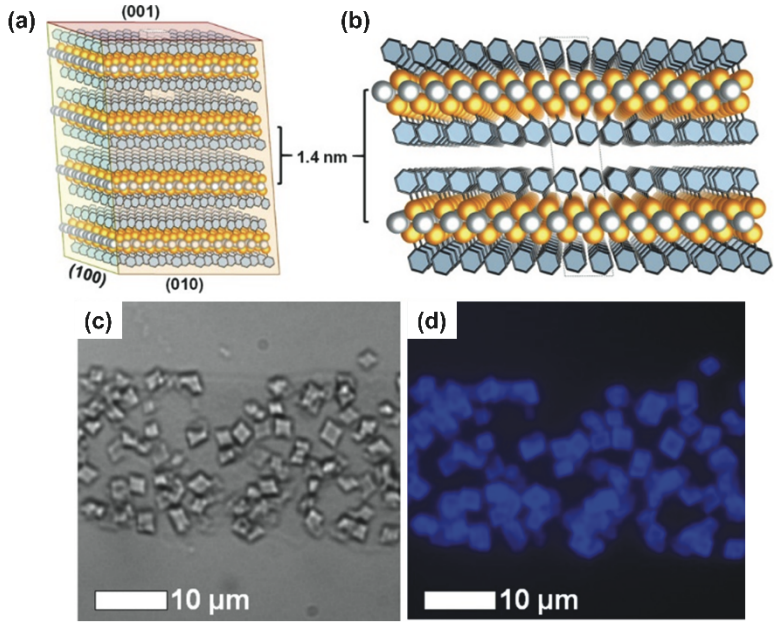


**Figure 1.4. Structure and emissive properties of AgSePh.** (a) Layered 2D structure of AgSePh with 1.4 nm sheet-to-sheet spacing noted. (b) View of two AgSePh sheets, showing the Ag (white), Se (yellow), and phenyl (blue) components. (c) AgSePh microcrystals formed *via* the biphasic reaction. (d) Bright blue photoluminescence emission from the same array of AgSePh microcrystals shown in panel (c). Reprinted (adapted) with permission from *ACS Appl. Nano Mater.* 2018, 1, 7, 3498-3508. Copyright 2018 American Chemical Society.[84]

Most early studies of AgSePh and MOCs in general have focused on driving synthetic improvements[88–94] in crystalline size and quality. Similar to perovskites, MOCs are also a tunable material platform, with structural and optoelectronic properties that can be modified by compositional changes to the chalcogen[86,95,96], metal[97], or organic[88,97] components. MOCs exhibiting a 2D structure similar to AgSePh have been most frequently studied, but 1D and 0D[43,98] structures can also be formed. Despite the recent interest for the past several years, MOCs are a mostly unexplored material family. Early results suggest many parallels to 2D perovskites or

TMDs. Similar to 2D perovskites, the band edge electron density in 2D MOCs is contained mostly within the inorganic sub-layer, with the organic sub-layer acting as a spacing layer that electronically isolates adjacent sheets. However, the covalent bonding in the system is more like TMDs and suggests that organic layer functionalization could impact the electronic structure to some degree. This covalent bonding also likely contributes to the robustness of MOCs, which are stable in air over days or longer, an improvement over the stability issues that present a continued challenge for 2D perovskites[99]. Later in this thesis, I also share a study of exciton-phonon coupling in 2D layered AgSePh, paralleling previous reports of exciton-phonon coupling in both TMDs[100] and 2D perovskites[101,102]. Additionally, the 2D layered structure of AgSePh has been shown to give rise to other interesting physical phenomena, like anisotropic in-plane excitons[86]. These few photophysical studies are likely just the tip of the iceberg on the unique physical phenomena exhibited by hybrid MOC nanomaterials, leaving the underlying physics of this material family still to be discovered.

### 1.5 Quantum Confinement Effect in Nanomaterials

The most noteworthy emergent property of nanomaterials is the quantum confinement effect. Since nanocrystal research began in earnest, quantum confinement was the first property that captured the interest of researchers[29–31], as it allows for NC size-dependent bandgap tunability and narrowed emission bandwidth (see **Figure 1.5**). We can better understand this phenomenon by calculating the quantum confinement effect in an example cuboidal semiconductor nanocrystal. In bulk intrinsic semiconductors, there are a set of closely packed filled low energy levels called the valence band (VB) and a separate set of closely packed empty high energy levels called the conduction band (CB). In between these is a region where no energy levels are found due to electron orbital interactions, referred to as the bandgap. In classical solid state physics models of bulk semiconductors, the bandgap is independent of the size of the semiconductor crystal and the VB and CB energy levels can be considered continuous. However, as the crystal size is reduced to the nanoscale, the energy levels in both bands begin to shift and the bandgap grows larger. This effect is due to the confinement of the quantum mechanical wavefunctions that describe electron/hole movement in a crystal. **Figure 1.5** illustrates the quantum confinement effect in a

semiconductor nanocrystal. Using a quantum mechanical particle in a box model, we can calculate to first-order the degree to which quantum confinement affects the bandgap in a NC.

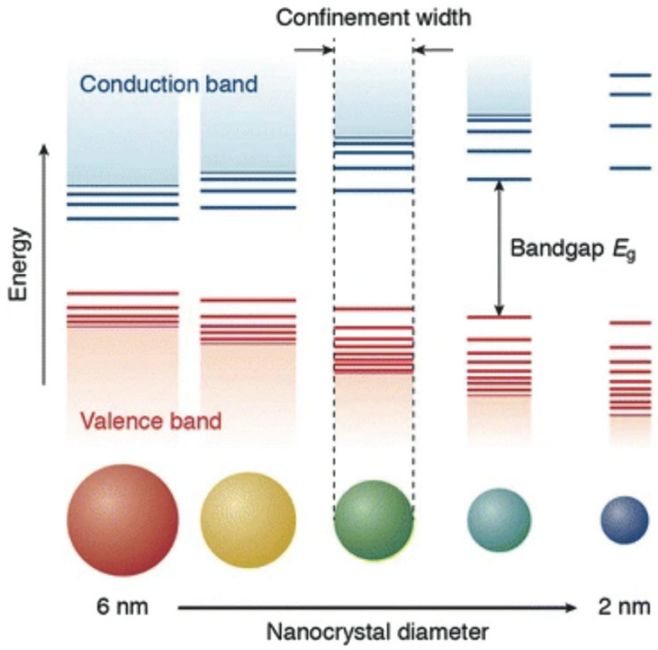


**Figure 1.5. Quantum confinement effect in semiconductor nanocrystals.** For nanocrystals of decreasing diameter (increasing quantum confinement), the valence and conduction bands separate and become more quantized near the band edge. Open Access figure reproduced from *Top. Curr. Chem. (Z)* 2016, *374, 5,* 58 (http://creativecommons.org/licenses/by/4.0/).[103]

We can imagine a NC absorbing a photon of light, exciting a single negatively-charged electron from the full valence band to the empty conduction band and leaving behind a positively-charged hole. In a bulk crystal, these two carriers would be separated in energy by the bulk material bandgap and free to move in all directions (ignoring other effects like Coulombic and carrier-lattice interactions). However, the infinite particle in a box model assumes that there is an infinite potential energy outside of the nanocrystal, so the electron and hole are confined to the nanocrystal and the wavefunctions of both are zero at the crystal boundaries. Here, we will solve the system in 1 dimension and then expand that solution to 3 dimensions.

We begin the analysis with the time-independent Schrödinger Equation for a steady-state wavefunction solution, $\psi$, for a carrier with energy $E$, position $\vec{r}$, and mass $m$:

$$\hat{H}\psi = E\psi\,, \tag{1.1}$$

where the Hamiltonian is defined by

$$\hat{H} = -\frac{\hbar^2}{2m}\nabla^2 + V(\vec{r})\,. \tag{1.2}$$

By applying the potential energy V as described above, we see that the wavefunction must be zero everywhere outside of the NC for a system of finite energy. Within the NC, the electron and hole are treated as free particles with boundary conditions of

$$\psi(0) = \psi(d) = 0 \tag{1.3}$$

at the surface of the NC of diameter $d$. We assume a free particle solution of the form

$$\psi = C_1 e^{-ikx} + C_2 e^{ikx}\,, \tag{1.4}$$

with constants $C_i$. Equation 1.4 can be rewritten as

$$\psi = C_3 \sin(kx) + C_4 \cos(kx)\,. \tag{1.5}$$

By applying the boundary conditions at x=0, the cosine term must be zero. Applying the second boundary condition at x=d, we see that

$$\begin{aligned} \psi(d) &= 0 = C_3 \sin(kd) \\ k &= \frac{n\pi}{d} \end{aligned}\,. \tag{1.6}$$

Thus, the wavefunction of a 1D particle in a box is

$$\psi(x) = C \sin\left(\frac{n\pi x}{d}\right). \tag{1.7}$$

The associated energy of the particle is found by solving Equation 1.1 with the solution found in Equation 1.7, which yields

$$E_n = \frac{\hbar^2 k_n^2}{2m} = \frac{\hbar^2 n^2 \pi^2}{2md^2}\,. \tag{1.8}$$

Expanding this solution to 3 dimensions and solving for the lowest available energy level (n=1 in all three dimensions) gives

$$\psi(x,y,z) = C\sin\left(\frac{\pi x}{d}\right)\sin\left(\frac{\pi y}{d}\right)\sin\left(\frac{\pi z}{d}\right) \tag{1.9}$$

and

$$E = \frac{\hbar^2\pi^2}{2md^2}. \tag{1.10}$$

This is the lowest available energy level for an electron in the conduction band above the bulk band edge, and it is also the highest energy level for a hole in the valence band below the bulk band edge. These values are consistent with the bulk limit, where the energy approaches the band edge for increasingly large crystals ($d \to \infty$). Combining Equation 1.10 for both the electron and the hole with the bulk bandgap, we find that the NC bandgap can be calculated as

$$E_{gap} = E_{gap,bulk} + \frac{\hbar^2\pi^2}{2m_e d^2} + \frac{\hbar^2\pi^2}{2m_h d^2}, \tag{1.11}$$

with the effective mass of the electron and hole given as $m_e$ and $m_h$, respectively. For a hydrogen atom with only one electron, the effective mass is simply the mass of an electron, approximately $m_o = 9.11\times10^{-31} kg$. However, the presence of many lattice sites and other electrons in the lattice impacts the effective mass of the electron and hole under consideration. The effective mass can be approximated from the band structure of the material by

$$\frac{1}{m_{eff}} = \frac{1}{\hbar^2}\frac{\partial^2 E}{\partial k^2}, \tag{1.12}$$

where the curvature of E with respect to k is evaluated at the band edge for the electron and hole.

This solution is only a first-order approximation and is limited for several reasons. First, it does not take into account the exciton binding energy of the system. An exciton is a neutral quasiparticle formed from a negatively-charged electron and a positively-charged hole. Its existence is the result of Coulombic interactions between the electron and the hole that make them more energetically stable as a pair rather than as independent particles. This lowers the effective bandgap by the exciton binding energy—the difference between the lowest energy exciton state

(which resembles a hydrogen atom in its available energy levels) and the energy of the free electron and hole. Next, this approximation assumes an infinite quantum well, where the wavefunction must be identically zero at the edge of the nanocrystal. In reality, there is a large but finite potential energy beyond the NC core, the value of which depends on the NC shell (if there is one), the ligands, and the NC surroundings. This allows for some amount of electron or hole wavefunction spread outside of the NC core, reducing the quantum confinement of the system. In addition, the NC shape, the dielectric environment, and other factors also impact the degree of quantum confinement experienced by the excited carriers. The general principles of quantum confinement described here for 0D nanocrystals can also be extended to 2D[63,104] and 1D[48] systems, with confinement only occurring in one and two dimensions, respectively.

### 1.6 Other Emergent Properties in Hybrid Semiconductor Nanomaterials

Beyond quantum confinement, hybrid organic-inorganic semiconductor nanomaterials exhibit many properties that are unique from purely organic or inorganic bulk materials systems. Some of these properties result solely from their nanoscale structure or from their complex hybrid composition, while others emerge from both attributes in combination. A relatively simple and intuitive example is the colloidal nature of nanocrystals. Unlike bulk inorganic semiconductors, colloidal NCs are solution processable, meaning they can be suspended in various solvents while maintaining their core structure and properties[6,8]. In this way, they can be deposited on a thin film or substrate through common techniques such as spin coating or spraying, allowing for the fabrication of inexpensive and flexible optoelectronic devices[105,106]. Monodisperse colloidal NCs have also been shown to form regular, closely packed superlattices (see **Figure 1.1b**), which is important for charge or energy transport in many device applications.

In another case, the dielectric environment of hybrid organic-inorganic nanomaterials can play a large part in key physical phenomena through Coulombic interactions. In most hybrid semiconductor nanomaterials, including perovskites and MOCs, the electron density of the VB and CB is primarily confined to the inorganic sub-component[86,107]. However, the dielectric environment surrounding the carriers still impacts their Coulombic interactions and is spatially inhomogeneous in hybrid organic-inorganic nanomaterials. In general, the dielectric constant is lower for the organic component than the inorganic component[108], thus the carriers are subject to

reduced dielectric screening in hybrid structures than in a fully inorganic bulk crystal made of the same material. The reduced screening means the carriers are subject to stronger Coulombic attractions or repulsions, leading to an increased exciton binding energy. This phenomenon makes it possible to tune the exciton binding energy (and effectively the bandgap) in a hybrid nanomaterial simply by changing the dielectric environment[109]. This effect can also lead to counter-intuitive results like faster exciton transport from a NC to a monolayer TMD than to a multi-layer TMD sample due to reduced dielectric screening[110] (**see Figure 1.6**), providing another channel for material tunability[111].

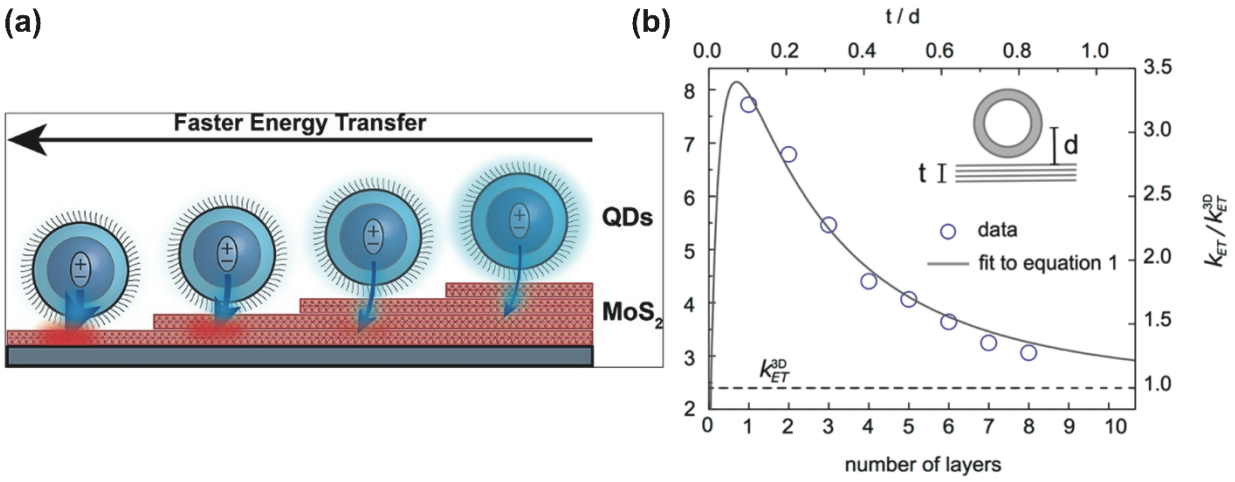


**Figure 1.6. Dielectric effects on energy transport in nanomaterials.** (a) Schematic showing exciton transport from a CdSe nanocrystal or quantum dot (QD) to single- and few-layer $MoS_2$, a transition metal dichalcogenide (TMD). (b) Quantification of energy transfer rates from the QD to TMD, showing faster rates of transfer with fewer TMD layers due to reduced dielectric screening. Reprinted (adapted) with permission from *Nano Lett.* 2014, 14, 11, 6087-6091. Copyright 2014 American Chemical Society.[110]

Charge and energy transport in organic-inorganic nanomaterials is also greatly impacted by both the nanometer scale structures and hybrid character of these materials. In a traditional bulk inorganic semiconductor, charge carriers exhibit band-like transport through a relatively flat energetic landscape[112], except near interfaces or grain boundaries normally present on ~µm length scales[20]. In contrast, hybrid nanomaterials are designed with nanometer scale periodicity to their structures, presenting recurring energy barriers to transport caused by the wider bandgap organic component. This creates a disconnect in the band-like electronic structure of the material and forces charge carrier transport instead to occur through a hopping mechanism[113,114].

The excitonic nature of nanomaterials introduced previously also greatly influences charge transport. Energy or exciton transport in these materials is possible through a tunneling mechanism (Dexter) that shows exponentially decaying dependence on separation distance ($k_{Dexter} \propto \exp(-r)$)[115]. However, energy transfer is also possible *via* dipole-dipole interactions (Förster resonance energy transfer or FRET) exhibiting $k_{FRET} \propto r^{-6}$ dependence[115,116], a mechanism absent from free carrier transport and dominant at slightly longer separation distances of a few nanometers. The dielectric environment has a large effect on FRET, as discussed previously and shown in **Figure 1.6**[110]. If however, charge or free carrier transport rather than energy transport is the goal—e.g. to generate a net current—then exciton dissociation is first required, a process that depends highly on the exciton binding energy. Thus, multiple emergent characteristics are important to control the interplay between exciton and free carrier transport in hybrid nanomaterials[115,117].

Electron-phonon interactions in hybrid semiconductor nanomaterials must also be considered. Due to the less rigid structure of these materials compared to bulk inorganic semiconductors, they exhibit much stronger electronic and vibrational coupling. This effect has been shown for multiple material systems and dimensionalities including nanocrystals[118], 2D materials[119], and bulk hybrid organic-inorganic materials[120]. Electron-phonon coupling can have a large impact on a variety of optoelectronic properties including improved charge transport due to polaron effects[79,120], broadband light emission through self-trapped exciton formation[96,121], and others. A much more thorough discussion on the physical mechanisms of electron-phonon coupling and how it impacts macroscopic attributes is provided for the case of 2D AgSePh in Chapter 3 of this thesis.

This summary just scratches the surface of the many emergent properties of hybrid organic-inorganic semiconductor nanomaterials. These individual properties also influence each other in interesting ways, such as the case of excitonic, energetic, and dielectric effects all impacting the rates of charge and energy transport in nanomaterials. Controlling macroscopic optoelectronic properties in these materials requires a complete understanding of these complex properties and their interactions.

## 1.7 Thesis Overview

In this thesis, I investigate the unique physical processes present in hybrid organic-inorganic semiconductor nanomaterials. In this chapter, I provided a history of the development of nanomaterials, specifically 0D nanocrystals and 2D materials, as well as a description of two material systems of interest, lead halide perovskites and metal organic chalcogenolates. I then summarized some of the most interesting emergent properties exhibited by hybrid semiconductor nanomaterials which will also be explored further within this thesis.

In Chapter 2, I provide an overview of my primary technique for studying these materials, transient absorption (TA) spectroscopy. This ultrafast technique is used to probe the electronic structure of nanomaterials with femtosecond time resolution over a broad energy range. I detail the theoretical and practical aspects of generating the necessary ultrafast laser pulses and employing them to investigate semiconductor nanomaterials.

Chapter 3 details my results investigating exciton-phonon coupling in 2D AgSePh. Many different spectroscopic techniques are used to study the material, including impulsive vibrational spectroscopy (a time-domain Raman method similar to TA), non-resonant Raman spectroscopy, and temperature-dependent photoluminescence spectroscopy. These experimental techniques are paired with density functional perturbation theory computational results to identify the dominant vibrational modes in this system and what is unique about these particular modes.

In Chapter 4, I present work studying temperature-dependent charging and neutralization processes in $CsPbBr_3$ perovskite nanocrystals. This project identifies a long-lived, redshifted signal present in the TA spectrum at low temperatures, which we ascribe to a charged NC species. Temperature-dependent TA data then provides insights into the mechanism of NC neutralization in this system. These results help improve understanding of the heterogeneous energy landscape present in perovskite NCs compared to bulk perovskites.

Finally, Chapter 5 includes my closing remarks and reflections on future directions for my research. In this thesis, I study hybrid semiconductor nanomaterials that combine low dimensional geometries with complex chemistries, e.g. 0D perovskite nanocrystals and 2D layered metal organic chalcogenolates. Using advanced spectroscopic techniques, I am able to discover the underlying physics that make these materials unique. These nanoscale physical insights can then

be connected to macroscale properties, providing a pathway to engineer new hybrid semiconductor nanomaterials and ultimately optimize the performance of next-generation optoelectronic devices.

# Chapter 2
# Transient Absorption Spectroscopy: Theoretical and Practical Details

*Suffice it to say that, in an earlier day, the study of these short-lived high-energy molecules and their chemical characteristics could hardly even have been contemplated as a wild dream.*

Professor H.A. Ölander, member of the Nobel Committee for Chemistry, on bestowing the 1967 Nobel Prize for Chemistry to Ronald Norrish and George Porter for their work on flash photolysis, the precursor to modern pump-probe spectroscopy[122]

## 2.1 Introduction

In Chapters 3 and 4, we will discuss the electronic and vibrational properties of several semiconductor nanomaterial systems, which evolve on extremely fast timescales down to the femtosecond regime. In order for these physical processes to be studied experimentally, a technique must be employed that can resolve such rapid changes in a material. This is not a trivial challenge, and very advanced spectroscopic equipment and methods have been developed in recent decades in order to make this possible[123,124]. These spectroscopic techniques involve exposing a material of interest (e.g. an atomic, molecular, or solid system) to one or more ultrafast laser pulses, coherent light pulses with a duration of less than a picosecond. These laser pulses impulsively excite the optically active material out of its equilibrium ground state and into a dynamically changing excited state.

This chapter has several goals. It is first meant to explain the basic principles of ultrafast transient absorption spectroscopy as well as its applications and limitations. It also provides a theoretical discussion on the generation and conditioning of the ultrafast laser pulses involved. Finally, it is meant to be a practical guide to the Tisdale lab transient absorption setup for use by current and future members of the research group.

## 2.2 Overview of Ultrafast Spectroscopy

The key benefit to ultrafast spectroscopy experiments is that they are designed such that the time resolution, or the fastest physical process that can be resolved using the technique, is not limited by any electronic component in the system. Instead, the time resolution is determined only by the duration of the laser pulse(s) used in the experiment, enabling orders of magnitude improvement in resolution over the fastest electronic-based timing systems[125]. This laser-based timing mechanism also motivates the use of methods like pulse compression (discussed later in the chapter) that minimize the duration of the laser pulse in order to measure ultrafast processes with the most clarity.

Advancements in ultrafast lasers have made these techniques much more widely available. Several decades ago when ultrafast lasers were first developed, performing ultrafast spectroscopy experiments required specialized, custom-built experimental setups[123,126]. Today, there are commercially available ultrafast laser systems that operate at kHz repetition rates and generate sub-100 fs duration laser pulses, enabling ultrafast techniques to be employed by a growing number of research groups[124]. Coupled with modern pulse compression setups using advanced optical materials, experiments with ~10 fs time resolution are now routinely performed[127–129], and specialty setups at the leading edge of the technology are pushing ultrafast spectroscopy into the attosecond regime[130,131]. These advancements have greatly expanded the physical processes that can be studied. For example, hot carrier cooling and nanoscale charge transport processes that occur on femtosecond to picosecond timescales have been investigated using ultrafast techniques[57,74]. So too have molecular vibrations, which exhibit oscillatory periods of roughly 10-100 femtoseconds[124,132]. At the lower limit of pulse duration, ultrafast techniques have been used to track bound core electron dynamics occurring on attosecond timescales[133].

Many different ultrafast techniques have been developed that employ various laser pulse trains, experimental geometries, and detection schemes, including transient absorption spectroscopy (TA)[123,127,134], time-resolved second harmonic generation (SHG)[57,135,136], femtosecond stimulated Raman spectroscopy (FSRS)[137,138], coherent anti-Stokes Raman spectroscopy (CARS)[139], impulsive vibrational spectroscopy (IVS)[128,140], and many others. Among these techniques, the most common and straightforward is likely pump-probe transient absorption (TA) spectroscopy. This workhorse technique involves two laser pulses interacting with the

sample. The first is a monochromatic pump pulse that excites the sample electronically and/or vibrationally. The second is normally a broadband probe pulse that arrives at a specified time delay after the first and interrogates the system. The probe pulse that transmits through the sample is routed to a spectrometer and is used to measure the absorption spectrum of the material. The absorption spectrum of the excited state after pumping is subtracted from the absorption spectrum of the ground state in the absence of the pump pulse, giving a differential measurement that represents the change in optical transmission due to the pump excitation. The TA signal intensity is normally represented as an optical density measurement (ΔOD), defined by:

$$I_{TA}(\Delta OD) = -\log_{10}\left(\frac{T_{on}}{T_{off}}\right), \tag{2.1}$$

where $T_{on}$ and $T_{off}$ are the wavelength-dependent probe transmission intensities when the pump pulse is on and off, respectively. For TA spectroscopy, the time resolution of the experimental setup is defined by the cross-correlation or convolution of the pump and probe laser pulses[141,142]. **Figure 2.1** shows a simplified schematic of the TA experimental geometry and sample data showing how the TA signal is derived from the ground and excited state absorption curves.

From TA data, fundamental physical properties such as vibrational dynamics or the energetic distribution of carriers within the band structure of a material can be determined. Contributions to the transient absorption signal include ground state bleach, stimulated emission, and excited state absorption[123]. Ground state bleach is caused by a reduction in available transitions from the valence band to the conduction band as a result of excitation by the pump pulse; stimulated emission involves a probe photon inducing the coherent emission of a photon with the same energy from the excited state of the material. Both of these processes appear as a negative TA signal ($T_{on} > T_{off}$). Conversely, excited state absorption results from new excitation pathways available in the excited state that weren't present in the ground state and appears as a positive TA signal ($T_{on} < T_{off}$). The combined effect of all three of these processes generates the wavelength-dependent TA signal, which also varies as a function of time delay between the pump and probe pulses.

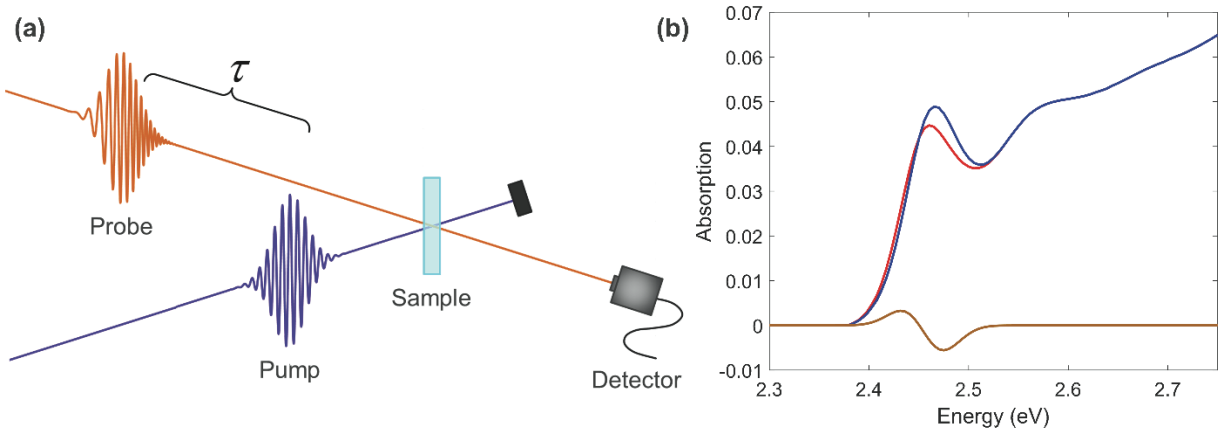


**Figure 2.1. Schematic of transient absorption spectroscopy technique.** (a) Non-collinear TA setup showing the pump pulse (purple) and broadband probe pulse (orange) sequentially interacting with the sample with a time delay τ. (b) The TA signal (gold) is calculated from the difference between the ground state absorption spectrum (blue) and the excited state absorption spectrum (red) of a sample.

## 2.3 Broadband Probe Light

Both the pump and probe laser pulses in our setup originate from the same ultrafast light source, a Spirit 1040-8W Yb regenerative amplifier ultrafast laser from Spectra-Physics that generates 1040 nm laser pulses of ~300 fs pulse duration with a power output of 8 W at a 200 kHz repetition rate. This initial laser output is split into two different beam paths. One portion is sent to a non-collinear optical parametric amplifier (NOPA) to generate a tunable pump laser pulse, as will be discussed further in the next section. The other portion is used to generate the broadband probe light, through a process termed supercontinuum (SC) light generation.

SC generation is a non-linear optical process that occurs when high intensity ultrafast laser pulses travel through a number of transparent media. The physics of this process is complex and much more through reviews of the mechanism and SC active media can be found in the literature[143–146]. Briefly, this process occurs through several steps, as illustrated in **Figure 2.2**. First, it is initiated by a self-focusing mechanism. When an ultrafast laser pulse of sufficient peak energy propagates through a transparent dielectric medium, the nonlinear refractive index of the medium begins to take effect. This is the result of the optical Kerr effect (OKE)[147], by which the real component of the refractive index, $n$, has an electric field –dependent term defined by

$$n = n_0 + n_2 I \,, \tag{2.2}$$

where $n_0$, $n_2$, and $I$ are the linear refractive index, the third-order non-linear refractive index term, and the intensity of the light field, respectively. Assuming an approximately Gaussian-shaped laser pulse, the center of the pulse has a higher intensity and therefore experiences a higher refractive index than the edges. This effectively creates a lens within the material that travels with the laser pulse as it propagates, constantly focusing the pulse down to a smaller diameter. As the pulse focuses, the field strength increases and the effect becomes further amplified, creating a positive feedback loop that is only arrested by multiphoton absorption and ionization effects that reduce the pulse strength and defocus the beam[145]. The progression of the beam diameter over time depends on the interplay between these two effects, along with the initial focusing conditions of the beam, the pulse intensity, and the properties of the nonlinear medium.

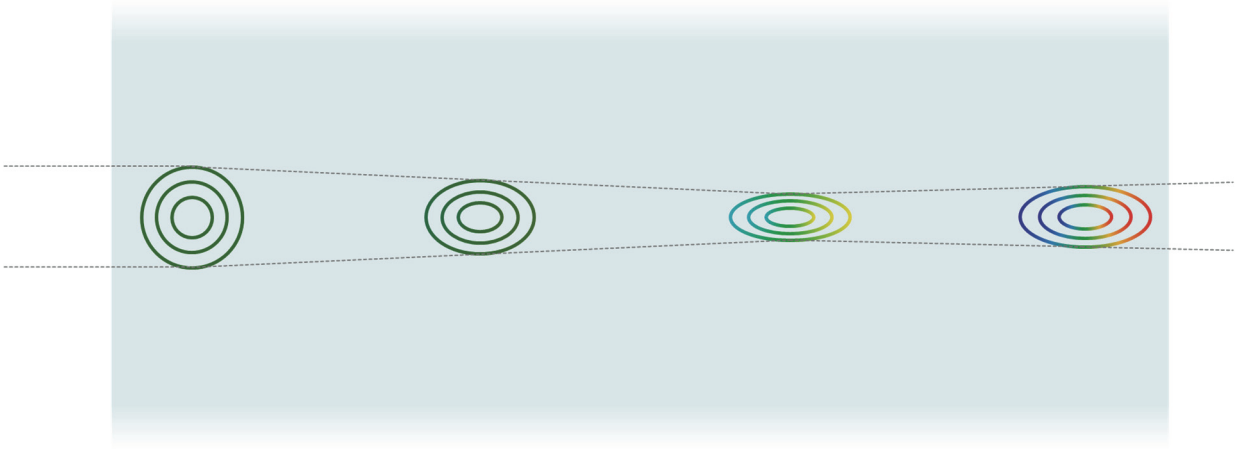

**Figure 2.2. Physics of supercontinuum light generation through a transparent medium.** A monochromatic green ultrafast laser pulse undergoes self-focusing followed by self-phase modulation, generating a chirped broadband laser pulse.

In addition to self-focusing, the refractive index gradient also induces self-phase modulation in the pulse, which causes the spectral broadening that ultimately converts a monochromatic laser pulse into a broadband SC pulse. This is driven by the changing refractive index along the axis of propagation. The leading edge of the laser pulse experiences a positive refractive index gradient, such that the wavelength of the light wave is stretched and the front half of the pulse becomes red-shifted to lower energy. Similarly, the trailing edge experiences a negative gradient and the wavelength is blue-shifted. The resultant laser pulse shows a continuous

spectral shift from red to blue, as illustrated in **Figure 2.2**. As long as a strong refractive index gradient is present, this process will continue to broaden the laser pulse, spanning multiple octaves under optimized conditions[144]. In a normal group velocity dispersion (GVD) material, red light travels faster than blue light, leading to the pulse being stretch out and the field strength eventually dropping below the critical level to sustain this process. In anomalous GVD materials, the trailing blue edge travels faster than the leading red edge, recompressing the pulse and generating "light bullets" that can continue to experience further self-phase modulation[145]. Through self-focusing and self-phase modulation, high intensity ultrafast laser pulses can be spectrally broadened to generate a SC white light laser pulse for use as the probe beam in transient absorption spectroscopy.

In our experimental setup, we have two different lineups for generating SC probe light as shown in **Figure 2.3**, with the selected beam path chosen based on the experimental needs. The primary setup involves routing the 1040 nm Spirit fundamental light into a yttrium aluminum garnet (YAG) crystal. This can be done with a 50 mm focal length lens into a 4 mm crystal to generate ~480-700 nm light, or with a 75 mm focal length lens into a 6 mm crystal to generate near infrared probe light. In order to study metal organic chalcogenolates exhibiting a larger bandgap than could be probed with the YAG setup, we also developed a second beamline using a 3 mm sapphire crystal. This line involves first frequency-doubling the 1040 nm light to 520 nm in a β barium borate (BBO) crystal, then using the 520 nm light as the pumping laser into the sapphire window as depicted in **Figure 2.4**. Finally, the resultant "bluer" SC probe light is filtered and routed onto the same beam path as the YAG setup using a magnet-mounted mirror, enabling either of the SC light setups to be used in any TA experiment. In either case, the resultant probe beam is then routed directly to the sample point without any further optical modulation.

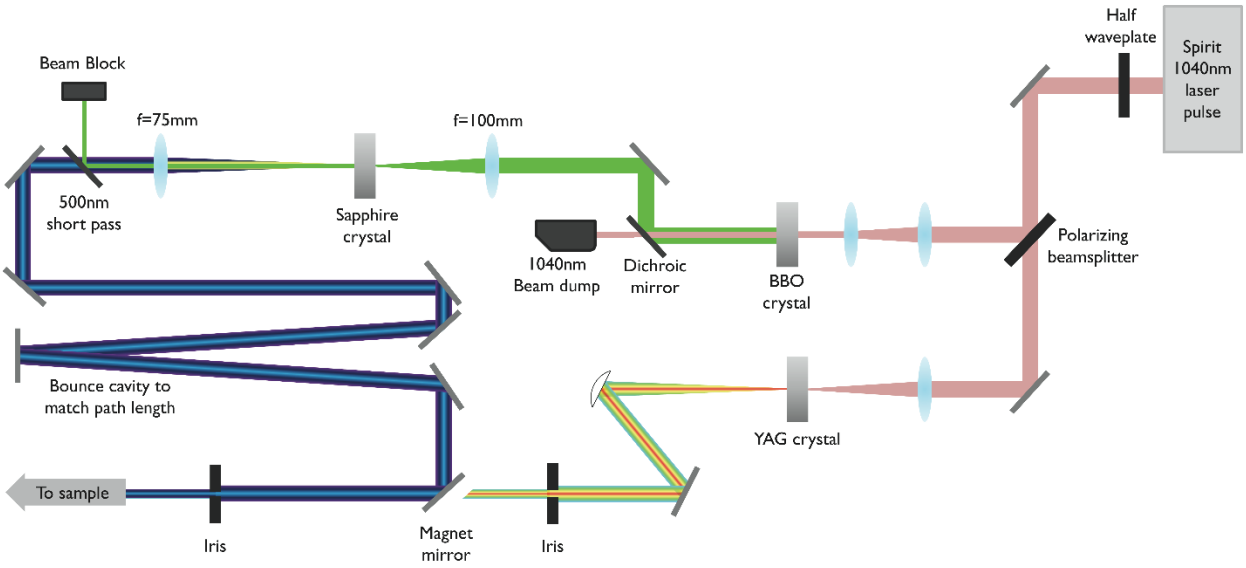


**Figure 2.3. Supercontinuum light generation beam paths in the Tisdale laser lab.** The 1040 nm Spirit output (pink) is either routed directly to a YAG crystal to generate broadband white light (bottom path), or it is first frequency-doubled to 520 nm (green) before being routed to a sapphire window to generate higher energy "bluer" broadband white light (top path).

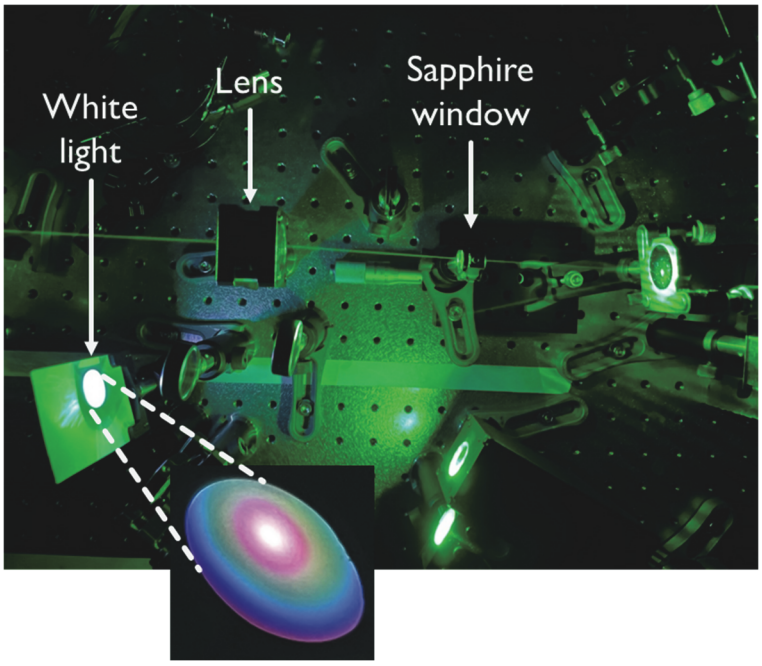


**Figure 2.4. Supercontinuum light generation in a sapphire window.** The 520 nm beam is focused onto the sapphire window using a lens. Supercontinuum white light is recollimated on a curved mirror and filtered to remove residual 520 nm light. Photographs taken in the Tisdale group laser lab.

## 2.4 Tunable Pump Pulse Generation

As noted previously, our transient absorption setup employs a tunable pump beam to provide us with the experimental freedom to excite a semiconductor sample at, above, or below the bandgap. This pump beam is generated in a commercially available non-collinear optical parametric amplifier (NOPA) from Spectra-Physics. The fundamental physical process of a NOPA converts one high energy laser pulse into two lower energy pulses in a transparent nonlinear crystal such as BBO. This process is subject to conservation of both energy and momentum of the photons involved[141]. Below we describe general details of NOPA operation specific to our experimental setup; we recommend further reading from the literature for much more in-depth discussion on the theoretical[148] and practical[149] aspects of optical parametric amplification.

The Spectra-Physics NOPA system we employ first generates seed and pump beams (not the same pump as in our TA setup; that comes later), then undergoes two rounds of amplification, followed by a pulse compression stage, and then finally a second harmonic generation (SHG) stage. The seed beam is formed from SC generation using 1040 nm Spirit fundamental light into a sapphire window. The pump beam is formed by frequency-doubling an additional portion of the 1040 nm light into 520 nm. In the two amplification stages that make up the core of the NOPA, the pump and seed lines are crossed in consecutive BBO crystals at a specific angle to consume the 520 nm pump pulse and amplify a specific wavelength of the broadband seed pulse (between 650 nm and 900 nm), forming the signal beam. The compression stage then involves two transparent prisms that minimize the pulse duration through a process to be discussed further in the next section. Finally, the compressed signal beam is sent to another BBO crystal to perform second harmonic generation, creating the NOPA output pulse at 325 nm to 450 nm, the pump beam as used in transient absorption experiments. Alternatively, the SHG stage can be bypassed, producing a 650 nm to 900 nm output instead.

All of the aforementioned NOPA sub-sections can be optimized by adjusting computer-controlled motors, e.g. the crystal angles to select the wavelength for amplification or delay stages to control pump-seed temporal overlap. Thus, day-to-day use of the system is well-automated, even when switching between output wavelengths. However, a brief reoptimization of the motor positions every few months, as well as a more involved complete mirror realignment and motor adjustment every one to two years is needed to keep the system functioning properly.

## 2.5 Pump Pulse Compression *via* Frequency-Resolved Optical Gating

We have now introduced the fundamental processes that are used to convert a train of ultrafast 1040 nm laser pulses from the Spirit laser into the tunable pump and broadband probe lines. Next, several additional optical and mechanical components are used to modulate the pump beam and enable the transient absorption experiment to be performed. These will each be described in turn, with the complete TA setup illustrated in **Figure 2.5**.

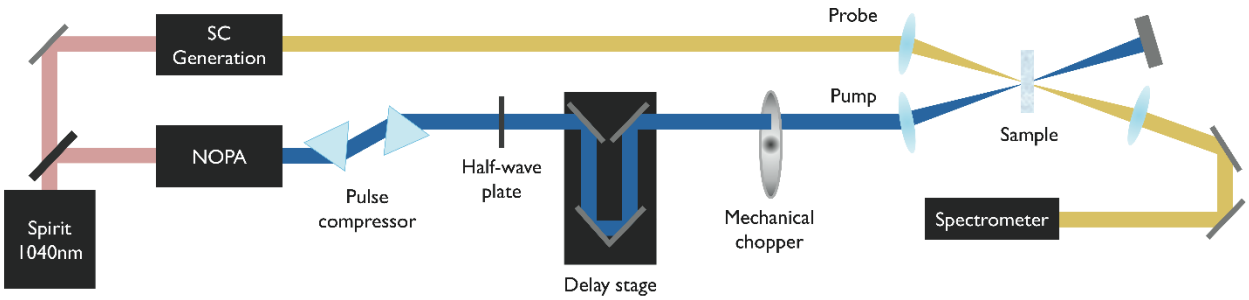


**Figure 2.5. Full transient absorption spectroscopy laser table setup.** This illustration highlights the optical and mechanical components used to modulate the pump and probe beams after they are generated.

The first optics that the pump beam encounters after exiting the NOPA are a pair of fused silica prisms used for pulse compression. This process is used to minimize the duration of the pump pulse, which is critical to improving the time resolution of the TA setup. The pump pulse exits the NOPA with a positive chirp, where the lower energy red portion of the pulse arrives ahead of the higher energy blue portion. This is due to the effects of dispersion in the transmissive optics in the NOPA, and additional chirp is added by optics further along the beam path, including neutral density (ND) filters, wave plates, cryostat windows, etc. This positive chirp must be offset with a negatively dispersive process to minimize the pulse duration.

The pump pulse is passed through both prisms twice to achieve this negative dispersion. Passing through the prisms themselves induces additional positive dispersion to the pulse. However, the prisms are carefully aligned such that the refraction of light in the prisms forces a longer total propagation time for the red edge compared to the blue edge, more than offsetting the positive dispersion of the prisms and leading to a net negative dispersive effect[150]. Alternatively, negatively dispersive chirped mirrors[151] or gratings can be employed for chirp correction, or a

combination of prisms and mirrors can be used to correct for higher order terms in the dispersion and achieve even shorter pulses[129,141].

In order to properly compress the pump pulse, the angles and insertions of the prisms into the beam path are adjustable. This is done through an iterative process of moving the prisms and then measuring the pulse duration and chirp. The spectral and temporal shape of the pulse is measured using the frequency-resolved optical gating (FROG) technique[152–154]. This method involves splitting the laser pulse to be measured into two beams (here denoted "pump" and "probe" with quotation marks to clarify they are different than the TA setup pump and probe lines), which are then crossed with one another in a transparent medium, as illustrated in **Figure 2.6**. This setup has a number of parallels to the transient absorption setup found in **Figure 2.5**, and is similar to a version of pump-probe spectroscopy.

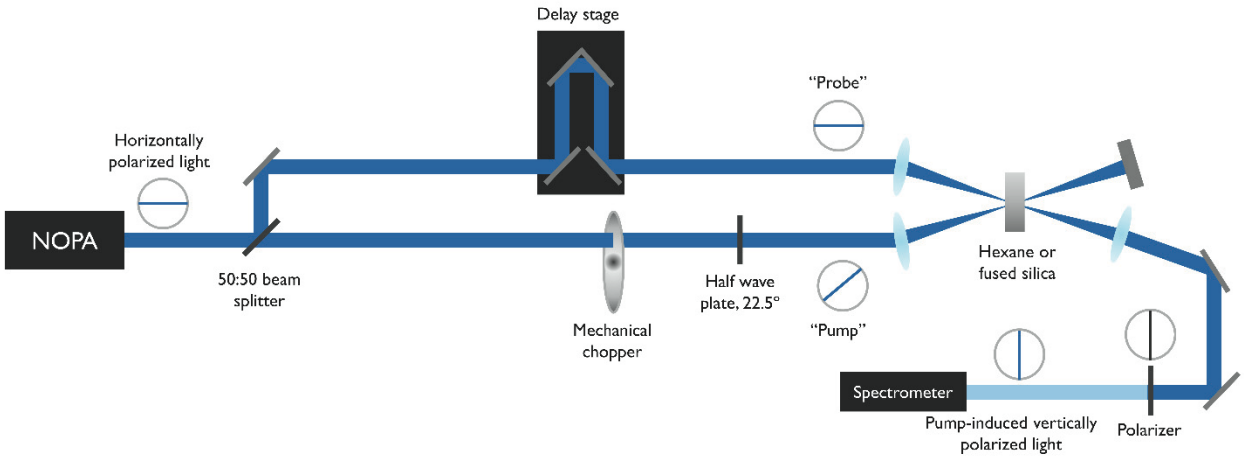


**Figure 2.6. Frequency-resolved optical gating experimental setup.** The TA pump pulse is split into two beam lines that are overlapped with one another, allowing for time- and frequency-resolved data to be collected.

The physics behind this method again utilizes the optical Kerr effect (OKE) and requires a laser pulse with a high instantaneous peak energy in order to induce nonlinear optical properties in a sample. The "probe" pulse (one half of the TA pump beam) is horizontally polarized, but routed to a spectrometer only after passing through a vertical polarizer. Thus, effectively no "probe" light reaches the spectrometer in the "pump off" condition. The other half of the TA pump beam, the "pump" line here, is rotated to a 45° polarization using a half-wave plate. When this

beam is focused into a hexane or fused silica sample, it induces birefringence in the material by the OKE. This birefringence rotates the polarization of the "probe" beam, allowing some of it to pass through the vertical polarizer and into the spectrometer, but only when the "pump" is on[154]. By using a mechanical chopper to alternate between "pump on" and "pump off" conditions and taking a differential measurement with the spectrometer as a function of time delay, a time- and frequency-resolved plot of the TA pump beam interacting with itself can be measured, as shown in **Figure 2.7** (top row).

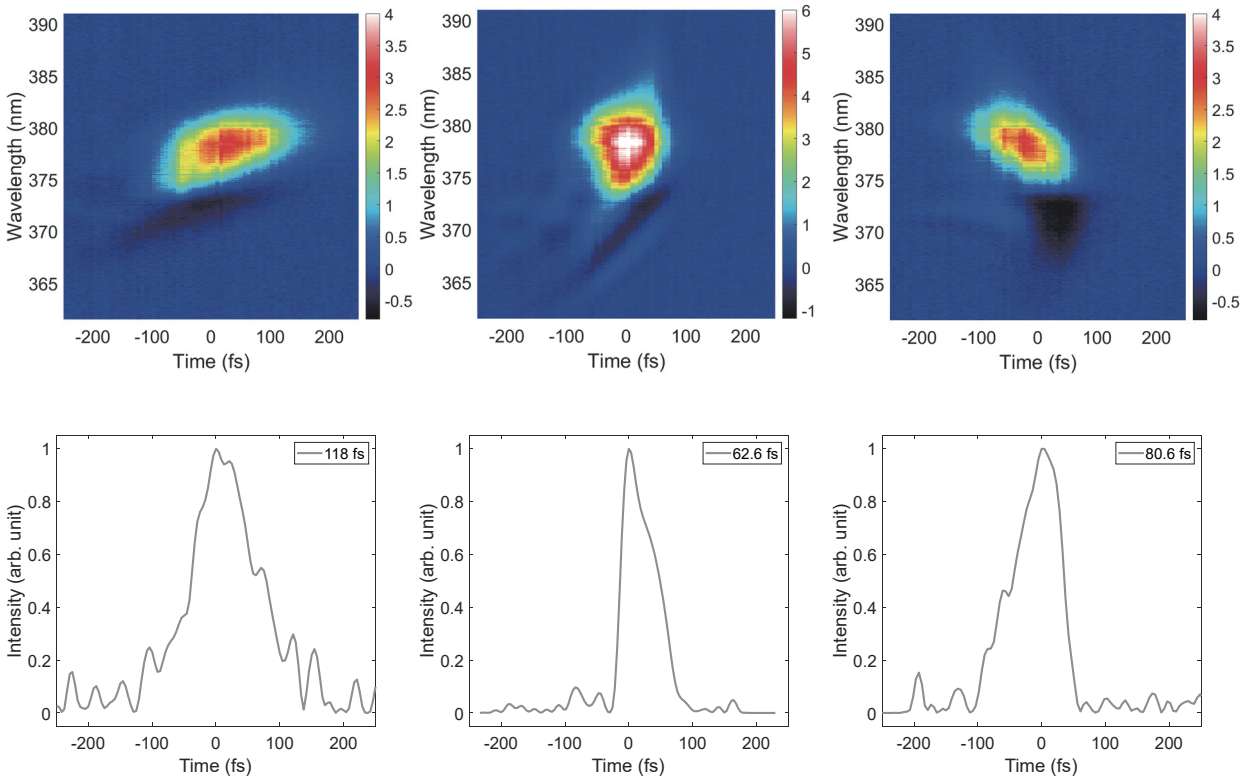


**Figure 2.7. Example frequency-resolved optical gating (FROG) data.** The data were collected at three different prism positions, corresponding to overcompensated (left), fully compressed (center), and undercompensated (right) ~375 nm pump pulses. Data taken by inducing birefringence in 2 mm fused silica using the OKE. The top row shows 2D plots of raw, convolved FROG data; the bottom row shows the 1D pulse autocorrelation spectrum after the deconvolution algorithm is completed.

The 2D FROG data must then be deconvolved to recover the actual 2D spectrogram of the pump pulse. Here we are greatly indebted to the Trebino group at the Georgia Institute of Technology for making their FROG deconvolution algorithm and code available to the public[155].

This code employs a 2D phase retrieval algorithm that performs an iterative series of Fourier transforms on the FROG data[154]. We are able to reformat our collected data into an appropriate input for the Trebino code and run it as is, resulting in a fast and efficient measurement of the pump pulse spectrogram. The prism positions are then adjusted until a fully compressed pulse with the shortest possible duration is achieved, as shown in **Figure 2.7**. We also briefly note that a similar method to FROG, a pump-probe cross correlation, is used to measure the probe pulse spectrogram and correct for the probe chirp in the analysis of collected TA data.

## 2.6 Transient Absorption Experimental Setup

Returning to the remaining optical components shown in **Figure 2.5**, the pump beam passes through a half-wave plate and polarizer after the pulse compressor. These optics enable us to perform polarization-selective transient absorption experiments. One type of experiment compares the TA signal between two cases, one where the pump and probe share the same polarization and the other where they have different polarizations. This extracts information about the rate at which charge carriers or excited structures reorient themselves upon photoexcitation[156,157]. Alternatively, orientation dynamics in molecular systems can be excluded from TA data using magic angle polarization[158]. In our experiments, both the pump and probe beams are normally maintained at a horizontal orientation.

The time delay between the pump and probe is established using a motorized delay stage. This consists of a corner cube mirror mounted on a computer-controlled linear translation stage with extremely fine positioning control and accuracy of <10 μm. This allows us to control the pump-probe delay by changing the pump path length and converting travel distance to travel time using the speed of light. The delay stage is 600 mm long (1200 mm round-trip), allowing for a 4 ns time window with <50 fs precision. Following the delay stage, the pump passes through a mechanical chopper. This piece of equipment allows for the concurrent acquisition of the "pump on" and "pump off" data that are subtracted to yield the differential transient absorption signal. The chopper operates at 5 kHz, such that ~20 pump pulses in a row pass through the chopper to reach the sample over a 100 μs period, then the next ~20 pump pulses are blocked by the chopper blade over another 100 μs period, and so on.

Finally, both the pump and probe beams are focused down to a ~50-500 μm diameter spot on the sample of interest using a 200 mm focal length mirror. The beams cross each other in a slightly non-collinear geometry, which allows us to precisely control the spot sizes at the point of beam overlap. This geometry also blocks the transmitted pump beam from continuing on to the spectrometer. Additionally, the sample stage allows for the use of a tower cryostat (Janis Research, ST-100), permitting temperature-dependent TA measured under inert conditions. After passing through the sample, the probe beam is recollimated and coupled to a multi-mode optical fiber. From there it is routed to one of three different spectrometers, all equipped with 1024 pixel linear CMOS camera detectors. One spectrometer has an adjustable grating that provides very fine spectral resolution (useful for autocorrelations and other measurements where slight wavelength shifts are important), while two others have coarser spectral resolution more suitable for broadband TA in the visible and near-infrared regions.

### 2.7 Transient Absorption Detection Scheme and Data Analysis

We will end the chapter with a discussion on how laser light detected by the spectrometer is converted into data that can yield conclusions about the photo-physics of semiconductor nanomaterials. The entire detection scheme is controlled with a LabVIEW program connected to a high speed data acquisition board. The raw transient absorption data is a two-dimensional data set as a function of both wavelength and time delay. To collect a single time delay data point, the delay stage is first moved to the appropriate position. The 1024 pixels in the CMOS camera then collect the entire spectrum all at one time for each time delay. As shown in **Figure 2.8**, the spectrometer is synced with the chopper and used to detect consecutive "pump on" and "pump off" windows, remaining open for 90 μs per acquisition window and collecting ~18 probe pulses over this period. This data is integrated for many cycles of the chopper, approximately one second in total, and then saved as a single time delay point containing the "pump on" and "pump off" counts as well as a calculated TA signal (as defined by **Equation 2.1**) for each wavelength pixel. The delay stage is then moved to the next time delay position and the process is repeated until all time delay positions specified by a particular TA position path have been measured, thereby creating a 2D data set of intensity versus wavelength and time. This constitutes a single TA scan; normally several scans are done per TA run in order to identify and control for sample degradation

over time. The LabVIEW script then generates a file in .bin format containing all of the raw data that was collected. Additional details on our detection setup have been reported previously by the Tisdale group[138,159].

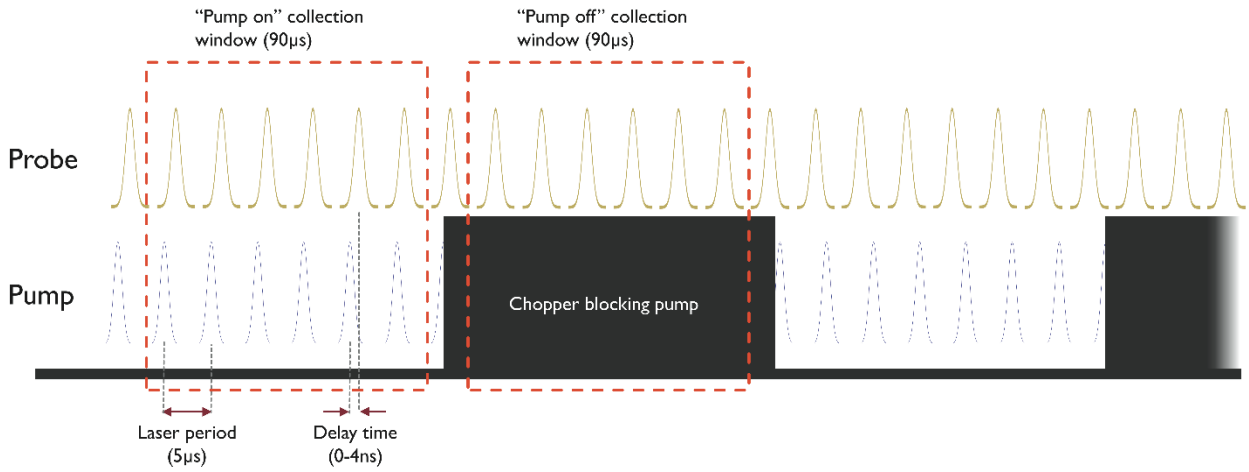


**Figure 2.8. Transient absorption detection and chopping scheme.** The top row shows the continuous train of probe pulses that pass through the sample; the bottom row shows the corresponding train of pump pulses, half of which are blocked by the chopper blade. The spectrometer collects sequential 90 μs "pump on" and "pump off" windows, each containing ~18 probe pulses (Note: only one out of every three pulses is shown here for visual clarity).

The .bin data is imported to MATLAB for further processing and data analysis. A series of nested functions have been created to achieve this. The lowest level function imports the .bin data and converts it to MATLAB-formatted matrices. The second level function applies a chirp correction and spontaneous photoluminescence background subtraction. The third level function aggregates multiple TA runs into a structure, removes erroneous data, and extracts experimental conditions. Finally, a master script is used to call these functions, generating formatted data that can easily be analyzed using a number of methods, including 2D and 1D plotting, analysis as a function of time delay/wavelength/temperature/fluence/scan count, fitting algorithms, and Fourier transforms. In this way, the newly collected transient absorption data can be quickly processed to a level where characteristics of the underlying physical mechanisms begin to emerge.

Our ultrafast broadband transient absorption spectroscopy setup allows for the study of femtosecond to nanosecond dynamics in hybrid semiconductor nanomaterials. The system is tunable over a wide range of pump wavelengths/fluences, probe/detector spectral ranges, sample

temperatures, and various other conditions, all with <100 fs temporal resolution. This system is a powerful tool for investigating a wide range of physical phenomena at the nanoscale.

# Chapter 3
# Coherent Exciton-Lattice Dynamics in a 2D Metal Organochalcogenolate Semiconductor

> *Nanomaterials have become increasingly important in the development of new materials for enhanced applications. … There is an immense quest for composite materials containing … the properties of two or more materials to create a material designed for a specific purpose.*
>
> B. Viswanathan Nano Materials[160]

*The basis of this chapter has been adapted from:*
Eric R. Powers[†], Watcharaphol Paritmongkol[†], Dillon C. Yost, Woo Seok Lee, Jeffrey C. Grossman, William A. Tisdale. "Coherent Exciton-Lattice Dynamics in a 2D Metal Organochalcogenolate Semiconductor." *In Preparation* (2023).
[†]Authors contributed equally.

## 3.1 Abstract

Hybrid organic-inorganic nanomaterials can exhibit transitional behavior that defies description by models developed for all-organic or all-inorganic materials systems. Here, we reveal the complexity of exciton-phonon interactions in a recently discovered 2D layered hybrid organic-inorganic semiconductor, silver phenylselenolate (AgSePh). Using femtosecond resonant impulsive vibrational spectroscopy and non-resonant Raman scattering, we measure multiple hybrid organic-inorganic vibrational modes and identify a subset of these modes that strongly couple to the electronic excited state. Calculations by density functional perturbation theory show that these strongly coupled modes exhibit large out-of-plane silver atomic motions and silver-silver spacing displacements. Moreover, analysis of photoluminescence fine-structure splitting and temperature-dependent peak-shifting/linewidth-broadening suggests that light emission in AgSePh is most strongly affected by a compound 99 $cm^{-1}$ mode involving the wagging motion of

phenylselenolate ligands. Finally, red-shifting of vibrational modes with increasing temperature reveals a high degree of anharmonicity arising from non-covalent interactions between phenyl rings. These findings reveal the unique effects of hybrid vibrational modes in organic-inorganic semiconductors and motivate future work aimed at specifically engineering such interactions through chemical and structural modification.

## 3.2 Introduction

Hybrid organic-inorganic materials can exhibit functionality and performance not achievable in all-organic or all-inorganic material systems alone. These hybrid materials – including metal-organic frameworks, colloidal nanocrystals, organics in sol-gel derived matrices, organic modified ceramics, and hybrid halide perovskites – have been used in many fields ranging from catalysis, photonics, functional coatings, electronics, energy, and sensing to biology, medicine, and biotechnology[161–163].

Interest in hybrid organic-inorganic semiconductors has surged recently due to remarkable optoelectronic properties and ease of fabrication by low-temperature solution-based syntheses[6,163–165]. However, a complete description of excited state dynamics in hybrid semiconductors has proven elusive due to strong charge carrier-lattice interactions[119,166–169] that defy conventional models of all-inorganic semiconductors. Moreover, excited state dynamics in low-dimensional hybrid semiconductors are further complicated by the mixed Frenkel-Wannier nature of strongly-bound excitonic states[102,170,171].

Exciton-phonon coupling in two-dimensional (2D) hybrid semiconductors has been extensively studied in 2D hybrid organic-inorganic lead halide perovskites[101,102,172,173]. Previous research in this material class has shown that the main vibrational modes that couple strongly to excitons and excited electronic states belong to the motions of inorganic frameworks, while the organic components indirectly affect the vibrational modes through structural templating[101,172,173]. However, it is unclear whether these findings are representative of all 2D hybrid semiconductors or if they are specific only to 2D lead halide perovskites, which are uniquely ionic in nature and possess relatively weak hydrogen-bonding interactions between organic and inorganic components.

Layered metal organochalcogenolates (MOCs)[64,174] are an emerging class of covalently-bonded 2D hybrid organic-inorganic semiconductors with potential applications in light emission[175–177], thermoelectricity[178], and electrocatalysis,[179] as well as in light[94,180,181], chemical[182], and thermal[183] sensing. A prototypical member of this material family is 2D silver phenylselenolate (AgSePh), comprised of a hybrid quantum-well structure[83,88,95] which exhibits a thickness-independent direct bandgap[90], strong exciton binding energy[85,86], an ultrafast picosecond photoluminescence lifetime[85,87,88,94,96], narrow-linewidth blue luminescence centered at 467 nm[84], 2D in-plane exciton anisotropy with polarized light absorption and emission[86], and robust chemical stability. Moreover, synthesis of AgSePh can be accomplished without specialized equipment and the material can be prepared as single crystals[83,88], microcrystals[88,91,92], or polycrystalline thin films[90,93,94] *via* low-temperature vapor-phase or solution-phase processes, depending on the end-use need. These attributes, combined with earth-abundant elemental composition and chemical robustness, have generated interest in AgSePh for a variety of optoelectronic applications.[180,181]

In this work, we employ a combination of steady-state and time-domain spectroscopy techniques together with density functional perturbation theory (DFPT) to develop a detailed understanding of exciton-lattice interactions in AgSePh. Understanding of exciton-phonon coupling in low-dimensional semiconductors like AgSePh reveals new opportunities for controlling optoelectronic properties through molecular engineering of hybrid organic-inorganic systems.

### 3.3 Crystal Structure, Electronic Structure, Synthesis, and Basic Optical Properties of AgSePh

AgSePh is a 2D hybrid organic-inorganic semiconductor, consisting of Ag, Se, C, and H. It crystallizes in the *C*2/*c* or *P*2$_1$/*c* space group[83,88,95] and adopts a quantum-well structure (**Figure 3.1a**) with a layer of Ag atoms located between two layers of Se atoms that are covalently bonded to phenyl (Ph) rings. Each Ag atom is surrounded by four Se atoms in a tetrahedral configuration, and each Se atom is linked to four Ag atoms and one phenyl ring oriented in the out-of-plane direction. The Ag atoms are arranged into a distorted hexagonal pattern (**Figure 3.1b**), leading to in-plane anisotropy[86] and three different Ag-Ag separation distances (3.04, 2.90 and 2.90 Å) for the *P2$_1$/c* crystal structure (the *C2/c* crystal structure has two different Ag-Ag separation

distances). Because these interatomic distances are shorter than the sum of two Ag atomic radii (3.44 Å), it is believed that Ag atoms are linked *via* argentophilic interactions[95,184]. For the remainder of this paper, these three Ag-Ag separations will be denoted $(Ag\text{-}Ag)_1$, $(Ag\text{-}Ag)_2$, and $(Ag\text{-}Ag)_3$, respectively, as defined in **Figure 3.1b**.

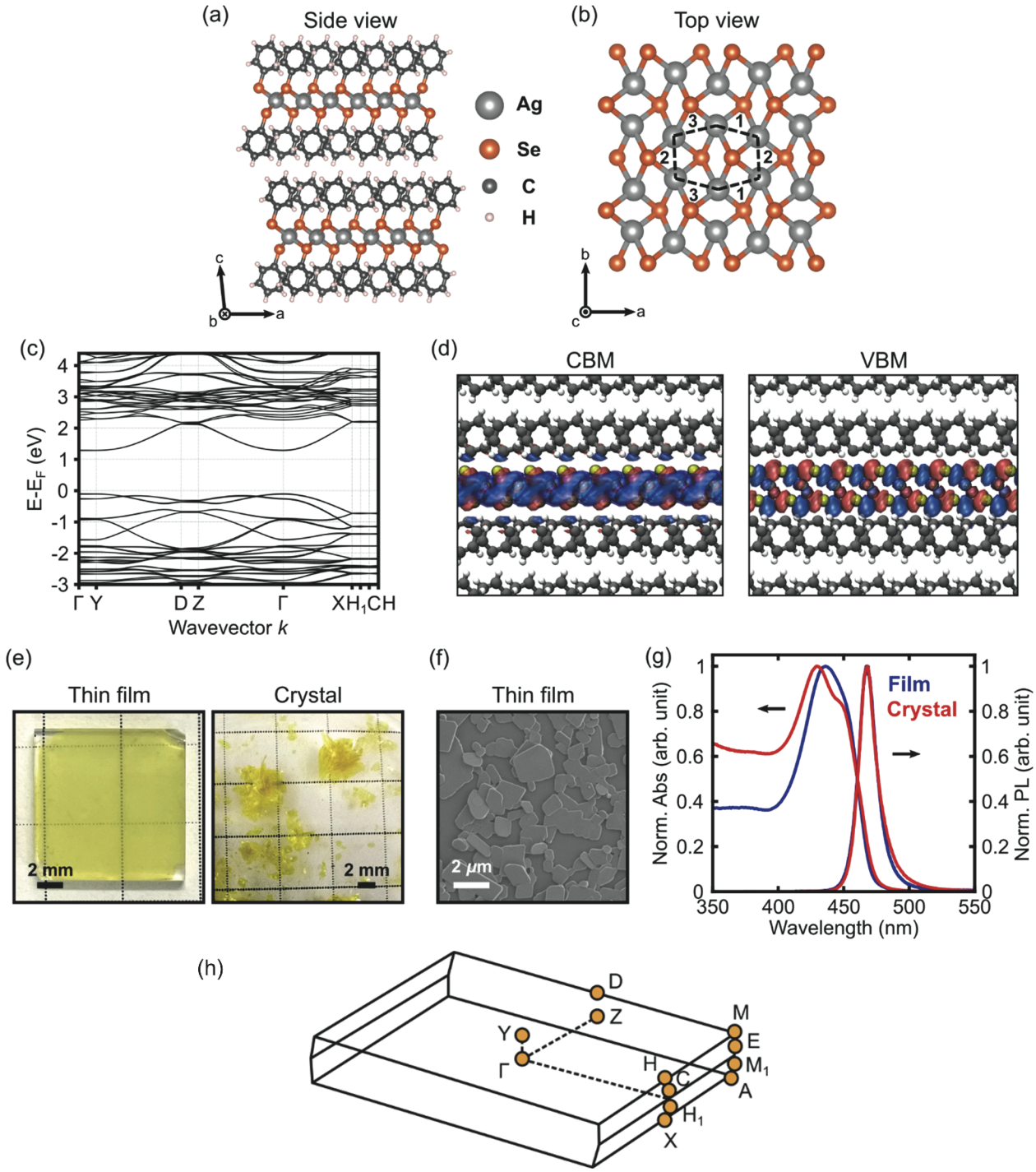


**Figure 3.1. Structural, electronic, and optical properties of AgSePh.** (a) Structure of AgSePh in $P2_1/c$ space group when viewed from the side showing a natural 2D quantum-well system. (b) Structure of AgSePh $P2_1/c$ space group when viewed from the top showing the distorted hexagonal pattern of in-plane Ag atoms and three different Ag-Ag bond lengths labeled by 1, 2, and 3. (c) Calculated electronic band structure of AgSePh derived from density functional theory, predicting a direct bandgap at Γ. (d) Isosurfaces of the wavefunctions at the conduction band minimum (CBM) and valence band maximum (VBM) at Γ. (e) Photos of an AgSePh thin film and AgSePh crystals used in this study. (f) Scanning electron micrograph of an AgSePh thin film showing its polycrystalline morphology with random in-plane orientation. (g)

Absorption and photoluminescence spectra of AgSePh thin films and crystals (powder). (h) Brillouin zone image of AgSePh adopting the $P2_1/c$ space group.

Electronic structure calculations performed using density functional theory (DFT) show that AgSePh is a semiconductor with a direct bandgap at Γ and no dispersion along the out-of-plane direction, in agreement with its quantum-well structure and a previous calculation[86] (**Figure 3.1c**). **Figure 3.1d** shows the electron densities at the conduction band minimum (CBM) and valence band maximum (VBM), which are mainly concentrated in the inorganic AgSe core. Electron density at the CBM also contains a small orbital contribution from the nearest C atoms, suggesting the possibility for electronic bandgap tunability by organic modification.

AgSePh was prepared as both thin films and large crystals, based on previously reported procedures.[88,94] AgSePh thin films (**Figure 3.1e, left**) were prepared by vapor-phase chemical transformation – or "tarnishing" – of metallic silver films by diphenyl diselenide ($Ph_2Se_2$) in the presence of dimethyl sulfoxide (DMSO) vapor.[94] A scanning electron micrograph of a representative film shows its polycrystalline nature with micrometer grain sizes and random in-plane orientation on a glass substrate (**Figure 3.1f**). Using an alternate synthetic method, large AgSePh crystals (**Figure 3.1e, right**) were obtained by an organic single-phase reaction between silver nitrate ($AgNO_3$) and $Ph_2Se_2$ in a mixed propylamine and toluene solution.[88]

**Figure 3.1g** shows the absorption and photoluminescence spectra of AgSePh thin films and crystals, revealing a crowded excitonic absorption feature at 430-450 nm comprised of three distinct optical transitions, and a single photoluminescence peak at 467 nm, in agreement with previous reports[84,86,88,94,96]. AgSePh thin films were used for femtosecond pump-probe experiments, while crystals were used for non-resonant Raman and photoluminescence spectroscopy experiments.

### 3.4 Time-domain observation of coherent exciton-lattice dynamics by impulsive vibrational spectroscopy (IVS)

To investigate vibrational dynamics in AgSePh, we employed resonant impulsive stimulated Raman scattering (RISRS)[101,102,119,168,172], a time-domain vibrational spectroscopy technique belonging to a broader class of methods known collectively as impulsive vibrational

spectroscopy (IVS). [126,132,140,141,185] Based on pump-probe transient absorption spectroscopy, IVS measures the change in a sample's absorption/transmission due to photoexcitation as a function of time (**Figure 3.2a**). In our experiment, an ultrafast 375 nm pump laser pulse was used to excite AgSePh electronically and vibrationally, followed by a broadband probe laser pulse to monitor the excited state dynamics over a controllable time delay (**Figure 3.2b**). Due to the short temporal width (~70 fs) of the pump laser pulse (**Figures 3.9 and 3.10**), a coherent vibrational wavepacket is generated on an excited-state potential energy surface upon photoexcitation, and this wavepacket evolves over time with a frequency ω corresponding to the underlying vibrational mode(s). This oscillation of the wavepacket leads to fluctuations in the atomic spacing and lattice organization, resulting in a time-dependent modulation of sample's absorption that contains information on the sample's vibrational dynamics.

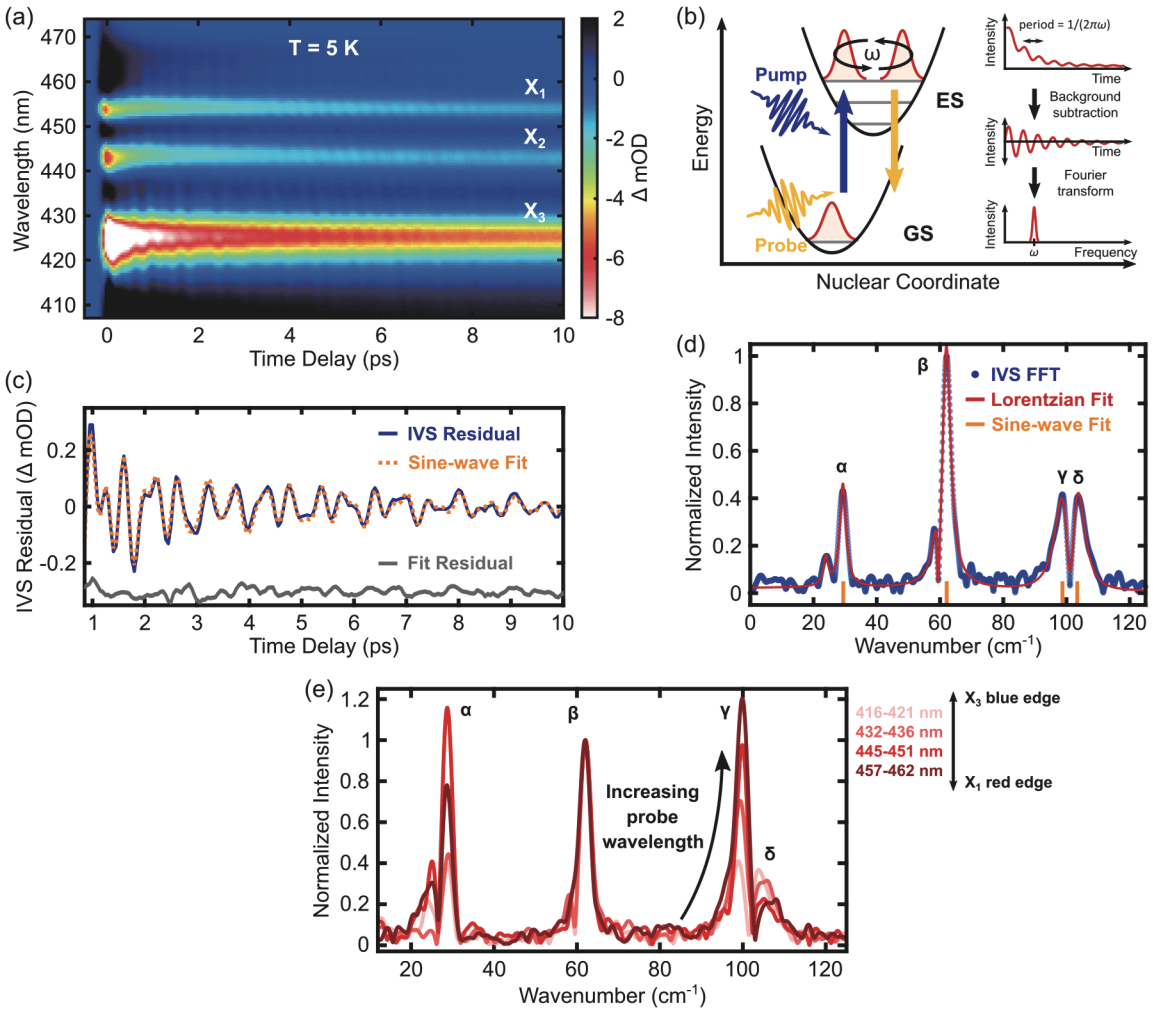


**Figure 3.2. Coherent vibrational dynamics obtained by impulsive vibrational spectroscopy (IVS).** (a) IVS color map of thin-film AgSePh at 5 K. The IVS data were collected and analyzed over a time delay of 0 to 20 picoseconds (ps), at which point all substantial oscillatory signals were found to have degraded. The data are truncated to 10 ps here for clarity; the full 20 ps color map can be found in Figure 3.15a. The three distinct excitonic transitions $X_1$, $X_2$, and $X_3$ are labeled. (b) Schematic of the IVS technique employed in a displaced harmonic oscillator potential energy system. Photoexcitation occurs from the electronic ground state (GS) to the excited state (ES) and induces a coherent vibrational wavepacket oscillating at a frequency ω. At right, the process of extracting vibrational frequency information from the IVS signal is illustrated, involving the subtraction of fitted electronic dynamics to obtain vibrational dynamics, followed by a Fourier transform to find the vibrational mode frequency. (c) Analysis of time-domain IVS data, showing the vibrational oscillations in the signal over a 408-422 nm region (blue), the fit to multiple decaying sine waves (orange), and the difference between the experimental signal and fit with an offset for clarity (gray). (d) Vibrational frequencies obtained after Fourier transformation of IVS vibrational dynamics (blue). These frequency-domain data were fit to multiple Lorentzian peaks (red) and agree with the frequencies identified by the sine-wave fit to the time-domain data (orange ticks). (e) Probe wavelength-dependent IVS vibrational frequencies showing an increase in the relative intensity of the γ mode at longer probe wavelengths.

**Figure 3.2a** shows the IVS color map for AgSePh at 5 K, plotted as the change in absorption versus time delay and probe wavelength. We observed three prominent bleach features (a negative change in absorption), labeled $X_1$, $X_2$, and $X_3$.[86,87] These three optical transitions in AgSePh were previously assigned to three distinct excitonic states oriented within the 2D plane ($X_2$ perpendicular to $X_1$ + $X_3$) and exciton binding energy ≥300 meV[86]. A fit to these excitonic dynamics and further discussion are shown in **Figure 3.3**.

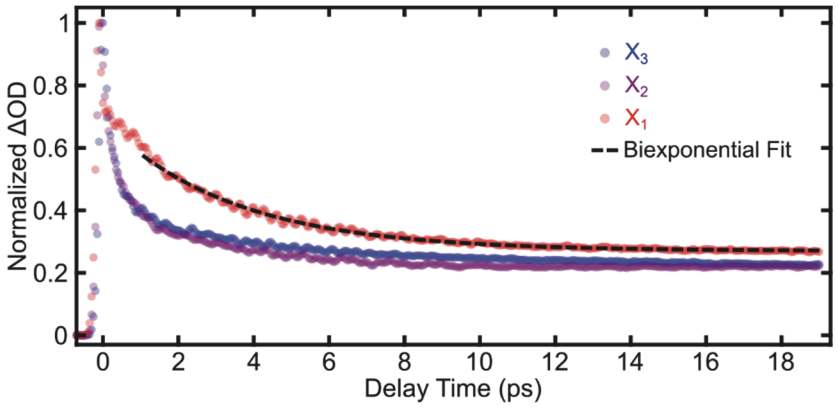


**Figure 3.3. Dynamics of the three bleach features in the AgSePh IVS spectrum at 5 K.** Dynamics for the first 0.5-1 ps consist primarily of decay from the higher energy $X_3$ (422-428 nm) and $X_2$ (440-446 nm) excitonic features to the lowest energy $X_1$ (451-457 nm) peak. The dynamics of the $X_1$ peak after 1 ps are fit with a biexponential decay, yielding a 3.4 ps fast lifetime, consistent with previously reported findings[87] and likely driven by exciton trapping or recombination through radiative and non-radiative pathways. The decay of the slow component was found to be effectively zero over the 20 ps time window, so the true long lifetime could be any value several hundred picoseconds or longer.

Superimposed on the decaying electronic signals in the IVS data are the oscillatory vibrational dynamics. To isolate the vibrational dynamics, we sum over a wavelength region of the IVS data, then fit and subtract off the electronic contribution to the signal (**Figure 3.2b** and **Figure 3.4**), leaving only the quickly oscillating vibrational signal as shown in **Figure 3.2c**. Next, a Fourier transform is applied to extract the frequencies of underlying vibrational modes (see **Appendix A** for an extended discussion on this data analysis method). **Figure 3.2d** shows the vibrational frequencies of the IVS signal at 408-422 nm.

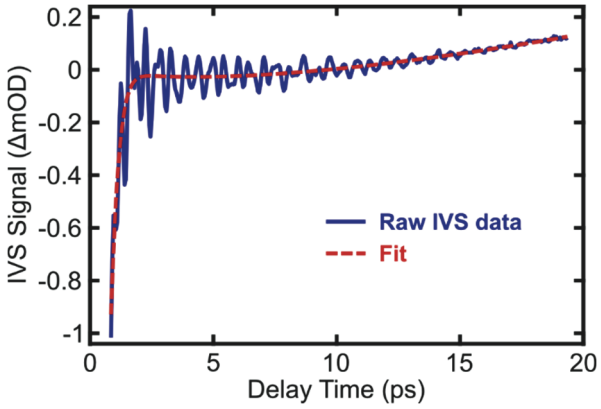


**Figure 3.4. Isolating coherent vibrational data from electronic dynamics.** The raw IVS data at 5 K extracted from Figure 3.2a is shown in blue. The fit to the data is shown in red, as discussed in Appendix A. Subtraction of the fit from the raw data yields the vibrational dynamics shown in Figure 3.2c.

We observe four dominant vibrational modes in the IVS data (**Figure 3.2d**) with frequencies of 29.3, 62.1, 98.7, and 103.7 $cm^{-1}$ labelled α, β, γ, and δ, respectively. These are the vibrational modes that significantly modulate the excitonic optical transitions in AgSePh; or, in other words, these are the primary modes that participate in exciton-phonon coupling.

The IVS results show differences in exciton-phonon coupling behavior among the three excitonic states (**Figure 3.2e**). While the β mode is the most dominant mode based on signal intensity at probe wavelengths of 416-421 nm (corresponding to the highest-energy excitonic state, $X_3$), the γ mode is most intense for the lowest-energy excitonic state, $X_1$ (probe wavelength 457-462 nm).

To corroborate the findings of the frequency-domain analysis, we also performed mode analysis directly on the time-domain data (**Figure 3.2c**) by fitting to the sum of multiple decaying sine waves of the form

$$I = \kappa_1 \sin(\omega_1 t + \varphi_1) \exp\left(\frac{-t}{\tau_1}\right) + \kappa_2 \sin(\omega_2 t + \varphi_2) \exp\left(\frac{-t}{\tau_2}\right) + \cdots, \tag{3.1}$$

where $I$ is the intensity of the IVS signal, $t$ is time, and the remaining variables represent adjustable fitting parameters. The result of a four-mode fit is shown as an orange dashed line overlaid with the original data in **Figure 3.2c**; details on the fitting method and a list of the derived fitting parameters can be found in **Appendix A** and **Table 3.5**, respectively. The orange ticks along the x-axis in **Figure 3.2d** represent the fitted sine-wave frequencies, showing good agreement with

the frequencies obtained by Fourier transformation. Beyond identification of the vibrational frequencies, the unique time-domain data collection method of IVS allows for analysis of the temporal evolution of the vibrational coherences, represented by the $\tau_i$ coherence lifetime terms in the fit and tabulated in **Table 3.1**.

### 3.5 Comparison of IVS spectrum to non-resonant Raman scattering (NRRS)

The unique information content of IVS is further revealed by comparison of the IVS spectrum to the corresponding frequency-domain non-resonant Raman scattering (NRRS) spectrum (**Figure 3.5a**). By using a non-resonant Raman pump laser wavelength of 785 nm (below the bandgap of AgSePh), we ensure that only vibrational modes belonging to the electronic ground state are observed in NRRS.

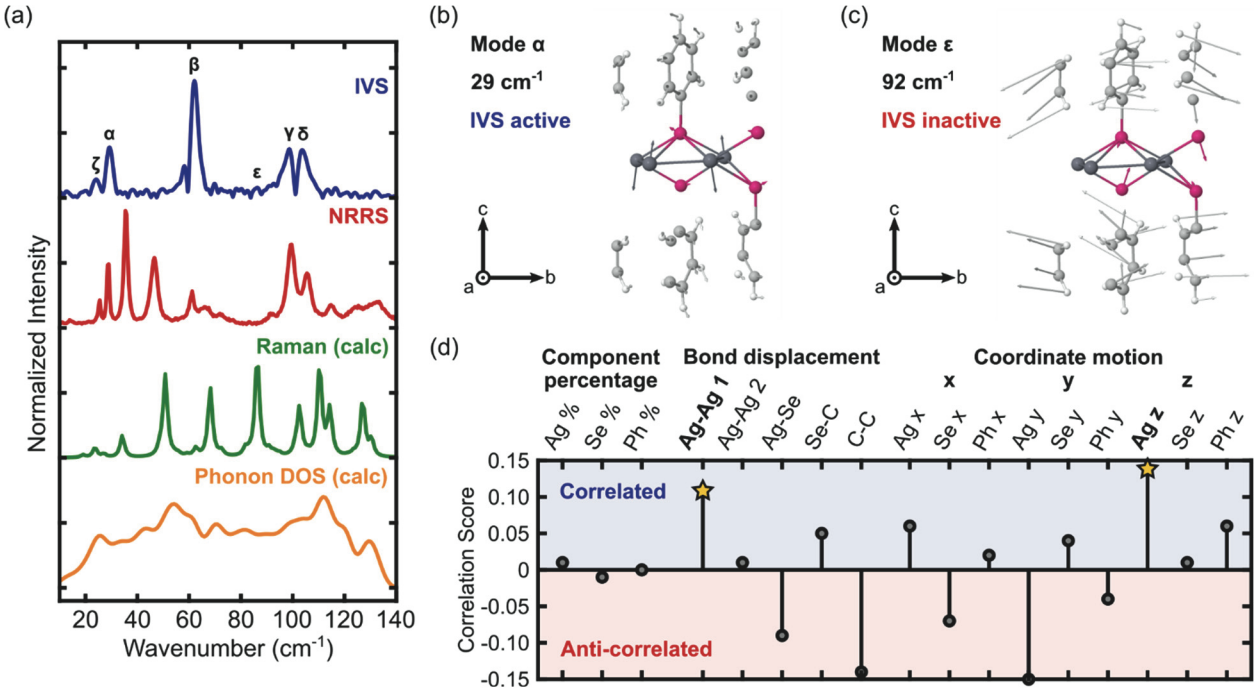


**Figure 3.5. Vibrational mode identification using density functional perturbation theory (DFPT).** (a) Comparison of vibrational spectra from several experiments and simulations, normalized and offset. Shown in order are impulsive vibrational spectroscopy (IVS, blue, 5 K), non-resonant Raman scattering (NRRS, red, 78 K), DFPT calculated Raman (green), and DFPT calculated phonon density of states (orange). See also Figures 3.19 and 3.20. (b and c) DFPT simulated atomic displacements in the AgSePh structure for the α (b) and ε (c) modes. (d) Net correlation between IVS activity and different vibrational mode characteristics in AgSePh, evaluated for the 13 identified modes between 0 and 140 $cm^{-1}$. The *x*, *y*, and *z* directions correspond to the *a*, *b*, and 5.6-degrees-off-*c* crystallographic directions, respectively.

The four primary IVS modes (α, β, γ, and δ) have corresponding peaks in the NRRS spectrum at 29.0, 61.2, 99.6, and 105.5 $cm^{-1}$, respectively (**Table 3.1**). The observation of these same four vibrational modes associated with exciton-phonon coupling by both techniques indicates that they couple to both the ground electronic state (as shown by NRRS) and the excited electronic state (as revealed with resonant IVS).

Due to the large unit cell of AgSePh consisting of 52 atoms, it is expected that many more Raman-active modes should exist in this material beyond the four modes identified by IVS. Indeed, the NRRS spectrum reveals >10 resolvable peaks in the spectral range from 0 $cm^{-1}$ to 140 $cm^{-1}$ (**Figure 3.5a**). As these vibrations are not observed in the IVS spectrum, we conclude that they correspond to Raman-active modes that do not couple strongly to the three primary excitonic transitions in AgSePh.

Another noteworthy difference between the results of the two techniques is the broadened linewidths in IVS compared to those seen in NRRS. First, we note that the linewidths are homogeneous in origin – rather than derived from sample inhomogeneity – due to the Lorentzian (rather than Gaussian) lineshapes shown in **Figure 3.2d** and **Figure 3.14**[186]. Typically, homogeneous lifetime broadening due to phonon-phonon scattering is the main contribution to linewidth broadening in Raman spectroscopy, including NRRS and IVS. In addition to this contribution, the IVS linewidth is further broadened by phonon-exciton scattering[187–189] resulting from resonant excitation of the sample. Following photoexcitation at 5 K, excitons in the two higher-energy states ($X_2$ and $X_3$) scatter into the lowest energy state ($X_1$) on a ~0.5 ps timescale, followed by a slower ~3 ps depopulation timescale for the lowest-energy state (**Figure 3.3**). These electronic lifetimes are on the same order of magnitude as the coherent vibrational lifetimes extracted from time-domain fitting of the IVS data using **Equation 3.1** (**Table 3.1**), indicating that linewidth broadening due to phonon-exciton scattering contributes significantly to linewidth broadening in resonant IVS – but not in non-resonant Raman scattering (NRRS). These fast exciton-phonon scattering rates may also contribute to the low photoluminescence quantum yield (~2%) of AgSePh at 5 K[96].

### 3.6 Mapping observed frequencies onto atomic displacements in AgSePh

To obtain a physical interpretation of the vibrational modes identified with IVS and NRRS, we compare the experimental vibrational spectroscopy results to lattice dynamics calculations performed using density functional perturbation theory (DFPT) approaches. A detailed description of how these calculations were performed can be found in the Methods section.

The calculated Raman spectrum and phonon density of states (PHDOS) are plotted alongside the experimental IVS and NRRS spectra in **Figure 3.5a**. As with the NRRS data, multiple vibrational modes were found in the calculated Raman spectrum, a subset of which are IVS active. Where possible, peak assignments between the IVS, NRRS, and calculated Raman spectra were made based on nearest frequency modes and an assumption of correspondence between the data sets, as listed in **Table 3.1** for the IVS active modes and shown in **Figure 3.6**. A complete listing of all 13 vibrational modes identified in this study over the region of interest (0-140 $cm^{-1}$) and their frequencies can be found in **Table 3.2**. We note that the peaks of interest are in the low frequency region (<140 $cm^{-1}$) and only separated by ~10 $cm^{-1}$ in several instances, whereas differences between calculated spectra and experimentally measured frequencies can be on the order of tens of wavenumbers[190] using first-principle approaches such as DFPT. A complete discussion on the possible sources of error in the computed PHDOS and Raman spectra can be found in **Appendix D**.

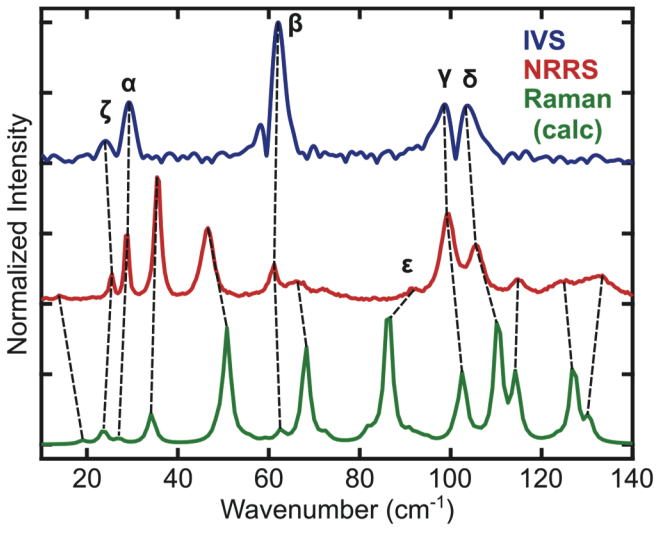


**Figure 3.6. Assignment of vibrational mode peaks between IVS, NRRS, and calculated Raman techniques.**

Using DFPT, the atomic displacements of vibrational modes in AgSePh can be visualized in real-space. Mode α, which has a clear IVS signal, is shown in **Figure 3.5b**. The motion primarily consists of silver atom motion in the *z*-direction alternating between positive and negative displacements for adjacent silver atoms. (We define the *x*, *y*, and *z* directions as corresponding to the *a*, *b*, and 5.6-degrees-off-*c* crystallographic directions). In contrast, Mode ε (**Figure 3.5c**), which presents strongly in the calculated Raman spectrum but is not observed *via* IVS, consists primarily of phenyl ring motion in the organic layer, with limited motion of the selenium atoms and almost stationary silver atoms.

To more systematically understand the modeled vibrational displacements and how they contribute to exciton-phonon coupling, we analyzed the simulated atomic motions to look for correlations with IVS activity. First, we considered the relative magnitude of atomic displacements, Cartesian-projected component motions, and changes in bond lengths. This analysis was performed on the five IVS-active and eight IVS-inactive modes that could be clearly identified and assigned in our data set. Relative contributions of selected atomic motions to the key vibrational modes are presented in **Table 3.1**; a complete list of motional contributions to all 13 of the mapped vibrational modes can be found in **Tables 3.3 and 3.4**.

**Table 3.1. Summary of experimental and simulation results describing key vibrational modes in AgSePh.** See also **Tables 3.2, 3.3, and 3.4**.

| Mode Designation | NRRS at 78 K ($cm^{-1}$) | IVS at 5 K ($cm^{-1}$) | Calculated Raman ($cm^{-1}$) | IVS Lifetime at 5 K (ps) | $(Ag\text{-}Ag)_1$ Displacement Contribution[a] | Ag *z* -Motion Contribution[b] |
|---|---|---|---|---|---|---|
| Zeta (ζ) | 25.5 | 24.1 | 23.7 | - | 0.45 | 0.28 |
| Alpha (α) | 29.0 | 29.3 | 27.1 | 4.6 | 0.30 | 0.38 |
| Beta (β) | 61.2 | 62.1 | 62.6 | 4.7 | 0.41 | 0.07 |
| Epsilon (ε) | 91.5 | - | 86.3 | - | 0.30 | 0.02 |
| Gamma (γ) | 99.6 | 98.7 | 102.7 | 2.4 | 0.39 | 0.04 |
| Delta (δ) | 105.5 | 103.7 | 110.4 | 3.4 | 0.35 | 0.03 |

[a]*Column value indicates atomic mass-weighted contribution of the specified displacement to total atomic displacements involved in the mode. All weighted displacements add to a value of 1.0.* [b]*Column value indicates atomic mass-weighted contribution of the specified directional motion to the total of all atomic directional motions. All weighted directional motions add to a value of 1.0.*

Next, the motional contributions to all modes identified using DFPT were compared to generate a correlation score predicting which atomic motions are most strongly correlated with IVS activity. The correlation score is effectively a predictor of exciton-phonon coupling in AgSePh, estimating the degree to which certain atomic displacements are likely to impact the electronic structure of the material. A high correlation score indicates that a particular atomic displacement is likely to be important in exciton-phonon coupling. **Figure 3.5d** shows the correlation scores for each characteristic we evaluated, with more positive scores indicating stronger correlation. Full details on the method for calculating and assigning correlation scores can be found in **Appendix B**.

The strongest correlation with IVS signal is found for Ag motion in the *z*-direction. In **Figure 3.1d**, we established that the band edge electron densities are contained predominantly within the inorganic 2D plane, making it intuitive that Ag displacements in the *z*-direction (out of the 2D plane) are likely to disrupt the electronic structure of the inorganic layer. The second strongest correlating motion is the change in $(Ag\text{-}Ag)_1$ interatomic bond spacing. As illustrated in **Figure 3.1b**, the $(Ag\text{-}Ag)_1$ bond is found within the 2D inorganic plane and oriented predominantly along the *x*-axis. This reveals that changes in atomic spacing between neighboring Ag atoms interrupt Ag orbital overlap, and that this bond contributes significantly to the band edge electronic structure of AgSePh. Overall, we note the similarity of behavior observed here in AgSePh to exciton-phonon coupling in other 2D semiconductors. Specifically, out-of-plane homopolar phonons and in-plane polar optical phonons have been identified as the most significant contributors to exciton scattering in other 2D semiconductors,[187,191,192] agreeing with identification here of Ag motion in the *z*-direction and $(Ag\text{-}Ag)_1$ interatomic bond spacing, respectively, as important displacements. Additionally, these results corroborate a recent finding from Schriber *et al.*[95], who conclude that bonding among the 2D network of Ag atoms is important for light emission in AgSePh and in two related compounds, AgSPh and AgTePh.

Returning to the modes previously introduced in **Figure 3.5b** and **Figure 3.5c**, we see in **Table 3.1** that Mode α exhibits a much larger Ag *z*-directed atomic displacement contribution than Mode ε, helping to explain why there is a greater degree of exciton-phonon coupling in Mode α than Mode ε, as measured with IVS.

### 3.7 Vibrational modes strongly influencing light emission

To identify which modes strongly influence the luminescence properties of AgSePh, we performed temperature-dependent photoluminescence (PL) spectroscopy on AgSePh crystals. **Figure 3.7a** shows a map of intensity-normalized PL spectra of AgSePh from 5 to 300 K in 5 K increments. With increasing temperature, the PL initially blue-shifted from 5 to 30 K before reversing direction and red-shifting from 30 K to 300 K. The shift was smooth without an abrupt change in position, suggesting an absence of phase transitions in this temperature range. Concurrent with the gradual peak shift, the PL linewidth monotonically broadened as a function of temperature, as expected for a lineshape influenced by exciton-phonon coupling effects.

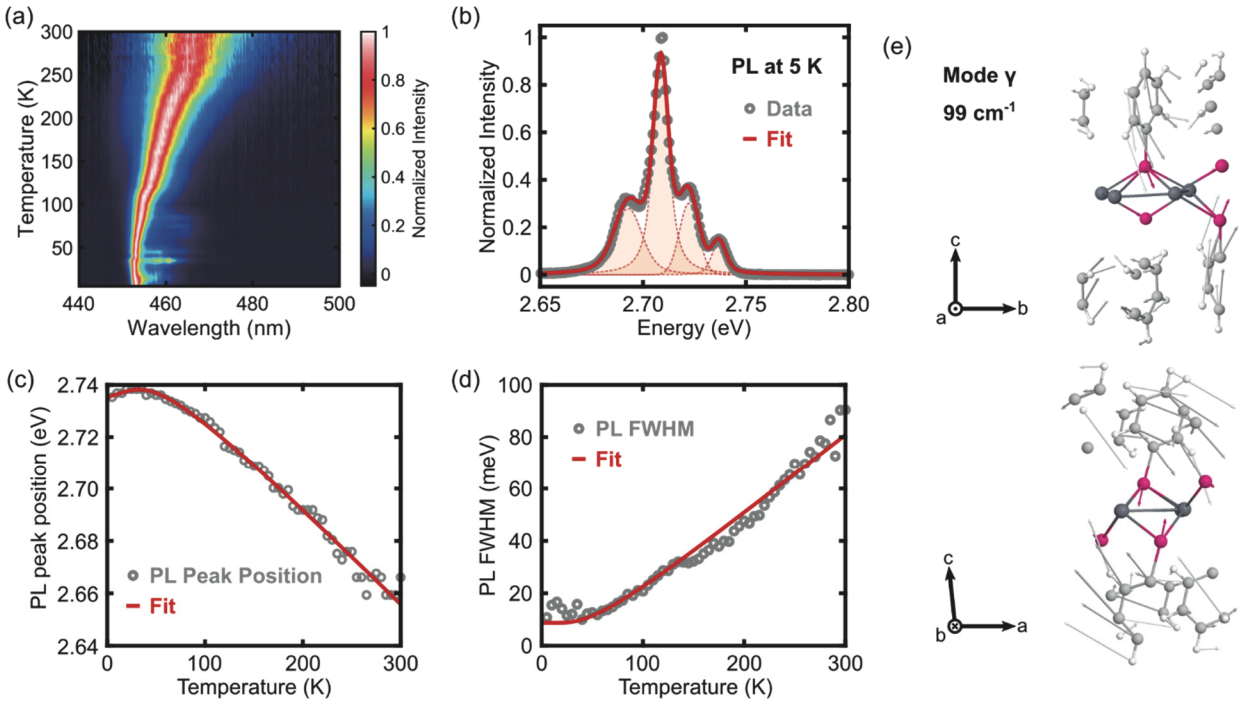


**Figure 3.7. Exciton-phonon coupling affecting light emission in AgSePh.** (a) Intensity-normalized temperature-dependent photoluminescence spectra from 5 to 300 K in 5 K steps. (b) Photoluminescence spectrum at 5 K showing peak splitting and their fits to Voigt functions centered at 2.6928, 2.7087, 2.7223, and 2.7367 eV. (c) Temperature-dependent photoluminescence peak shift and corresponding fit to Equation 3.2. (d) Temperature-dependent photoluminescence linewidth broadening and corresponding fit to Equation 3.3. (e) DFPT-simulated lattice displacements of mode γ (98.7 $cm^{-1}$ or 12.2 meV) viewed along two different in-plane axes.

At very low temperature, the emission spectrum of AgSePh split into multiple peaks and as many as four distinct optical transitions could be resolved at 5 K (**Figure 3.7b**). Fitting of these four peaks to Voigt functions results in peak energies of 2.6928, 2.7087, 2.7223, and 2.7367 eV, yielding peak energy separations of 15.9, 13.6, and 14.5 meV (128, 110, and 117 $cm^{-1}$), respectively. The roughly constant separation in energy suggests the origin of peak splitting to be phonon sidebands[193] arising from strong interaction between an exciton and a dominant phonon having an energy of ~13-16 meV (~105-129 $cm^{-1}$).

An analysis of the temperature-dependent PL peak shift can be used to extract the energy of the vibration most strongly coupled to the excitonic state responsible for light emission. Assuming a quasi-harmonic oscillation and a temperature-independent exciton binding energy, the temperature dependent electronic band gap (*i.e.* quasiparticle gap) of a semiconductor at constant pressure, $E_g(T)$, can be described by[194,195]

$$E_g(T) = E_0 + A_{TE}T + A_{EP}\left(\frac{2}{\exp\left(\frac{E_{ph}}{k_B T}\right) - 1} + 1\right), \tag{3.2}$$

where $E_0$ is an unrenormalized band gap, $A_{TE}$ determines the weight of thermal expansion interaction, $A_{EP}$ accounts for the strength of exciton-phonon interaction, $E_{ph}$ is the energy of a dominant phonon, and $k_B$ is the Boltzmann constant. Assuming a temperature-independent exciton binding energy, a fit of **Equation 3.2** to the temperature-dependent peak position of AgSePh (**Figure 3.7c**) yields an $E_0$ of 2.770 $\pm$ 0.004 eV, $A_{TE}$ of 0.12 $\pm$ 0.11 meV/K, $A_{EP}$ of -35.2 $\pm$ 3.3 meV, and $E_{ph}$ of 12.3 $\pm$ 2.8 meV.

To further confirm the fitted phonon energy, $E_{ph}$, we applied the value extracted from the peak-shift analysis (**Figure 3.7c**) to an analysis of the temperature-dependent PL linewidth broadening of AgSePh. **Figure 3.7d** compares the PL full width at half maximum (FWHM) as a function of temperature to the predicted broadening. We found that the PL FWHM was well-fitted by a model comprised of a temperature-independent linewidth, $\Gamma_0$, and a contribution from a single vibrational mode with an energy of 12.3 meV[196–198]:

$$\Gamma_{homo}(T) = \Gamma_0 + \frac{\Gamma_{ph}}{\left[\exp\left(\frac{E_{ph}}{k_B T}\right) - 1\right]}. \tag{3.3}$$

Here, $\Gamma_{ph}$ is an exciton-phonon coupling strength parameter, and $\Gamma_0$ and $\Gamma_{ph}$ were found to be $9 \pm 1$ meV and $44.0 \pm 1.0$ meV, respectively.

Overall, these findings indicate that a single dominant vibrational mode having energy of ~12-16 meV (~97-129 $cm^{-1}$) is responsible for the low-temperature PL spectral splitting, the temperature-dependent peak shifting, and the temperature-dependent linewidth broadening in AgSePh. Further, we see agreement between the exciton-phonon coupling behavior determined from PL analysis and the excitonic state-dependent IVS vibrational spectrum in **Figure 3.2e**, which showed that the γ mode at 99 $cm^{-1}$ dominates coherent lattice dynamics of the $X_1$ state.

The $X_1$ state is the lowest-energy excitonic state in AgSePh and also the state responsible for light-emission[86,96]. In **Figure 3.2e** we observed that the β mode at 62 $cm^{-1}$ was the dominant mode for the highest energy excitonic state ($X_3$) based on IVS signal intensity, while the γ mode at 99 $cm^{-1}$ was the highest intensity peak for the lowest-lying excitonic state ($X_1$). The relative coupling strength of the γ mode may also be underestimated because the intensity of an IVS peak is expected to vary inversely with the square of vibrational frequency ($I \propto 1/\omega^2$)[173,199]. **Figure 3.7e** shows the calculated vibrational motion of the γ mode viewed from two orthogonal in-plane directions. Overall, the γ mode is a strongly hybridized mode involving the alternating rocking of phenyl rings and corresponding displacement of Se and Ag atoms in both in-plane and out-of-plane directions.

### 3.8 Temperature-dependent vibrational dynamics

Impulsive vibrational spectroscopy (IVS) was performed as a function of sample temperature from 5 K to 200 K using the same experimental setup and conditions discussed previously (see **Figure 3.15**). The time-domain vibrational dynamics as a function of temperature are displayed in **Figure 3.8a**. We focus here on the blue edge of the highest energy excitonic peak ($X_3$) because it has the highest signal-to-noise ratio across the widest temperature range (specific wavelength ranges and other details are included in **Appendix A**). At each temperature, the time-domain vibrational dynamics were fit to the sum of four exponentially decaying sine waves. Fits to the data and a summary of the fitting parameters for all temperatures can be found in **Figure 3.18** and **Table 3.5**, respectively. Vibrational dephasing times for the four dominant IVS modes are plotted in **Figure 3.8b** as a function of sample temperature. Overall, dephasing becomes faster

at higher temperatures, as expected due to increasing population of the incoherent phonon bath with increasing temperature.[200]

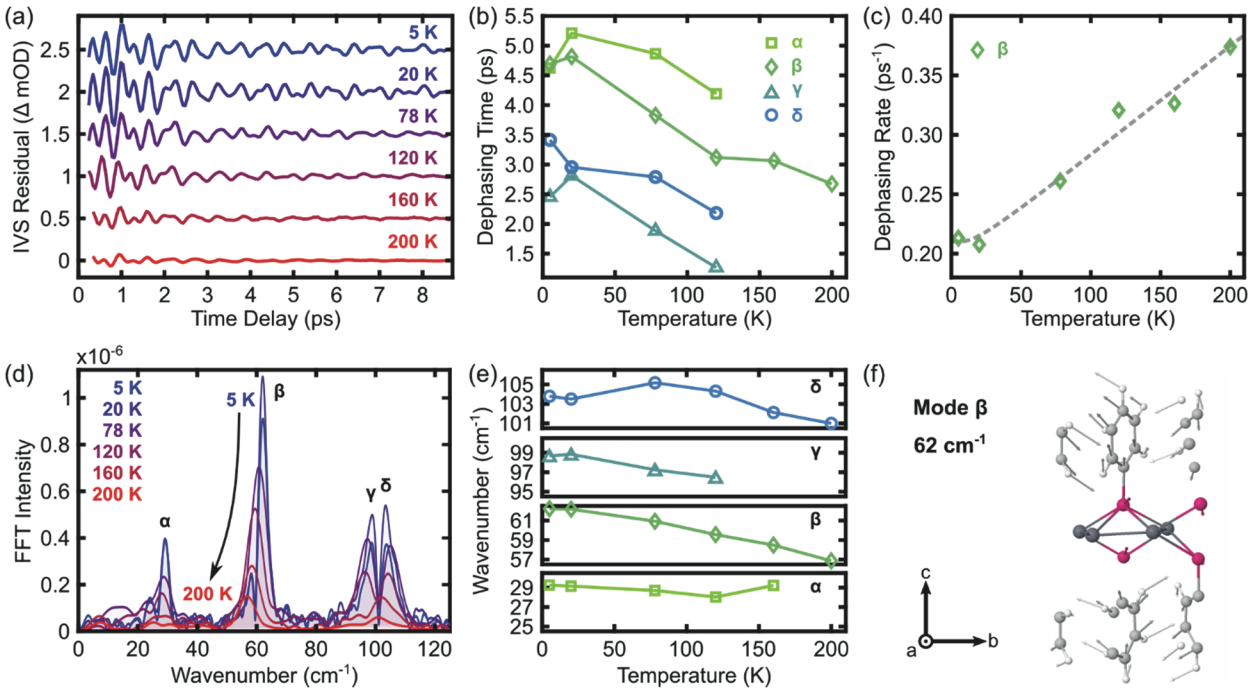


**Figure 3.8. Temperature-dependent vibrational dynamics.** (a) Time-domain IVS coherent vibrational response from 5 K to 200 K. (b) Temperature-dependent dephasing times for the four primary IVS-active modes, determined by fitting the data in (a) to the sum of four decaying sine waves. (c) Dephasing rate of the β mode as a function of temperature, fitted with a cubic overtone model. (d) Temperature-dependent IVS spectrum obtained by Fourier transform of the curves in (a). See also Figure 3.17. (e) Dependence of IVS mode frequency on sample temperature. Note that some peaks become irresolvable at higher temperatures, leading to series truncation. (f) Real-space displacements of the β vibrational mode, showing shearing motion of adjacent phenyl rings.

Temperature-dependent dephasing rates can be fit to a cubic overtone model, in which one coherent optical phonon decays into two acoustic phonons of equal energy and opposite wave vectors.[200,201] This model provides a simplified picture of vibrational dephasing, but yields a useful measure of anharmonic coupling strength[200] and the relative magnitude of different sources of dephasing. We focus on the 62 $cm^{-1}$ mode as it is the best resolved feature in the IVS spectrum, especially at higher temperatures.

The dephasing rate (or the inverse of the dephasing lifetime) is fitted to the cubic overtone model using

$$\Gamma = \Gamma_0 + \gamma_0 \left[ 1 + \frac{2}{\exp\left(\frac{\hbar\omega}{2k_B T}\right) - 1} \right], \tag{3.4}$$

where $\Gamma_0$ is a temperature-independent scattering rate (*i.e.* defect scattering), $\gamma_0$ is the anharmonic coefficient, and $\omega$ is the vibrational mode frequency. As shown in **Figure 3.8c**, this model successfully captures the observed trend in dephasing rate with fitting parameters of $\Gamma_0$ = 0.190 ± 0.025 $ps^{-1}$ and $\gamma_0$ = $2.1\times10^{-2}$ ± $0.4\times10^{-2}$ $ps^{-1}$, suggesting that both temperature-dependent and temperature-independent sources of scattering are significant. Again, we note that the exciton lifetime is <10 ps at all temperatures, and on the same order of magnitude as the vibrational coherence time (see **Figure 3.16**). Coherent vibrations on the electronic excited potential energy surface would likely be scattered by an electronic transition back to the ground state, limiting the conclusions that can be reached with a phonons-only analysis.

Temperature-dependent IVS spectra (obtained by Fourier Transform of the time-domain data shown in **Figure 3.8a**) are displayed in **Figure 3.8d**. These curves show notable shifts in peak width and position as a function of temperature, and the magnitude of these shifts varies among the different vibrational modes. Peak broadening results directly from homogeneous lifetime broadening, as discussed in the preceding paragraph. Additionally, we observe a temperature-dependent frequency shift of all modes (**Figure 3.8e**), revealing the role of mode anharmonicity[202].

Of the modes appearing in the IVS spectrum, the β mode exhibits the largest temperature-dependent frequency red-shift ($\Delta\omega/\omega$ = 9% from 5 K to 200 K). Atomic displacements of the β mode are illustrated in **Figure 3.8f**. This mode is dominated by a shearing motion of the phenyl rings, which slide past each other in alternating fashion. In contrast, the α mode (**Figure 3.5b**) – which showed the smallest temperature-dependent frequency shift ($\Delta\omega/\omega$ = <1% from 5 K to 160 K) – consists primarily of Ag atomic motion in the *x*- and *z*-directions, with minimal contribution of the phenyl rings. These findings suggest that the covalently-bound silver atoms within the inorganic 2D plane exist in a more harmonic displacement potential than the phenyl rings, which interact with adjacent rings *via* co-facial van der Waals attractive forces and steric repulsive forces, leading to a greater degree of anharmonicity for the β mode.

When compared to other material systems, these findings clearly reveal the truly hybrid nature of layered 2D AgSePh. Over a 5 K to 200 K temperature range, the anharmonic frequency shift of the dominant modes in AgSePh (~0-9%) is much larger on average than purely inorganic crystalline systems (~1-2%)[203–206] but smaller than crystalline polycyclic aromatic organic molecules like anthracene and naphthalene (~7-20%)[207]. Further, the β mode—which most heavily involves motion of the organic phenyl moiety—has an anharmonic frequency shift in the range reported for the organic molecules, while the α mode—primarily confined to the inorganic sublayer—shows a frequency shift more in-line with the fully inorganic systems.

### 3.9 Conclusions

Overall, our results provide new insight into exciton-phonon interactions in AgSePh and, more broadly, in low-dimensional hybrid organic-inorganic semiconductors. The unique electronic structure of AgSePh, showing three distinct excitonic features, allows for varying degrees of exciton-phonon coupling among different excitonic states and the vibrational modes of the system. The combination of IVS, PL, and DFPT techniques enabled identification of the γ mode – characterized by complex atomic displacements throughout the AgSePh structure and wagging phenyl motion – as the mode most strongly coupled to the emissive $X_1$ state. Moreover, temperature-dependent IVS revealed increased mode anharmonicity in hybrid organic-inorganic AgSePh compared to all-inorganic crystals, especially for vibrational modes that involve significant motion of the phenyl ring (such as the β mode). Finally, these experiments highlight the detailed information that can be obtained by integrated time-domain, frequency-domain, and computational efforts to understand exciton-phonon interactions in hybrid nanomaterials.

These findings also suggest the ability to tune optoelectronic properties of metal organochalcogenolates through synthetic modification like chalcogen substitution[86,95,96] or functionalization of the organic layer[85,88,97]. For example, modifying the phenyl rings to create steric hindrance or allow for interlayer cross-linking may increase the rigidity of the structure, leading to higher photoluminescence efficiency[208]. Furthermore, it may be possible to induce or suppress exciton-phonon interactions to realize targeted properties like minimized broadband emission from self-trapped excitons[87,96,121] or improved charge-carrier screening and transport

properties *via* polaron formation. Finally, engineering excitonic behavior through molecular doping of the organic layer may offer an orthogonal route to achieve desired performance[50,108].

### 3.10 Methods

**Synthesis of AgSePh thin films.** Thin films of silver phenylselenolate (AgSePh) for ultrafast spectroscopy were made by chemical transformation of metallic silver with an organic diselenide vapor in the presence of a solvent vapor[90,94]. Metallic silver (Ag) films with thickness of 10 nm were deposited on single-crystal quartz substrates using a thermal evaporator. Each silver film was sealed inside a microwave reaction vial along with two culture tubes separately containing ~30 mg diphenyl diselenide ($Ph_2Se_2$) and 200 µL dimethylsulfoxide (DMSO). The sealed reaction vessels were heated in an oven at 100 °C for 5 days, yielding yellow films of AgSePh.

**Synthesis of AgSePh crystals.** Large (~millimeter) AgSePh crystals for Raman and PL spectroscopy were synthesized by an organic single-phase reaction[88] by mixing 5 mL of 10 mM $AgNO_3$ solution in propylamine ($PrNH_2$) with 5 mL of 10 mM $Ph_2Se_2$ solution in toluene and holding at room temperature for 5 days.

**Optical absorption spectroscopy.** Optical absorption measurements were performed on AgSePh thin films in transmission mode using a Cary 5000 UV-Vis-NIR spectrophotometer, and on ground crystal powders using the same spectrophotometer with a PIKE Technologies DiffuseIR accessory. For the measurements on ground crystals, solid samples were prepared by grinding with dry potassium bromide (KBr) to a ~1 wt% dilution, and diffuse reflectance spectra were normalized to a 100% KBr baseline. The obtained diffuse reflectance spectra were converted into absorption spectra using the Kubelka-Munk transform[209], $F(R) = \frac{(1-R)^2}{2R}$,where $F(R)$ is the Kubelka-Munk function having a value proportional to the sample's absorption coefficient, and $R$ is the relative reflectance of the sample with respect to the 100% KBr baseline.

**Photoluminescence spectroscopy.** Photoluminescence measurements were performed on AgSePh crystals using an inverted microscope (Nikon, Ti-U Eclipse). Samples were mounted on a cold finger in a microscopy cryostat (Janis Research, ST-500) and cooled by flowing liquid helium. A 405 nm laser diode (Picoquant, LDHDC-405M, continuous wave mode) was used for photoexcitation, and the emission spectrum was imaged through a spectrograph (Princeton

Instruments, SP-2500) mounted with a cooled charge-coupled detector (Princeton Instruments, Pixis).

**Non-resonant Raman scattering (NRRS).** Non-resonant Raman spectra were collected in a backscattered geometry on the same microscopy setup used for photoluminescence measurements. A 785 nm narrow-band continuous-wave laser (Ondax) was used as an excitation source and the scattered laser light was passed through a set of volume holographic grating notch filters (Ondax) before being directed into the spectrograph mounted with the cooled charge-coupled detector. The role of the notch filters is to suppress the Rayleigh scattering, allowing an accurate measurement of vibrational modes to <10 $cm^{-1}$. The resolution of the system is approximately 0.5 $cm^{-1}$.

**Resonant impulsive vibrational spectroscopy (IVS).** A 375 nm wavelength pump pulse at 200 kHz repetition was used to excite the sample. Unless otherwise noted, the pump power was 1100 μW, which corresponds to 5.5 μJ/pulse. A broadband laser pulse covering at least the 405-485 nm spectral region with a power of <100 μW was used to probe the sample after a variable time delay from the excitation. A probe spot size of approximately 7900 $\mu m^2$ was used with the pump spot being slightly larger, leading to an excitation density of approximately $3.0\times10^5$ photons/$\mu m^2$/pulse. The pump pulse duration was 71.2±0.8 femtoseconds (fs) full width at half maximum (FWHM) as measured by frequency resolved optical gating (FROG) utilizing the optical Kerr effect (OKE).[154] Further details on the experimental setup and pulse duration measurement can be found in **Appendix A**.

**Density Functional Theory calculations.** Density functional theory (DFT), phonon density of states (PHDOS), and Raman spectra calculations were performed using the VASP planewave pseudopotential code[210–213]. A full structural relaxation of the experimentally determined 52-atom primitive unit cell with an ionic force convergence threshold of $1.0 \times 10^{-7}\ eV/\text{Å}$ was performed prior to the phonon calculations. For the structural relaxation, an $8 \times 8 \times 1$ Monkhorst-Pack k-point grid with a Gaussian smearing of 0.01 eV was used. The valence electron – ionic core interactions were treated used projector augmented wave (PAW) potentials [214,215]. A planewave kinetic cutoff energy of 500 eV was used. The Perdew–Burke-Ernzerhof (PBE) generalized gradient approximation to the exchange correlation functional[216] was used in all calculations. Taking the DFT-relaxed equilibrium structure, the Phonopy code[217] was used to generate $3 \times 3 \times 1$ supercell structures with atomic displacements in order to calculate the PHDOS over the

Brillouin zone. These 152 structures were then used to compute the force-constant Hessian matrix *via* the density functional perturbation theory (DFPT) capabilities in VASP[218,219]. The Phonopy code was used to post-process the calculation data, generating the simulated total PHDOS spectra, the Cartesian-direction projected PHDOS spectra, the atom-projected PHDOS spectra, and the *xyz* trajectory files of the phonon eigenmodes. The Phonopy-Spectroscopy code[220] was used in conjunction with VASP dielectric constant calculations[221–223] for the displaced structures in order to calculate the Raman intensities and simulated Raman spectrum of the vibrational modes. Visualizations of the vibrational modes were obtained using the VMD software[224]. As another point of comparison for the VASP/Phonopy calculated spectra, first principles molecular dynamics simulations were performed using the Qbox code[225], from which vibrational power spectra were calculated and found to have generally good agreement.

### 3.11 Acknowledgements

Materials synthesis and characterization was supported by the U.S. Army Research Office under Award Number W911NF-20-1-0200. Ultrafast spectroscopy experiments were funded by the U.S. Department of Energy, Office of Science, Basic Energy Sciences under Award Number DE-SC0019345. D.C.Y. was supported through an appointment to the Intelligence Community Postdoctoral Research Fellowship Program at Massachusetts Institute of Technology, administered by the Oak Ridge Institute for Science and Education through an interagency agreement between the U.S. Department of Energy and the Office of the Director of National Intelligence. This research used resources of the National Energy Research Scientific Computing Center (NERSC), a U.S. Department of Energy Office of Science User Facility operated under Contract No. DE-AC02-05CH11231. E.R.P. was supported by the US Department of Defense through the National Defense Science & Engineering Graduate (NDSEG) Fellowship Program. W.S.L was partially supported by the Seoul Broadcasting System Foundation Overseas Doctoral Program Scholarship.

## 3.12 Appendix A: IVS Experimental Methods Discussion and Additional Figures

### Impulsive Vibrational Spectroscopy Setup

Impulsive vibrational spectroscopy (IVS) was performed using a Spirit 1040-8 ultrafast laser (Spectra-Physics) operating at 200 kHz. A portion of the 1040 nm fundamental light was directed to a commercial two-stage non-collinear optical parametric amplifier (NOPA) with a second harmonic stage (Spirit-NOPA, Spectra-Physics), where it was converted to 375 nm pump light. The NOPA output was filtered using a 375 nm bandpass filter (Chroma AT375/28x), compressed using two fused silica prisms to minimize pulse duration, and modulated to an intensity of 1.1 mW using neutral density filters.

A second portion of the 1040 nm light was frequency-doubled to 520 nm in a β-barium borate (BBO) crystal. The residual 1040 nm was filtered out using a dichroic beam splitter, and the remaining ~150 mW 520 nm pulse was then focused into a 3 mm sapphire window with a 100 mm focal length lens to generate a broadband supercontinuum. The resultant white light was recollimated and filtered using either a 500 nm shortpass filter (Thorlabs) or two consecutive filters (Thorlabs notch filter 533nm, 17nm full width at half maximum FWHM; PIXELTEQ magenta color filter 544 nm, 124 nm FWHM) to create the probe pulse covering a minimum spectral range of 405-485 nm.

The pump pulse was modulated at 5 kHz using a mechanical chopper (Thorlabs), and the time delay between the pump and probe pulses was controlled using a mechanical delay stage (Newport). The pulses were overlapped using a 200 mm focal length mirror to a spot size of ~7900 $\mu m^2$ at the sample, which was mounted in a tower cryostat under vacuum (Janis Research, ST-100). The transmitted probe light was recollimated and directed to a spectrometer and high-speed data acquisition system (Ultrafast Systems) with a 90 μs collection window, corresponding to ~18 consecutive probe pulses for each successive “pump on” and “pump off” acquisition period. The displayed data were collected from a minimum of 4 different locations in the sample to confirm sample homogeneity, and approximately 8-12 scans were taken at each location to rule out significant sample degradation during data collection. A chirp correction to the data was performed based on a cross correlation of the pump and probe pulses as measured in a 2 mm fused silica

window. The photoluminescence background signal was also subtracted using an average of 5 data points from before time zero.

For pump pulse metrology, an autocorrelation was performed on the pump pulse using the optical Kerr effect in a 2 mm fused silica window. The temporal and spectral pulse profile was retrieved using the frequency-resolved optical-gating (FROG) method[154] with code adapted from the Trebino group[155] as illustrated in **Figure 3.9** and **Figure 3.10**. The measured pump pulse duration of 71.2±0.8 fs FWHM sets a theoretical upper limit of ~468 $cm^{-1}$ for the highest frequency coherent vibration that can be measured using this IVS experimental setup, although the actual value is likely lower due to effects from the transform limit of the probe pulse[128,141] and the much higher signal-to-noise ratio needed when approaching the theoretical limit.

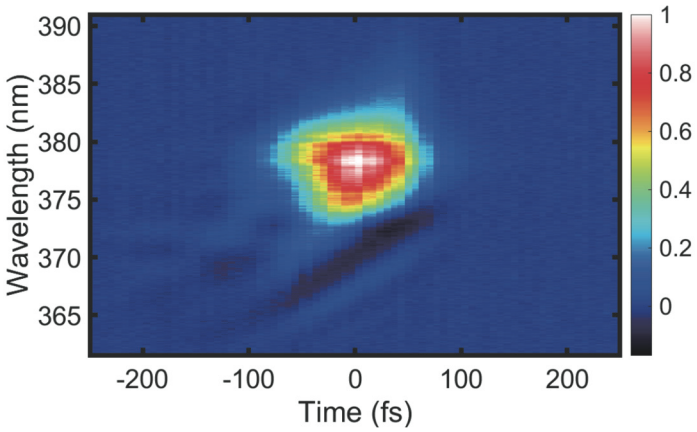


**Figure 3.9. Color map of pump autocorrelation results before deconvolution analysis.**

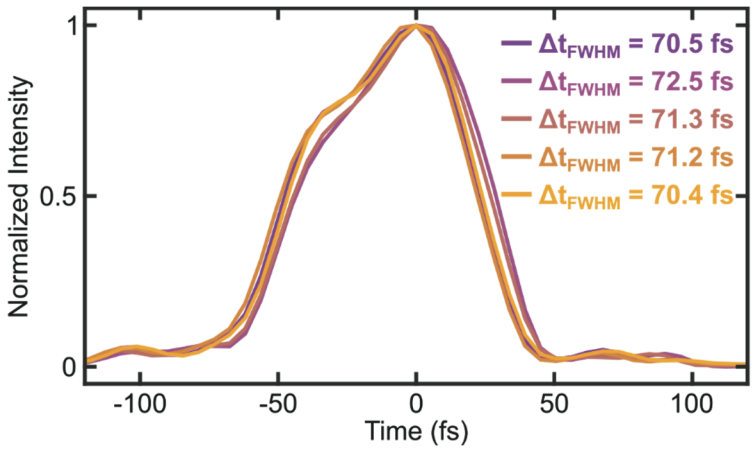


**Figure 3.10. Pump pulse temporal lineshape after execution of the FROG algorithm.** FROG analysis performed on the data shown in Figure 3.9. Different curves are the results from 5 separate runs of the FROG code using the same input data, validating the reproducibility of the algorithm.

**Impulsive Vibrational Spectroscopy Frequency Domain Analysis**

When fitting raw IVS data, the following procedure was followed. First, a wavelength region with a clear and in-phase oscillatory signal was identified in the 2D IVS data. As noted in the main text, the IVS signal is strongest near wavelengths at which the linear absorption spectrum has a high change in intensity with respect to wavelength[128]. Conversely, nodes in the IVS data and phase flips occur at the extrema of the absorption spectrum when the slope of the signal changes sign. For the complex electronic structure of AgSePh, this led to multiple nodes in the IVS signal. In the case of analyzing 5 K data, the IVS signal along the blue edge of the highest energy excitonic peak from 408 nm to 422 nm was summed to generate a one-dimensional curve of intensity versus time delay. For IVS data at temperatures above 5 K shown in **Figure 3.8a** and elsewhere, the following wavelength ranges were summed, always using the blue edge of the highest energy exciton — 20 K: 408-422 nm, 78 K: 413-424 nm, 120 K: 414-427 nm, 160 K: 414-429 nm, 200 K: 414-429 nm, and 300 K: 412-433 nm. A 20 ps time window was used to analyze the 5 K and 20 K data, with only a 10 ps window being necessary at 78 K and above due to faster IVS signal dephasing. After summing, the low frequency electronic dynamics were fitted and subtracted off to leave only the vibrational components. The fit was performed in MATLAB using a custom fitting equation. After trying various functional forms, the best fit to the electronic dynamics was found using the sum of 1) the tail of a Gaussian distribution, 2) a triple exponential decay, and 3) a constant offset, a total of 10 fitting parameters. The fit was determined by providing a reasonable initial guess and iteratively optimizing until an optimal stable solution was found.

Next, a Fourier transform was applied to convert the time-domain vibrational data to the frequency domain. A Kaiser-Bessel window function was applied to the time-domain data before the Fourier transform was performed[226], as this has been shown to reduce ringing effects in IVS data[119,128]. By an empirical evaluation, an alpha value of 1.0 was chosen to minimize ringing effects without excessively broadening the peak width. A total of 8000 additional zero-valued data points were appended to the end of the <400 time-domain data points to increase the spectral resolution (zero padding)[119,128]. The Fourier transform was performed using the fft function in MATLAB. The resultant data could be fitted to the sum of multiple Lorentzian peaks as shown in **Figure 3.2d**. A Lorentzian shape was found to provide a better fit than Gaussian and is consistent with homogeneous linewidth broadening mechanisms (see also **Figure 3.12**). It is worth noting that the apparent node between the γ and δ peaks at around 100 $cm^{-1}$ is an effect of performing a Fourier

transform on two decaying sinusoidal waves near to each other in frequency, and we do not believe it to be physically meaningful. However, this effect led us to report all IVS frequencies based on the IVS experimental peak frequency, rather than using the center of the fitted Lorentzian due to difficulties fitting the data in this region. We also note that this analysis process involves summing the data across a wavelength region before Fourier transforming. Alternatively, the data can first be Fourier transformed at each wavelength and then summed, as has been reported by others[128]. This method was also tested and is shown in **Figure 3.11**, but it was found to generate a higher noise level than first summing the raw data due to random fluctuations in individual wavelength pixel intensities.

**Impulsive Vibrational Spectroscopy Time Domain Data Analysis**

The following procedure was used to fit the IVS vibrational data in the time domain. The functional form of the fit we employed is given by **Equation 3.1** in the main text. The fit was performed iteratively, first optimizing for a single decaying sine term, then two terms, and so on. At each iteration, the initial guesses were based on the results of the previous iteration and the strongest peak frequencies identified in the corresponding frequency domain data. This process was continued until the fitting parameters remained constant between successive iterations and four decaying sine terms had been fitted, which all agreed well with the four strongest modes identified in the frequency domain. The fitting results at all temperatures are shown in **Figure 3.18**, and the fitted parameters are listed in **Table 3.5**. At 160 K and 200 K, it was only possible to fit three terms, which is consistent with the frequency domain results in **Figure 3.17**, where the γ peak intensity drops significantly at higher temperatures.

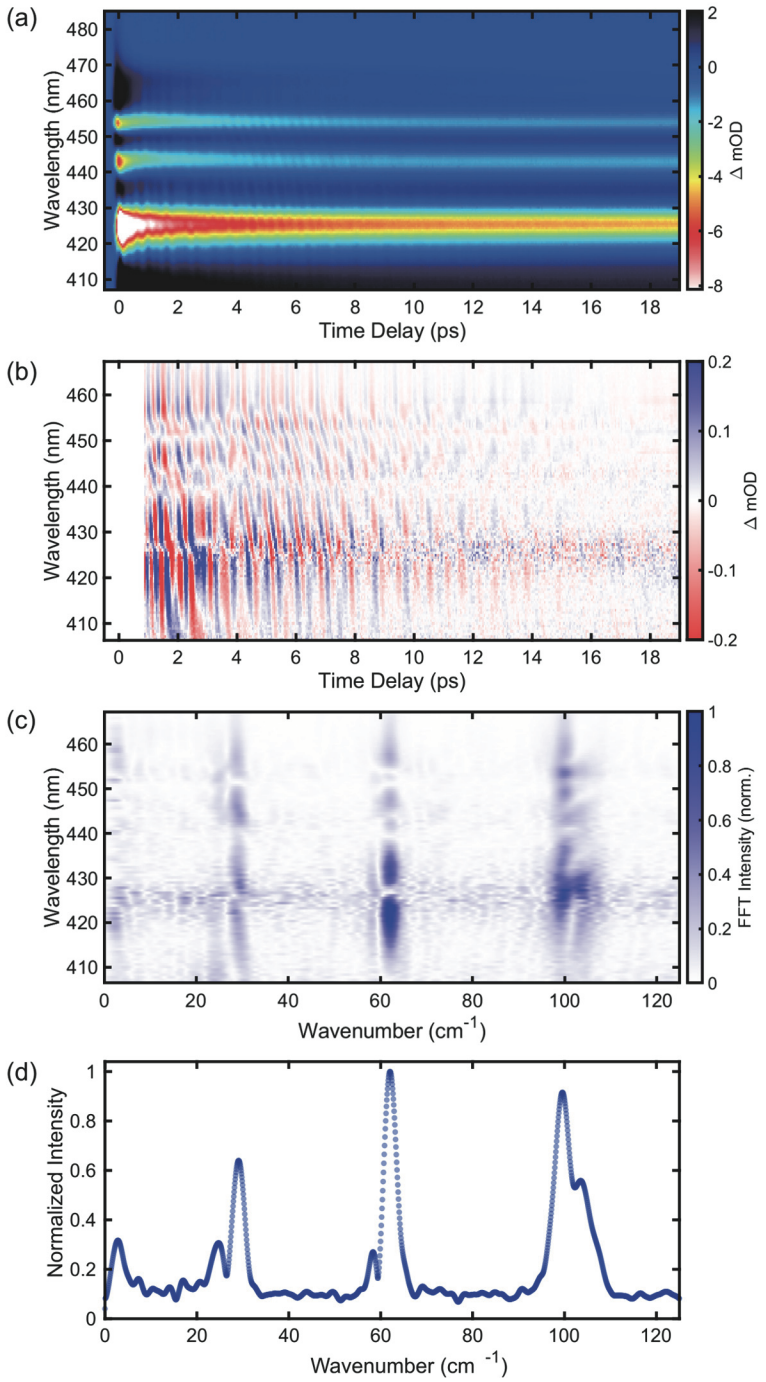


**Figure 3.11. Individual wavelength method of extracting IVS frequency domain data.** (a) IVS color map of AgSePh at 5 K using the same data set as analyzed in Figure 3.2 of the main text. (b) Coherent vibration residual data derived by individually subtracting off the electronic dynamics at each wavelength pixel rather than first summing the data and then performing the electronic dynamics subtraction only once. (c) Results of a Fourier transform to the data in panel (b), again performed at each wavelength pixel. These results show the same vibrational frequencies are present at all wavelengths but with varying intensities. (d) Sum of the 2D data in panel (c) across all wavelengths, resulting in a 1D IVS spectrum comparable to Figure 3.2d.

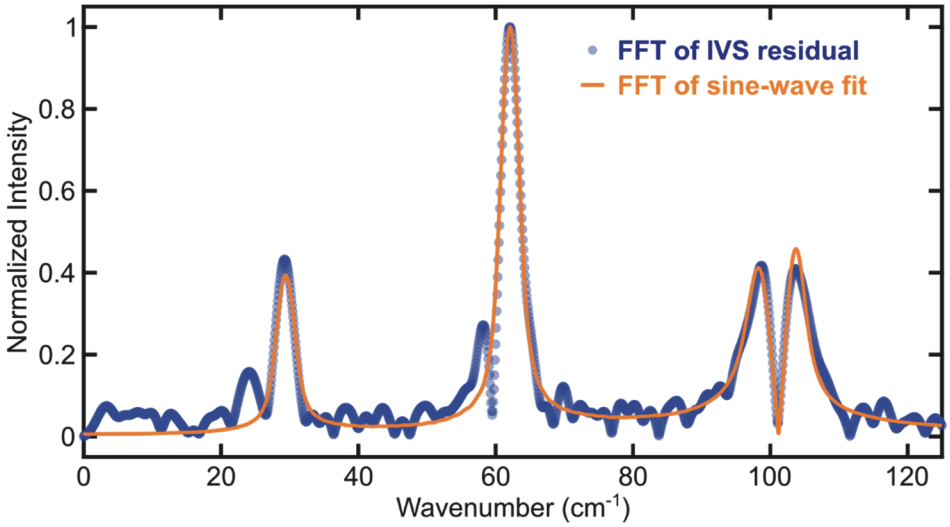


**Figure 3.12. Analysis of linewidth broadening mechanisms in IVS.** (blue) Fourier transform of IVS data at 5 K, identical to Figure 3.2d. (orange) Fourier transform of the sine-wave fit to the IVS data, shown in orange in Figure 3.2c.

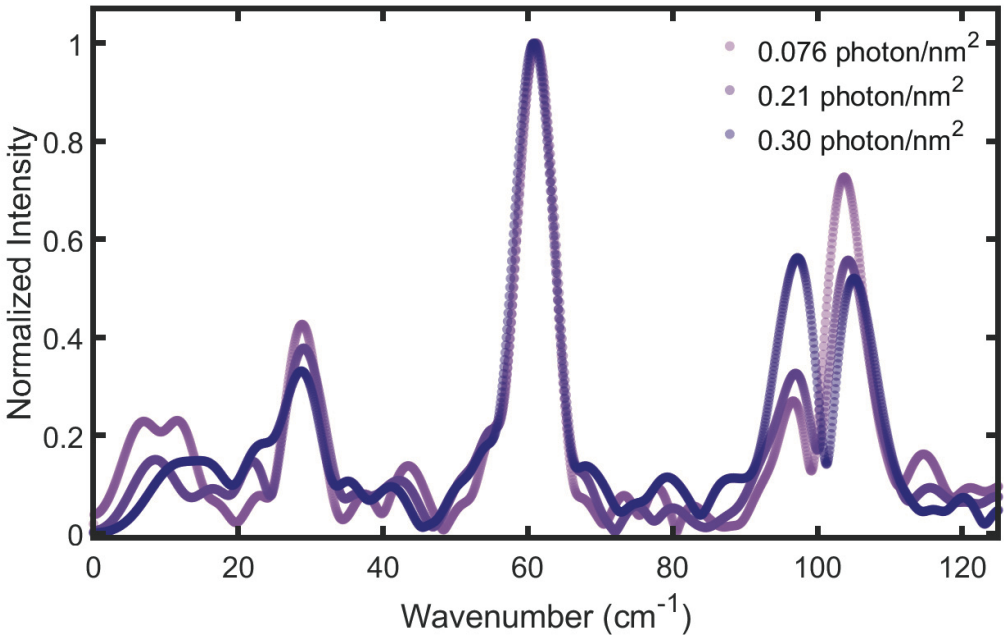


**Figure 3.13. Pump fluence-dependent IVS frequency domain spectra at 78 K.** The same analysis method was used on all three data sets, analyzing the 413-424 nm wavelength region on the blue edge of the highest energy ($X_3$) exciton. The highest fluence value of 0.30 photon/nm$^2$/pulse is the same fluence used to collect all other IVS experimental data presented in the main text, and this curve is the same as the 78 K curve in Figure 3.8d.

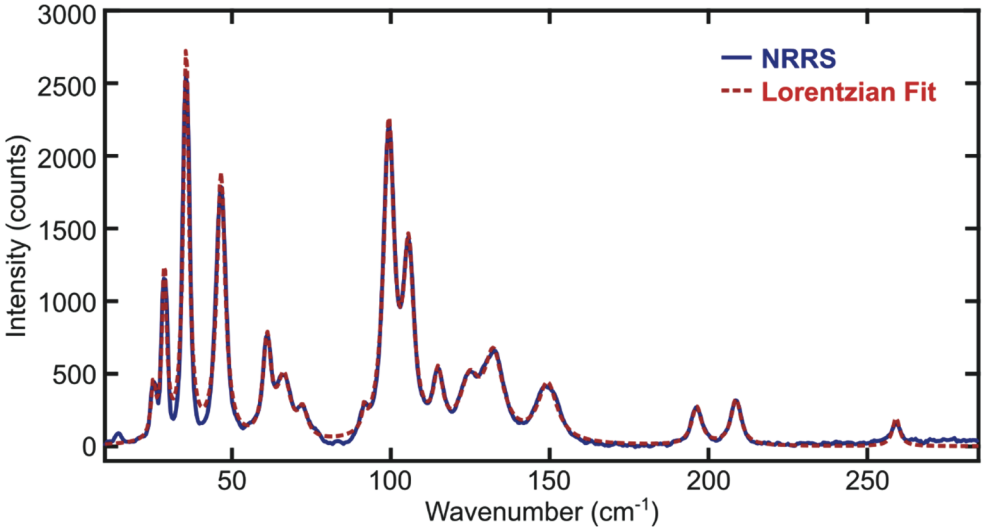


**Figure 3.14. Lorentzian fits to NRRS spectrum at 78 K.** Non-resonant Raman scattering spectrum (NRRS) at 78 K (blue) and the corresponding fit to multiple Lorentzian peaks (red).

## 3.13 Appendix B: Vibrational Mode Data Analysis

### Converting Experimental and Computational Data into Correlation Scores

The DFPT results contain a complete picture of all atomic displacements from equilibrium for each vibrational mode. This information was analyzed by evaluating the relative contributions from different sub-components to the total mode displacement. The categories considered included 1) the total contributions from the silver (Ag), selenium (Se), and phenyl ring (Ph) components, weighted by the amount of spatial displacement and the molecular weight of the component; 2) the changes in bond displacements for several key bonds in the structure, including $(Ag\text{-}Ag)_1$, $(Ag\text{-}Ag)_2$, Ag-Se, Se-C, and C-C; and 3) the degree of displacement for the Ag, Se, and Ph components projected along each of the three Cartesian coordinate directions. Each mode and category was evaluated independently from the others, with the contributions in each category summing to 1. The values for all of the various contributions to each mode are listed in **Table 3.3** and **Table 3.4**.

The correlation scores reported in **Figure 3.5d** were found by calculating the degree to which each characteristic was correlated with IVS activity. For example, to calculate the score of 0.11 for the strongly correlated characteristic of $(Ag\text{-}Ag)_1$ bond displacement, we start with the $(Ag\text{-}Ag)_1$ column of **Table 3.2**. The values of this characteristic for the 5 IVS active modes (α, β, γ, δ, and ζ) are summed:

$$0.45 + 0.30 + 0.41 + 0.39 + 0.35 = 1.90\,. \tag{3.5}$$

This value is divided by the total sum of all 13 modes in the column:

$$\begin{aligned} &0.27 + 0.45 + 0.30 + 0.28 + 0.28 + 0.41 + 0.03 + 0.30 + \cdots \\ &0.39 + 0.35 + 0.19 + 0.31 + 0.31 = 3.87\,, \end{aligned} \tag{3.6}$$

giving a value of

$$\frac{1.90}{3.87} = 0.49\,. \tag{3.7}$$

Finally, the value of a perfectly uncorrelated characteristic is subtracted:

$$0.49 - \frac{5}{13} = 0.49 - 0.38 = 0.11, \tag{3.8}$$

resulting in the reported $(\text{Ag-Ag})_1$ correlation score of 0.11. This methodology gives a maximum correlation score of $1 - 0.38 = 0.62$ and a minimum correlation score of $0 - 0.38 = -0.38$.

**Table 3.2. Summary of experimental and simulation results for all identified vibrational modes in AgSePh.**

| Mode Designation | NRRS at 78 K ($cm^{-1}$) | IVS at 5 K ($cm^{-1}$) | Calculated Raman ($cm^{-1}$) | IVS Lifetime at 5 K (ps) | $(\text{Ag-Ag})_1$ Displacement Contribution | Ag *z* -Motion Contribution |
|---|---|---|---|---|---|---|
| - | 13.8 | - | 19.0 | - | 0.27 | 0.12 |
| Zeta (ζ) | 25.5 | 24.1 | 23.7 | - | 0.45 | 0.28 |
| Alpha (α) | 29.0 | 29.3 | 27.1 | 4.6 | 0.30 | 0.38 |
| - | 35.4 | - | 34.2 | - | 0.28 | 0.33 |
| - | 46.6 | - | 50.8 | - | 0.28 | 0.17 |
| Beta (β) | 61.2 | 62.1 | 62.6 | 4.7 | 0.41 | 0.07 |
| - | 65.9 | - | 68.2 | - | 0.03 | 0.04 |
| Epsilon (ε) | 91.5 | - | 86.3 | - | 0.30 | 0.02 |
| Gamma (γ) | 99.6 | 98.7 | 102.7 | 2.4 | 0.39 | 0.04 |
| Delta (δ) | 105.5 | 103.7 | 110.4 | 3.4 | 0.35 | 0.03 |
| - | 114.8 | - | 114.4 | - | 0.19 | 0.03 |
| - | 125.4 | - | 127.1 | - | 0.31 | 0.01 |
| - | 133.4 | - | 130.4 | - | 0.31 | 0.01 |

**Table 3.3. Simulated atomic displacements and bond length changes for all identified vibrational modes in AgSePh at 5 K.** See also **Figure 3.20**.

| NRRS at 78 K ($cm^{-1}$) | Ag Contribution | Se Contribution | Ph Contribution | $(Ag\text{-}Ag)_1$ Displacement | $(Ag\text{-}Ag)_2$ Displacement | Ag-Se Displacement | Se-C Displacement | C-C Displacement |
|---|---|---|---|---|---|---|---|---|
| 13.8 | 0.54 | 0.20 | 0.26 | 0.27 | 0.41 | 0.07 | 0.07 | 0.18 |
| 25.5 | 0.65 | 0.15 | 0.20 | 0.45 | 0.20 | 0.33 | 0.01 | 0.01 |
| 29.0 | 0.67 | 0.12 | 0.21 | 0.30 | 0.55 | 0.10 | 0.02 | 0.03 |
| 35.4 | 0.56 | 0.13 | 0.30 | 0.28 | 0.52 | 0.08 | 0.03 | 0.09 |
| 46.6 | 0.50 | 0.16 | 0.34 | 0.28 | 0.61 | 0.09 | 0.01 | 0.02 |
| 61.2 | 0.45 | 0.18 | 0.37 | 0.41 | 0.42 | 0.13 | 0.01 | 0.02 |
| 65.9 | 0.36 | 0.19 | 0.44 | 0.03 | 0.48 | 0.41 | 0.02 | 0.07 |
| 91.5 | 0.10 | 0.16 | 0.73 | 0.30 | 0.11 | 0.18 | 0.06 | 0.35 |
| 99.6 | 0.12 | 0.34 | 0.54 | 0.39 | 0.06 | 0.02 | 0.18 | 0.35 |
| 105.5 | 0.13 | 0.32 | 0.55 | 0.35 | 0.42 | 0.15 | 0.01 | 0.07 |
| 114.8 | 0.16 | 0.35 | 0.49 | 0.19 | 0.06 | 0.11 | 0.04 | 0.61 |
| 125.4 | 0.44 | 0.34 | 0.21 | 0.31 | 0.16 | 0.37 | 0.02 | 0.14 |
| 133.4 | 0.47 | 0.32 | 0.21 | 0.31 | 0.15 | 0.42 | 0.04 | 0.07 |

**Table 3.4. Simulated atomic displacements along different Cartesian directions for all identified vibrational modes in AgSePh at 5 K.** See also **Figure 3.20**.

| NRRS at 78 K ($cm^{-1}$) | Ag *x*-Motion | Se *x*-Motion | Ph *x*-Motion | All *x*-Motion | Ag *y*-Motion | Se *y*-Motion | Ph *y*-Motion | All *y*-Motion | Ag *z*-Motion | Se *z*-Motion | Ph *z*-Motion | All *z*-Motion |
|---|---|---|---|---|---|---|---|---|---|---|---|---|
| 13.8 | 0.30 | 0.12 | 0.05 | 0.47 | 0.09 | 0.05 | 0.19 | 0.34 | 0.12 | 0.04 | 0.03 | 0.19 |
| 25.5 | 0.29 | 0.08 | 0.03 | 0.41 | 0.07 | 0.04 | 0.14 | 0.25 | 0.28 | 0.04 | 0.03 | 0.34 |
| 29.0 | 0.22 | 0.05 | 0.04 | 0.30 | 0.07 | 0.04 | 0.15 | 0.26 | 0.38 | 0.03 | 0.02 | 0.44 |
| 35.4 | 0.13 | 0.03 | 0.07 | 0.24 | 0.09 | 0.07 | 0.21 | 0.37 | 0.33 | 0.03 | 0.03 | 0.39 |
| 46.6 | 0.20 | 0.05 | 0.14 | 0.38 | 0.14 | 0.07 | 0.16 | 0.37 | 0.17 | 0.04 | 0.04 | 0.25 |
| 61.2 | 0.14 | 0.09 | 0.16 | 0.40 | 0.24 | 0.03 | 0.12 | 0.38 | 0.07 | 0.07 | 0.07 | 0.22 |
| 65.9 | 0.15 | 0.13 | 0.17 | 0.45 | 0.17 | 0.03 | 0.17 | 0.37 | 0.04 | 0.04 | 0.10 | 0.18 |
| 91.5 | 0.01 | 0.07 | 0.19 | 0.28 | 0.07 | 0.03 | 0.43 | 0.53 | 0.02 | 0.05 | 0.12 | 0.19 |
| 99.6 | 0.04 | 0.09 | 0.19 | 0.32 | 0.04 | 0.20 | 0.19 | 0.43 | 0.04 | 0.05 | 0.16 | 0.25 |
| 105.5 | 0.08 | 0.09 | 0.21 | 0.38 | 0.02 | 0.17 | 0.21 | 0.40 | 0.03 | 0.05 | 0.13 | 0.22 |
| 114.8 | 0.10 | 0.12 | 0.17 | 0.40 | 0.03 | 0.18 | 0.23 | 0.44 | 0.03 | 0.04 | 0.09 | 0.16 |
| 125.4 | 0.02 | 0.20 | 0.08 | 0.30 | 0.42 | 0.08 | 0.07 | 0.57 | 0.01 | 0.06 | 0.07 | 0.13 |
| 133.4 | 0.03 | 0.17 | 0.07 | 0.27 | 0.43 | 0.11 | 0.08 | 0.61 | 0.01 | 0.05 | 0.06 | 0.12 |

## 3.14 Appendix C: Additional Temperature-Dependent IVS Figures

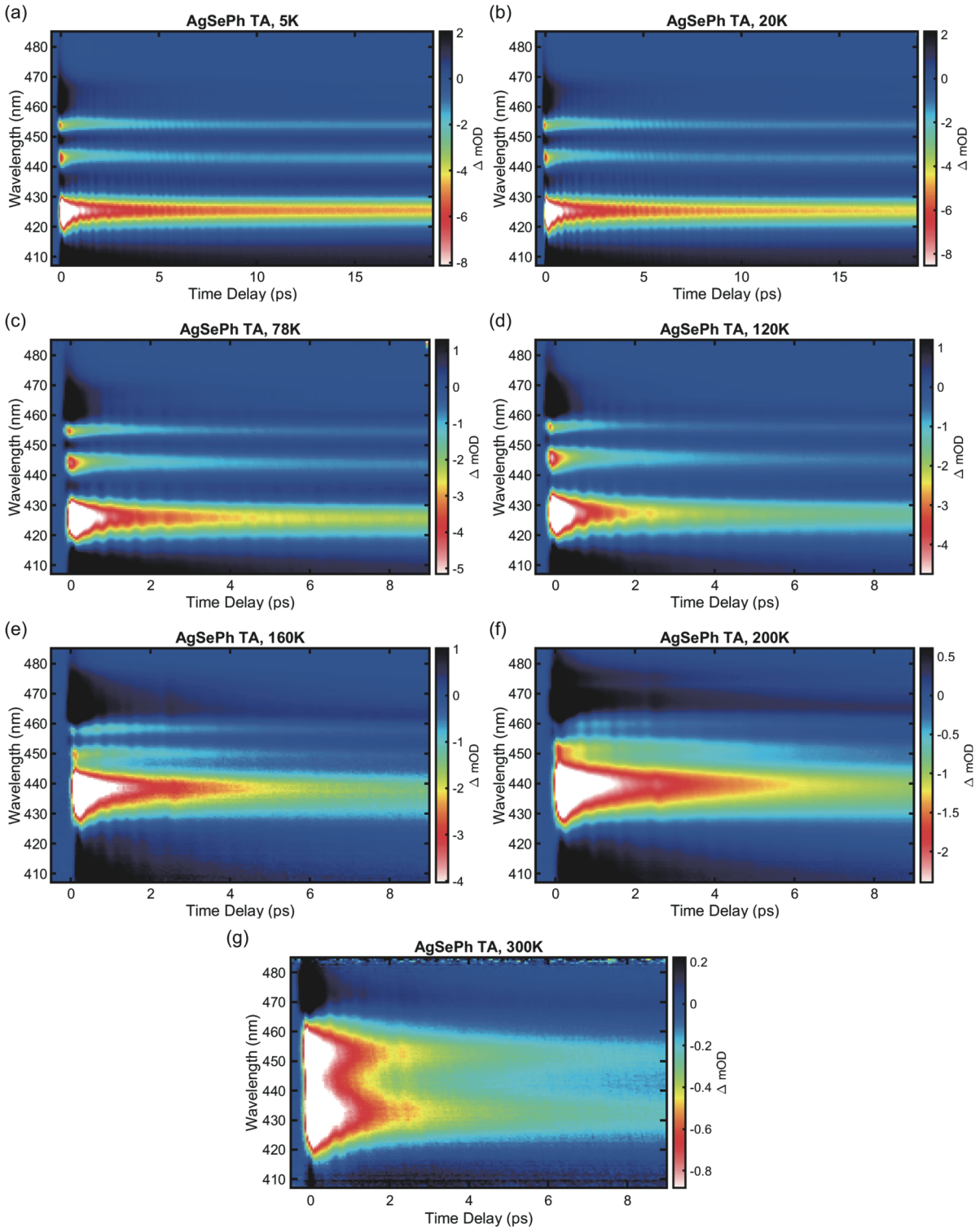


**Figure 3.15. IVS color maps of AgSePh measured at temperatures from 5 K to 300 K.**

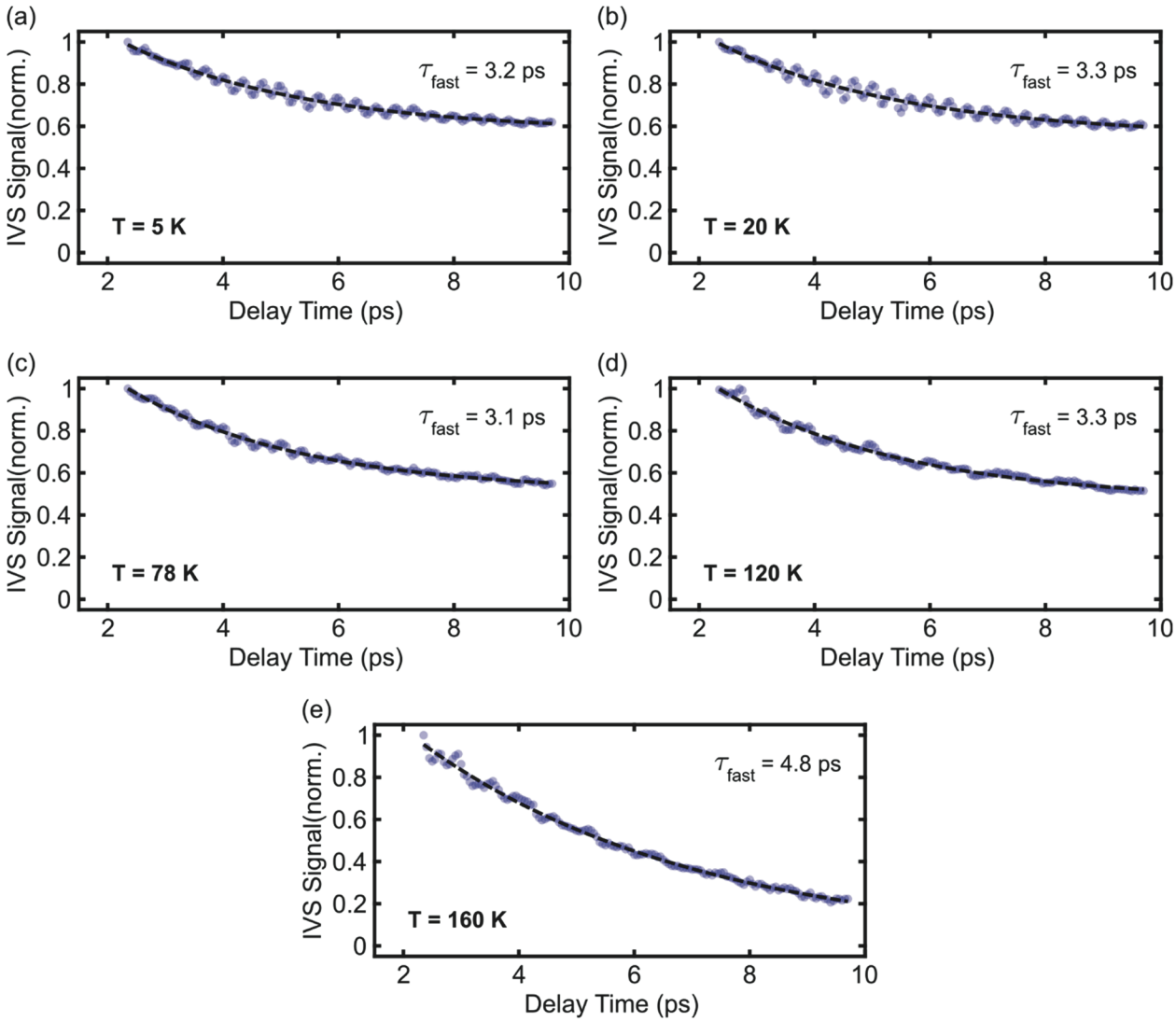


**Figure 3.16. Electronic decay dynamics of the $X_1$ bleach feature in AgSePh at temperatures from 5 K to 160 K.** The data was well fit with a biexponential decay, with the slow decay lifetime set to 1 μs. The fast lifetime is always found to be ~3-5 ps and doesn't show a clear trend with temperature, although the relative contribution of the fast lifetime component increases with increasing temperature. The small step in the data around 3 ps seen in some scans is due to a double reflection of the pump beam slightly re-exciting the sample. Data above 160 K was excluded due to increasing spectral overlap of the $X_1$ and $X_2$ bleach features.

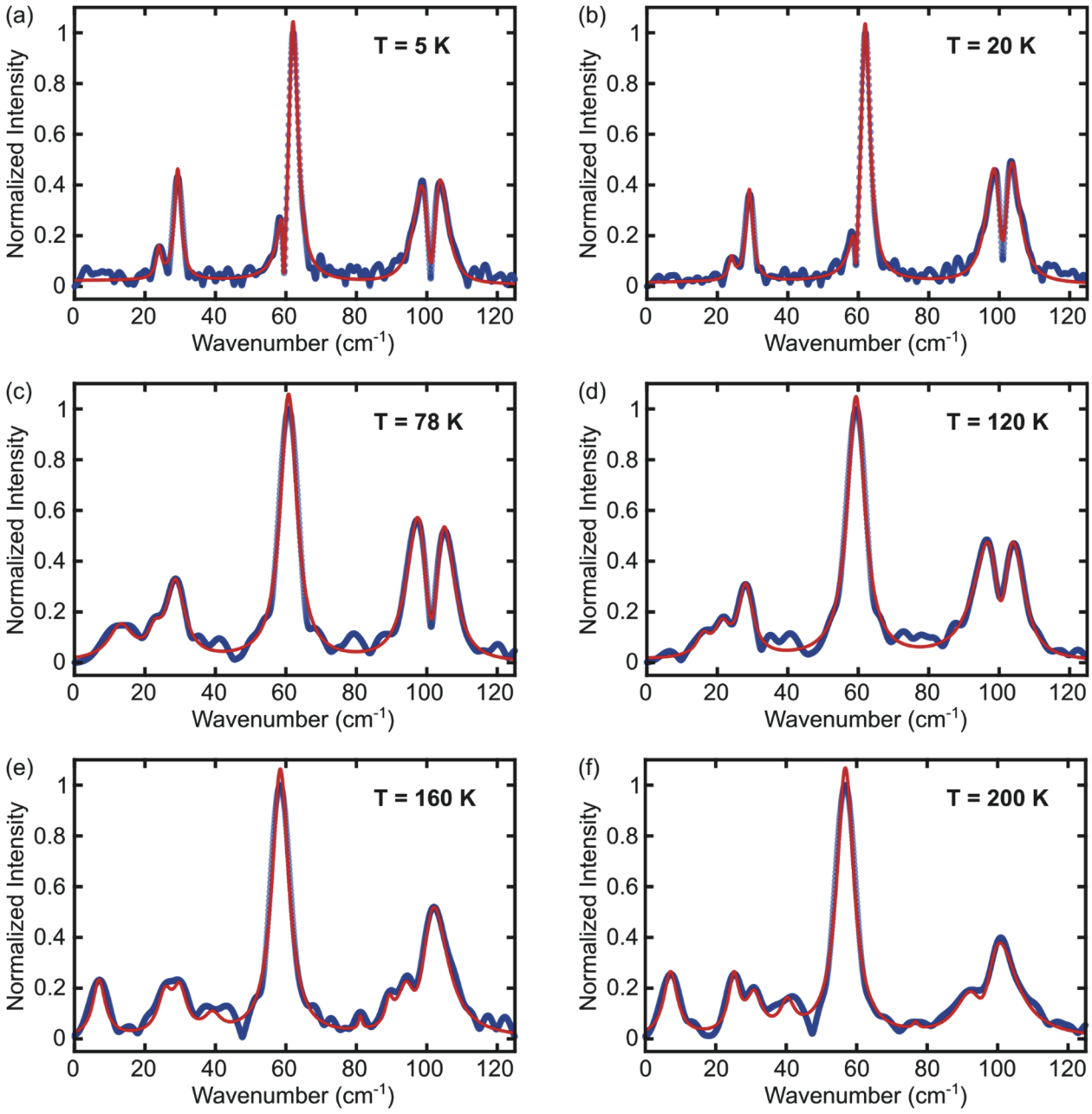


**Figure 3.17. Temperature dependence of the IVS spectrum from 5 K to 200 K.** These curves are equivalent to the data shown in Figure 3.8d, but separated and normalized at each temperature. The raw data is shown in blue, with a fit to the sum of multiple Lorentzian peaks in red.

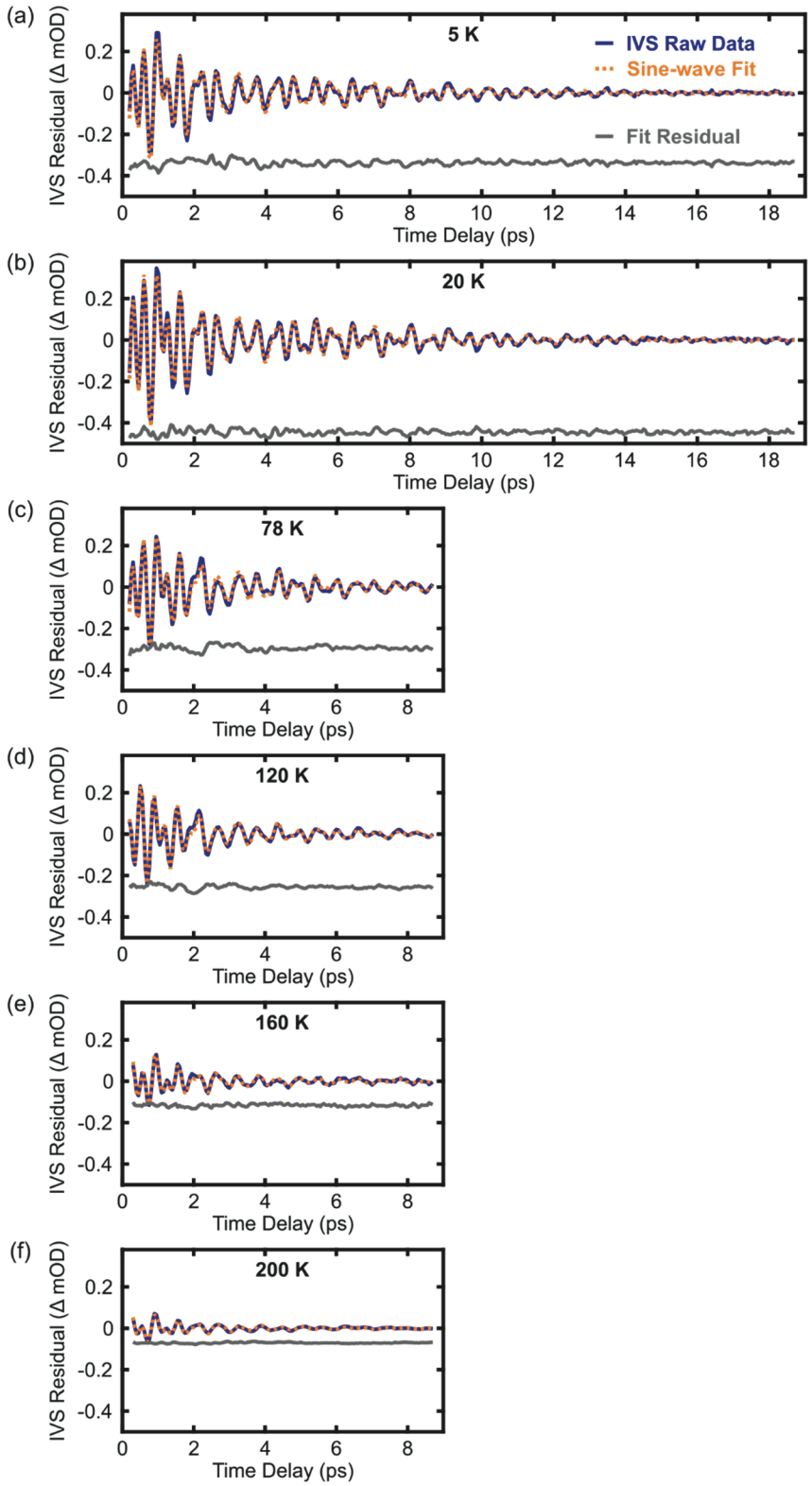


**Figure 3.18. Temperature-dependent IVS residuals with sine wave fits from 5 K to 200 K.** The raw data in blue is equivalent to that shown in Figure 3.8a. The orange curve represents the sine wave fit, with the extracted fit parameters shown in Table 3.5. The fit residual in gray is the difference between the experimental data and fit, offset for clarity.

**Table 3.5. Extracted parameters from time domain fits at all temperatures.**

| Designation | Parameter (units) | 5 K | 20 K | 78 K | 120 K | 160 K | 200 K |
|---|---|---|---|---|---|---|---|
| Alpha (α) | Frequency ($cm^{-1}$) | 29.4 | 29.4 | 29.0 | 27.8 | 27.0 | 26.4 |
| | Lifetime (ps)[a] | 4.6 | 5.2 | 4.9 | 4.2 | ∞ | ∞ |
| | Intensity (ΔmOD) | 0.7 | 0.6 | 0.5 | 0.4 | 0.1 | 0.0 |
| | Phase (deg) | 69 | 67 | 104 | 193 | 360 | 51 |
| Beta (β) | Frequency ($cm^{-1}$) | 62.1 | 62.0 | 60.6 | 59.4 | 58.7 | 56.9 |
| | Lifetime (ps) | 4.7 | 4.8 | 3.8 | 3.1 | 3.1 | 2.7 |
| | Intensity (ΔmOD) | 1.8 | 2.1 | 1.7 | 1.6 | 0.9 | 0.6 |
| | Phase (deg) | 213 | 208 | 236 | 298 | 327 | 6 |
| Gamma (γ) | Frequency ($cm^{-1}$) | 98.7 | 99.1 | 97.8 | 96.7 | - | - |
| | Lifetime (ps) | 2.5 | 2.8 | 1.9 | 1.3 | - | - |
| | Intensity (ΔmOD) | 2.2 | 2.6 | 2.5 | 3.1 | - | - |
| | Phase (deg) | 165 | 141 | 196 | 125 | - | - |
| Delta (δ) | Frequency ($cm^{-1}$) | 103.4 | 103.1 | 104.5 | 104.2 | 101.4 | 100.1 |
| | Lifetime (ps) | 3.4 | 3.0 | 2.8 | 2.2 | 1.2 | 1.0 |
| | Intensity (ΔmOD) | 1.3 | 2.6 | 1.2 | 1.0 | 2.6 | 1.5 |
| | Phase (deg) | 138 | 144 | 110 | 191 | 347 | 28 |

[a]*At 160 K and 200 K, the optimal fit to the time domain data exhibited no decay in the alpha mode over 10 ps, leading to the infinite decay lifetimes reported here.*

## 3.15 Appendix D: DFT Computation Discussion and Figures

### Sources of Error in DFT Calculations

A possible source of calculation error is the exchange correlation (XC) approximation. In this work, we used the PBE XC approximation, which provides a good trade-off between accuracy and computational cost. More advanced functionals, such as hybrids, could provide more accurate results, but at a prohibitively expensive computational cost for such a large electronic system. An additional complication is that the relatively complex crystal structure of the material, and the resultant large number of degrees of freedom, give rise to a "busy" theoretical spectrum with many modes of similar frequencies and intensities.

Some of the most noticeable differences between the experimental and calculated spectra can be found in the 150-350 $cm^{-1}$ frequency range. While the experimental non-resonant Raman spectrum shows some small peaks around 200 $cm^{-1}$ and 260 $cm^{-1}$, this is clearly quite different from the three high intensity split peaks that appear in the calculated spectra at approximately 180 $cm^{-1}$, 230 $cm^{-1}$, and 290 $cm^{-1}$ (**Figure 3.19**). When we examine, the atom-projected spectra, we observe that only the Se and Ph components of the system contribute appreciably to these peaks. This indicates that vibrational motion of the Se and Ph components of the AgSePh system are suppressed in the experimental case relative to the theoretical case. Calculation error from the XC approximation's treatment of the $\pi - \pi$ between the phenyl groups could be one source of error[227], but there may also be a physical explanation for the suppression of these modes in the real system such as interactions between adjacent phenyl rings. Both the monolayer and bulk 2D AgSePh systems were found to have very similar spectra, and thus we conclude that inter-layer interactions are not responsible for suppressing these phenyl vibrations.

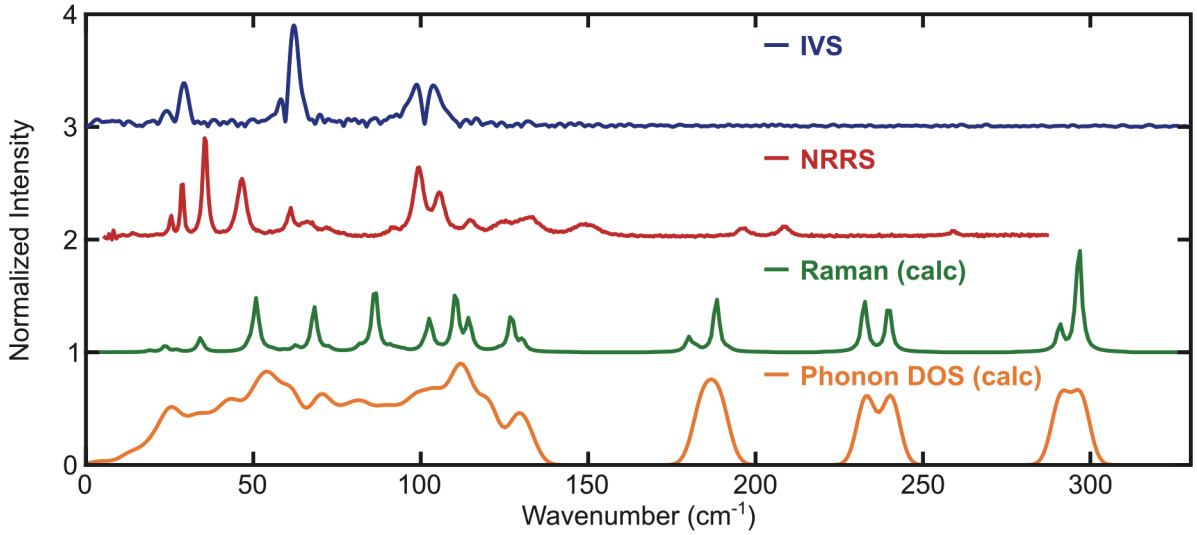


**Figure 3.19. Comparison between computational and experimental results over 0-350 $cm^{-1}$ frequency range.** The curves correspond to the same data shown in Figure 3.5a but are extended out to 350 $cm^{-1}$ to show higher frequency modes found in NRRS and computational results.

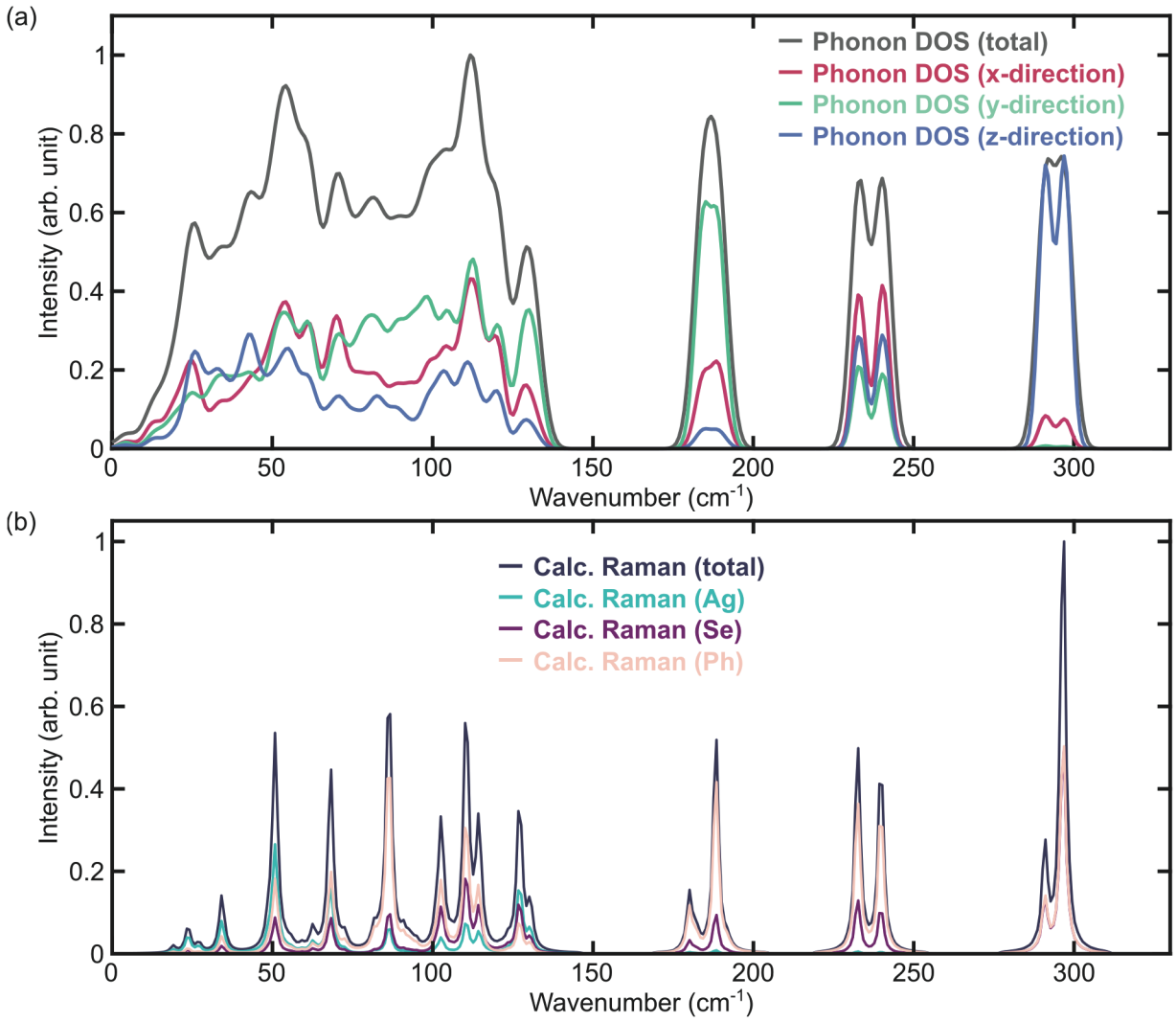


**Figure 3.20. Contributions from various vibrational mode characteristics to calculated Raman spectrum and phonon density of states.**

# Chapter 4
# Temperature-Dependent Neutralization Dynamics in Charged $CsPbBr_3$ Perovskite Nanocrystals

> *Perovskites have been a life-changing experience… The pace of research, the pace of scientific and technological advancement with these materials is like science on steroids.*
>
> Henry Snaith, Professor at the University of Oxford and co-founder of Oxford PV[228]

*The basis of this chapter has been adapted from:*
Eric R. Powers, Wenbi Shcherbakov-Wu, Franziska Krieg, Maksym V. Kovalenko, William A. Tisdale. "Temperature-Dependent Neutralization Dynamics in Charged $CsPbBr_3$ Perovskite Nanocrystals." *In Preparation* (2023).

## 4.1 Abstract

Colloidal semiconductor nanocrystals (NCs), or quantum dots, have attracted significant interest over the last few decades due to their solution processability, narrow bandwidth emission, and tunable optical properties. Recently, new methods for synthesizing monodisperse lead halide perovskite NCs have been developed, enabling the union of colloidal nanocrystals with the superior optoelectronic properties of perovskites. A long-identified but still unresolved challenge in both traditional and perovskite NCs is fluorescence intermittency, or blinking, which lowers NC quantum efficiency and impairs device performance. Blinking is generally believed to be caused by NC charging and neutralization processes, although there remains broad disagreement about the underlying mechanisms that drive this phenomenon. Herein, we employ temperature-dependent transient absorption spectroscopy to study charging and neutralization in $CsPbBr_3$ perovskite nanocrystals. We identify significant nanocrystal photocharging at cryogenic temperatures, with the charge-separated state persisting on microsecond timescales. We then model the transient absorption data to extract the charged NC spectrum and a ~100 meV energy barrier to charged NC neutralization. Furthermore, a sub-linear fluence dependence of charging

rates excludes an Auger-driven charging process, in direct contrast with some previously established NC charging mechanisms. These results help illuminate of the mechanism of charging in $CsPbBr_3$ NCs and inform future efforts to synthesize blinking and charging-free nanocrystals.

## 4.2 Introduction

Colloidal semiconductor nanocrystals (NCs) or quantum dots (QDs) are a family of nanomaterials that exhibit exceptional optoelectronic properties including bandgap tunability[29,30,229,230], narrow bandwidth emission[26,36], and high quantum efficiency[231,232]. They are normally spherical or cuboidal inorganic crystals <20 nm in length, coated in aliphatic capping ligands, and produced using solution-based syntheses[6,8,19]. Since their initial development in the last two decades of the 20$^{th}$ century[31,32], continued advances in NC technology have led to the commercialization of this material platform in television displays[40], with ongoing progress towards implementation in lighting[233–236], photovoltaic[4,237,238], lasing[10–12], quantum information[16,18,239], and other applications. Traditional NCs are most commonly comprised of metal and chalcogenide elements in binary pairs or alloys (e.g. CdSe, PbS, $Zn_xCd_{1-x}S$)[8] and are often grown as layered core-shell structures to improve surface passivation[36,231].

More recently, lead halide perovskite nanocrystals[24,240] (e.g. $CsPbBr_3$) have been developed that demonstrate many of the same beneficial characteristics as their traditional NC counterparts. Additionally, perovskite NCs incorporate many of the unique attributes of lead halide perovskites, most notably defect tolerance[72,74,241] and a high absorption coefficient[2,71]. Perovskite NCs are more robust to non-radiative recombination processes than traditional NCs, with reports of high quantum efficiencies approaching 90% even in core-only structures[24,239,242,243]. Thanks to the combination of these properties, perovskite NCs have great potential for use in LEDs[6,234–236] and as quantum emitters[16,239,244].

A major challenge for both traditional and perovskite NCs is fluorescence intermittency, or blinking, which can reduce radiative efficiency and represents a major impediment to device applications. Blinking, characterized by temporal switching between states of differing brightness and quantum yield, has been widely reported in traditional NCs[245–250]. In perovskite NCs, some studies have shown reduced blinking compared to traditional NC systems[239,242,251], but the issue remains unresolved[244,252,253]. Blinking is most commonly attributed to nanocrystal charging and

neutralization, with bright "on" state emission coming from a neutral NC, while the dimmer "off" state is associated with a charged NC containing an extra electron or hole. This scheme is supported by reports of shorter radiative lifetimes of the "off" state due to Auger recombination of the charged exciton (trion) state[245,246,254,255], as well as observations of delayed fluorescence resulting from neutralization of the charge-separated state, which often follows a power law distribution[247,249,252]. The physical mechanism(s) causing charging in NCs are still subject to debate. Most commonly, charging is thought to result from charge carrier trapping at sites on the NC surface, at the core-shell interface, or external to the NC, such as on the capping ligands[249,254–259]. Many different models have been proposed that describe the dynamics and energetics of trapping and detrapping processes in order to explain experimental observations[245,246,248–250,252,254,257,260,261], making it clear a universal model is unlikely to fully describe charging and blinking in all materials systems under all conditions.

In this work, we employ transient absorption (TA) spectroscopy to analyze charging and neutralization dynamics in weakly confined $CsPbBr_3$ NCs. We find a long-lived TA signal showing microsecond persistence at cryogenic temperatures, which we conclude is the result of NC charging. We then perform temperature-dependent TA and use the results to develop a model describing charging and neutralization processes in this system. This unique data set allows us to study the effects of temperature on charging and neutralization processes and improve mechanistic understanding of photocharging in perovskite nanocrystals.

### 4.3 Synthesis and Basic Characterization of $CsPbBr_3$ Nanocrystals

The colloidal $CsPbBr_3$ perovskite nanocrystals (NCs) used in this study were synthesized with zwitterionic capping ligands (3-(N,N-dimethyloctadecylammonio)propanesulfonate) reported to improve surface binding and NC stability[67]. The synthesis and linear absorption studies of these particular samples were also reported previously[262]. The NCs used here have an average edge length of 8.1 ± 0.75 nm as measured with transmission electron microscopy (TEM) (**Figure 4.1a, inset**). This size is slightly larger than the 7 nm exciton Bohr diameter in $CsPbBr_3$[24], leading to weakly confined NCs. The solution-phase absorption and photoluminescence spectra of the NCs are shown in **Figure 4.1a**, with the absorption spectrum showing a clear band edge excitonic peak at a wavelength of 504 nm as well as an additional higher energy excitonic feature at ~480-485

nm. After synthesis, the NCs were embedded in polystyrene in a dilute concentration, such that each NC can be considered isolated and independent of neighboring NCs. The use of a polymer film, rather than a dilute colloidal solution as is more commonly done, enables us to perform low temperature studies without concern for the effects of solvent freezing. The NC-embedded polymer films were kept air-free during synthesis, storage, and experimentation.

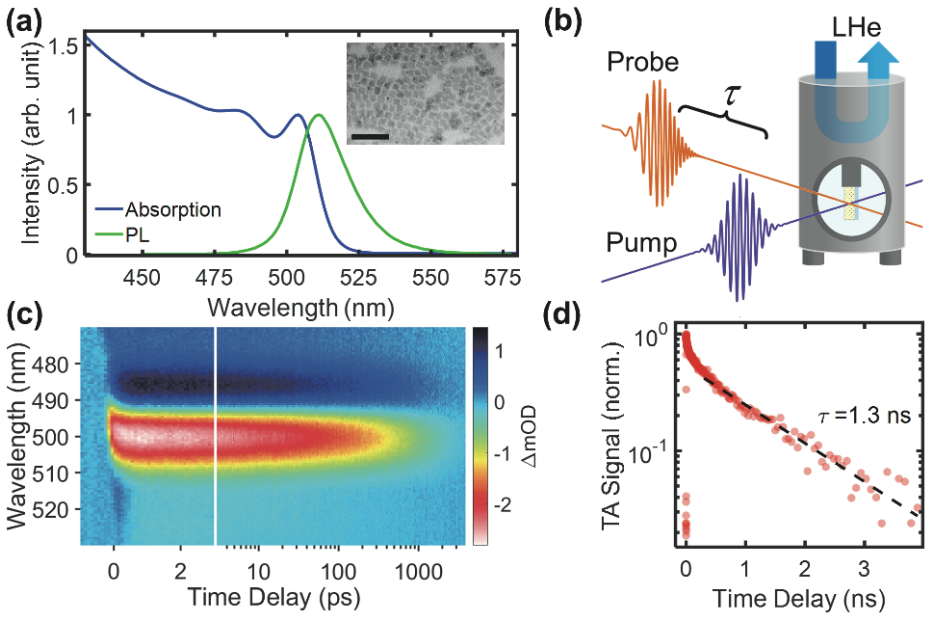


**Figure 4.1. Room temperature spectroscopy of $CsPbBr_3$ nanocrystals.** (a) Absorption and photoluminescence spectra of $CsPbBr_3$ NC –embedded polymer film. Inset: Transmission electron micrograph (TEM) of NCs in a densely packed thin film. Scale bar is 50 nm. (b) Schematic of TA spectroscopy, showing the sequential interaction of ultrafast pump and probe pulses with the sample at a time delay $\tau$. The film sample is mounted in a vacuum cryostat and can be cooled with liquid helium or nitrogen. (c) TA colormap of $CsPbBr_3$ NCs at room temperature (300 K) and low fluence (<N> = 0.4). The first 3 ps are plotted on a linear time scale and include carrier cooling to the band edge. The remainder of the time window is plotted on a logarithmic scale and shows no significant spectral shifts. (d) Decay dynamics of the ground state bleach peak in panel (c), showing a single exponential decay fit over a 300-3900 ps time window with a 1.3 ns fitted lifetime.

### 4.4 Room Temperature Transient Absorption Spectroscopy

The primary experimental method we employ to investigate the electronic dynamics of $CsPbBr_3$ NCs is transient absorption (TA) spectroscopy. This ultrafast technique utilizes a narrowband laser pulse (centered at 450 nm in our experiments) to excite the sample, followed by a broadband probe pulse to measure the change in absorption as a function of a variable time delay,

as schematically illustrated in **Figure 4.1b**. TA provides a wealth of information about the excited state electronic structure and dynamics in a material. Details about the experimental setup are provided in the Methods section. To study the excitonic dynamics of $CsPbBr_3$ nanocrystals, we first collected a TA spectrum of the NC-embedded polymer film at room temperature (300 K). In **Figure 4.1c**, we show a room temperature TA colormap over a 0-4 ns time delay window. This and all other TA data are performed in the low-fluence regime, with an average excitation density (<N>) of 0.3-0.4 excitons per nanocrystal unless otherwise noted. The primary feature visible is a ground state bleach (GSB) signal centered at 501 nm. This represents a reduction in absorption by the NC film compared to the ground state, due to the prior interaction with the pump pulse reducing the number of valence band to conduction band electronic transitions available[123]. Slightly above the bandgap at 488 nm, an induced absorption (IA) feature representing an increase in absorption can be seen, resulting from newly available absorption transitions after excitation. These features form in ~1 ps after time zero, consistent with the ~100 fs pump pulse duration followed by hot carrier cooling from the slightly above bandgap excitation. A trend of the formation and subsequent decay of the GSB peak at room temperature is shown in **Figure 4.1d**. A faster initial decay is seen for the first few hundred picoseconds, likely the result of recombination of the few biexcitons formed out of the Poisson distribution of excited NCs. For excitation densities up to <N> = 0.4, we find that these multiexciton dynamics are completed after 300 ps, as shown by the normalized fluence series in **Figure 4.2**. Thus, the decay trace in **Figure 4.1d** can be fitted to a single exponential decay after 300 ps, yielding a lifetime of 1.3 ns.

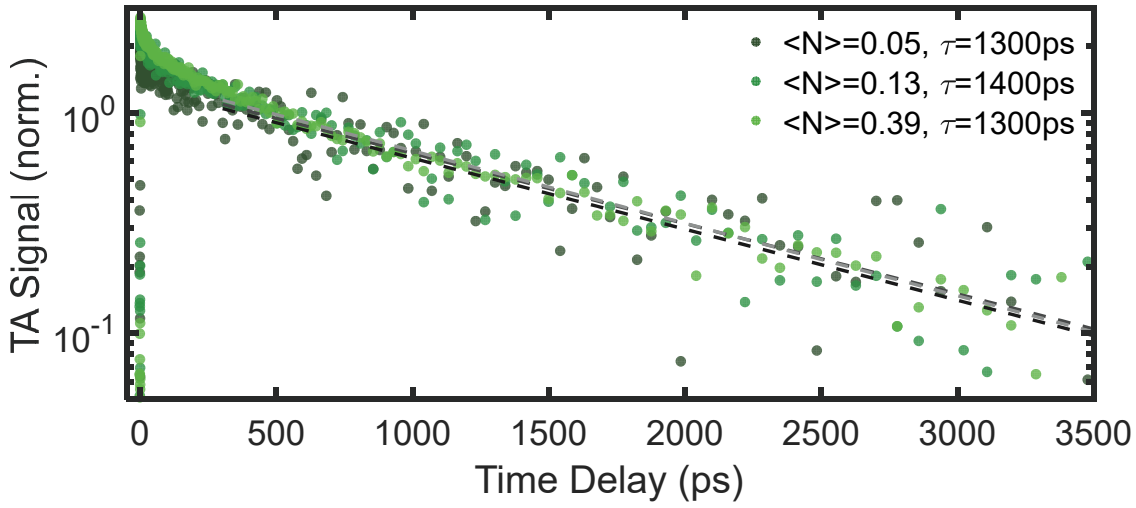


**Figure 4.2. Low-fluence excitation regime comparison.** Ground state bleach decay dynamics of room temperature $CsPbBr_3$ NCs at excitation densities of <N> = 0.05, 0.13, and 0.39. The curves show identical decay dynamics after 300 ps, with a single exponential fit yielding lifetimes of 1.3 ns, 1.4 ns, and 1.3 ns, respectively.

We can also generate a series of spectral slices at increasing time delays in order to study the development of the electronic excited state over time. In **Figure 4.3a**, we show these spectra for the same 300 K data set. No change in spectral lineshape is evident, a finding reinforced when viewing the curves normalized by the GSB peak intensity as shown in **Figure 4.3d**. The normalized data show no shifts in the GSB or IA peak intensity, wavelength, or spectral shape with time delay. These room temperature TA dynamics are consistent with the formation and subsequent decay of neutral excitons in the NCs in the low fluence regime. The 1.3 ns exponential decay lifetime is the result of radiative and nonradiative decay of excitons, in agreement with other reports of $CsPbBr_3$ perovskite NC exciton lifetimes at room temperature[67,263,264]. The spectral shape and decay dynamics are also consistent with our previous study of similarly-sized, zwitterionic ligand-coated $CsPbBr_3$ NCs in solution[159].

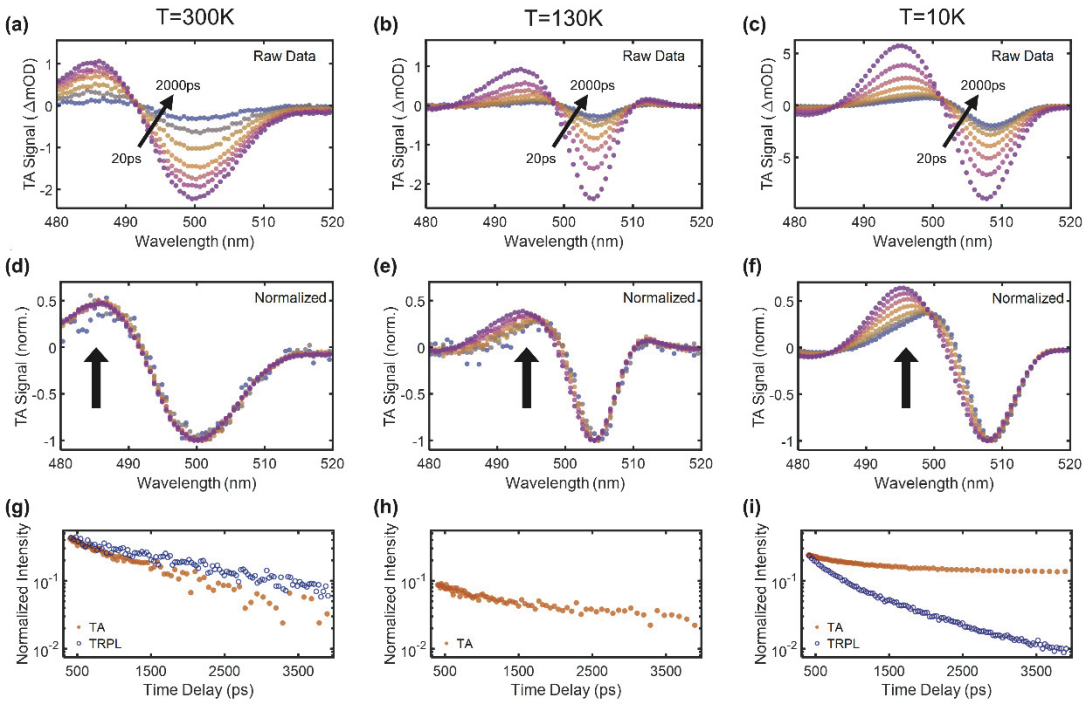


**Figure 4.3. Temperature-dependent spectral and temporal dynamics in $CsPbBr_3$ NCs.** (a)-(c) TA spectral slices over the first 2 ns at temperatures of 300 K, 130 K, and 10 K, respectively. The displayed curves were measured at time points of 20, 50, 100, 200, 500, 1000, and 2000 ps. (d)-(f) Normalized TA spectral slices for the same time and temperature windows as in panels (a)-(c). The arrows highlight the IA feature that appears time-invariant at 300 K but changes in lineshape and peak frequency at lower temperatures. (g)-(i) Decay traces of the GSB TA signal (orange dots) and time resolved photoluminescence (TRPL) signal (blue circles) over a 400-3900 ps time window at temperatures of 300 K, 130 K, and 10 K (5 K for TRPL). The TA intensity is normalized to 1 at time zero, and the TRPL intensity is normalized to the TA intensity at 400 ps. There is no TRPL data at 130 K.

## 4.5 Temperature-Dependent Transient Absorption Spectroscopy

Next, we look to investigate the impact of temperature on excitonic dynamics in $CsPbBr_3$ NCs, which can help to reveal thermodynamic and kinetic effects. We collected the transient absorption spectrum of the sample at temperatures ranging from 10 K to 300 K, with data collected every ~30 K. First considering the spectral dynamics, we can contrast the time slices evaluated previously at room temperature with those in the intermediate and low temperature regimes (**Figures 4.3a, 4.3b, and 4.3c** at temperatures of 300 K, 130 K, and 10 K, respectively). As the temperature is reduced, the decay dynamics of the TA signal change, as illustrated by the spacing between successive time slices. In addition, there is an apparent spectral shift of the GSB and IA peaks to lower energies with increasing time delay. These spectral changes are more apparent in

the normalized curves shown in **Figures 4.3d, 4.3e,** and **4.3f**, which also clearly reveal a change in relative intensity and shape of the IA feature as well as a narrowing of the GSB peak over time.

The most surprising phenomenon we observe is an apparent transition from a single time-independent lineshape at room temperature (**Figure 4.3d**) to a dynamically changing lineshape at cryogenic temperatures (**Figure 4.3f**), despite maintaining photoexcitation in the low fluence regime. The transition between these two regimes is found to occur around 100-200 K, as exemplified by the intermediate temperature regime data **Figure 4.3e** collected at 130 K (TA curves at all collected temperatures are shown in **Figure 4.8** and **Figure 4.9**). The dynamically changing spectrum at low temperatures could result from multiple species with different TA spectra decaying at different rates, or it could point to more complex dynamics, such as multiple populations interacting with non-equilibrium kinetics.

A study of the ground state bleach peak temporal decay as a function of temperature complements the spectral analysis. In **Figures 4.3g, 4.3h,** and **4.3i**, the TA bleach peak intensity over time is plotted, again at 300 K, 130 K, and 10 K, respectively. The room temperature results in **Figure 4.3g** show a single exponential decay, evidenced by the linear trend on a semi-log plot. The figure also includes time-resolved photoluminescence data (TRPL) taken on the same sample at 300 K, showing good agreement with the TA results. As temperature is reduced (**Figures 4.3h** and **4.3i**), the TA dynamics become increasingly non-exponential, with a faster initial decay (consistent with the faster exciton lifetime seen at lower temperatures in $CsPbBr_3$ NCs[243,265]) followed by an anomalous leveling off at a significant fraction of the initial value. This long-lived state corresponds to the redshifted spectrum we saw in the spectral analysis at the longest time delays in **Figures 4.3e** and **4.3f**. The 10 K TRPL curve in **Figure 4.3i** diverges significantly from the corresponding TA data (as we would expect from a non-exponential decay shape), showing an order of magnitude weaker signal by the end of the time window,. TRPL measures the rate of radiative recombination, which is low if the lifetime is long, while TA is a continuous measure of the excited state population. These data show that at low temperature, the TA signal appears to come predominantly from the exciton state initially, but also reveals an unidentified long-lived state after the exciton has decayed.

## 4.6 Repetition Time Transient Absorption Spectroscopy

In order to get a glimpse into the TA signal intensity at much longer time delays than can be sampled with our mechanical delay stage (up to 4 ns), we also employ repetition time transient absorption. This is done by collecting the TA signal at a negative time delay, where the pump arrives just *after* the probe. In this way, the time delay between the pump pulse and the next probe pulse is effectively the repetition time of the laser, or the reciprocal of the repetition rate[264]. In most circumstances, the repetition time of the laser is much longer than the longest-lived species excited by the laser pulse and this "negative time delay" signal isn't present. However, we are able to use this technique to detect the long-lived species at low temperatures, greatly expanding our time window of investigation and allowing us to better characterize the system.

**Figure 4.4a** shows a split panel colormap of the $CsPbBr_3$ NC TA signal at 300 K. The left panel gives the first 40 picoseconds of data, showing the GSB and IA signal intensity soon after photoexcitation. The middle panel shows the long time delay region of the normal TA detection setup, around 3-4 ns. The color scale has been magnified by 5x to allow us to see the faint TA signal remaining at this time delay. The right panel shows the repetition time data at 5 μs, also with 5x color scale enhancement, revealing no measureable TA signal. We can contrast these findings with **Figure 4.4b**, showing the same time windows and color scale magnifications but at a temperature of 10 K. The TA signal in the middle panel of **Figure 4.4b** is much stronger and nearly constant from 3 ns to 4 ns, consistent with low temperature dynamics shown in **Figure 4.3i**. The right panel of **Figure 4.4b** is most interesting, clearly showing a TA signal 5 μs after excitation by the pump pulse. We can confirm this is a TA signal and not just spontaneous photoluminescence reaching the detector because of the presence of an induced absorption signal, whereas spontaneous PL would only ever create a bleach signal.

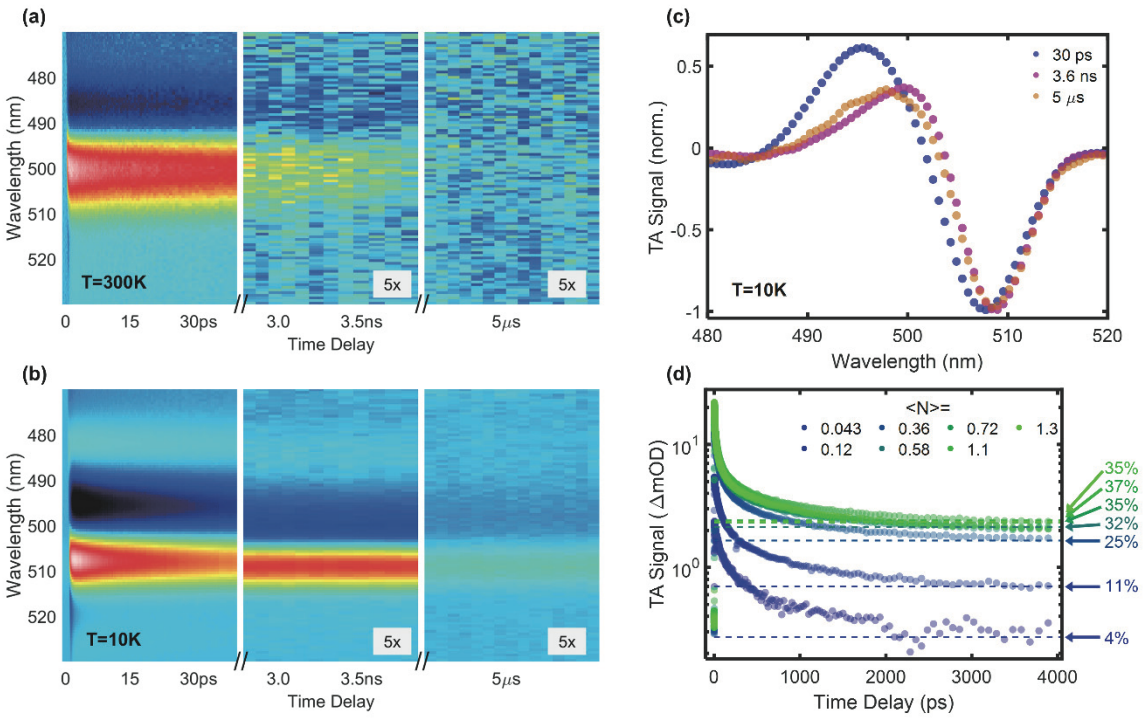


**Figure 4.4. Repetition time and fluence-dependent TA spectroscopy.** (a) Split panel colormap of 300 K TA data, showing early time dynamics from 0-40 ps (left), intermediate time dynamics of 3-4 ns (center), and late time dynamics at the repetition time of 5 μs (right). The 5x designations in the center and right panels denote the color scale has been scaled by that factor to better display the weaker TA signal at longer time delays. (b) Split panel colormap of 10 K TA data with the same time windows as in panel (a), showing increased TA signal intensity at intermediate and long time delays. (c) Normalized TA spectral slices at 10 K at time delays of 30 ps, 3.6 ns, and 5 μs. (d) Fluence-dependent TA curves showing the GSB decay at 10 K for various excitation densities (circles). The dotted lines represent the percentage of NCs excited with one exciton according to a Poisson distribution, as denoted to the right of the figure.

In **Figure 4.4c**, we plot the 10 K TA data from **Figure 4.4b** as three separate spectral slices to better compare the spectral shape at different time delays. We find that the lineshape of the 5 μs curve is nearly identical to that of the 3.6 ns curve, confirming the TA signals from both result from the same long-lived species and allowing us to estimate that the long-lived TA signal decays ~80% over 5 μs, allowing us to approximate a decay lifetime of ~3 μs at 10 K. By varying the repetition rate of the laser while maintaining the sample at 78 K, we also collected several discrete repetition time TA data points at time delays of 5, 10, 20, and 40 μs (**Figure 4.5**), revealing a continued slow decay over the microsecond time scale.

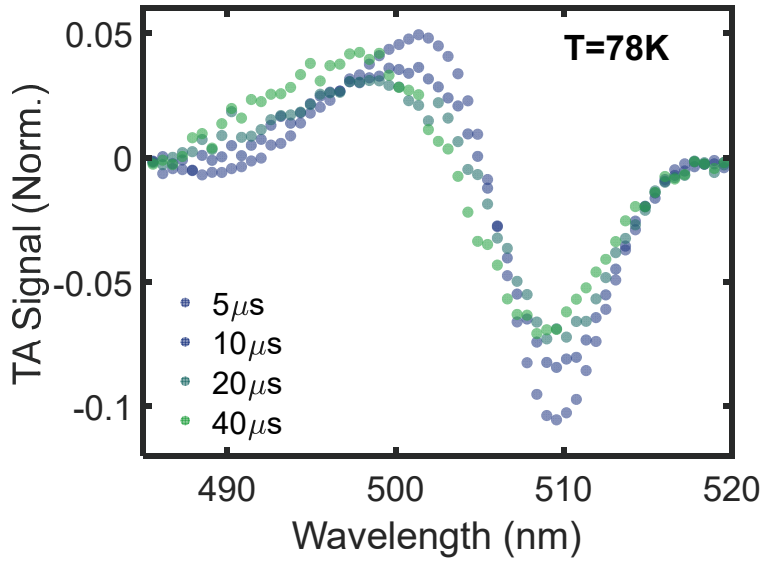


**Figure 4.5. Repetition time TA signal at various time delays.** Data collected at 78 K. Time delay was controlled by varying the repetition rate of the laser without changing the excitation density. The signal intensity is normalized to the GSB signal intensity at 4 ns.

As a final experimental observation, we collected fluence-dependent TA data over an excitation density range of <N>=0.04 to <N>=2.0 excitons per nanocrystal. The GSB peak decay traces for these data at 10 K are shown in **Figure 4.4d**. All traces exhibit the same general trends noted in the low fluence 10 K TA data shown in **Figure 4.3i**: a fast, sub-ns initial decay followed by a leveling off of the signal intensity after ~2 ns. Interestingly, the TA signal intensity at 3.9 ns, which can be taken as a measure of the long-lived state population, scales sub-linearly with excitation density, beginning to saturate at higher fluences. It is instead found to scale linearly with the number of NCs initially excited with exactly one exciton (based on a Poisson distribution), as shown by the dashed lines in **Figure 4.4d**.

### 4.7 Modeling Spectra and Dynamics of Long-Lived Species

To further characterize the long-lived state and help identify its origins, we apply target analysis to the low temperature TA data with the goal of resolving both the exciton and long-lived species spectra and dynamics. This analysis is performed on the 10 K TA data set, the temperature at which the signature of the long-lived species is most clear. One particular challenge with

modeling this system is the apparently similar spectra of the exciton and long-lived species, which can lead to multiple solutions with a similar goodness of fit but yielding different spectra and decay dynamics. In order to overcome this issue, we assume that all neutral excitons have fully decayed by 3 ns, such that the TA spectrum after that time comes only from the long-lived species. This is supported by the fast <500 ps exciton lifetime at liquid helium temperatures reported in the literature[239,242,243,252]. Our own experimental data further justifies this assumption, with negligible TA signal intensity decay after ~2 ns as seen in **Figure 4.3i**. The long-lived species spectrum $L(\lambda)$ is therefore directly taken to be the average of the observed TA spectrum after 3 ns. The following simple kinetic model is then proposed to model the observed TA spectrum as a function of both time delay $t$ and wavelength $\lambda$:

$$I(t,\lambda) = \left( A_X e^{\frac{-t}{\tau_X}} \right) X(\lambda) + \left( A_L e^{\frac{-t}{\tau_L}} \right) L(\lambda), \tag{4.1}$$

where $X(\lambda)$ is the spectrum of the neutral exciton, $\tau_i$ are the decay lifetimes of the exciton and long-lived species (as designed by the subscript), and $A_i$ are the decay prefactors, all of which are fitted parameters. For a given set of proposed decay parameters and a proposed exciton spectrum, the fitted TA spectrum can be generated and compared to the raw TA data to generate a sum-squared error. The parameters and spectra that minimize this error were found iteratively with a constrained optimization solver. More details on the setup and execution of this fitting method can be found in the **Methods** section.

The resultant normalized exciton and long-lived species spectra shown in **Figure 4.6a**. Fits to individual time slices are shown in **Figure 4.6b**, and colormaps of the actual and predicted TA spectra are given in **Figure 4.6c** and **Figure 4.6d**, respectively, confirming good agreement between the fit and experimental results. The fitted prefactors are 1 and 0.69 for the exciton and long-lived species, respectively, revealing a significant contribution of the long-lived species to the total TA spectrum. The fitted exciton lifetime is 720 ps, in generally good agreement with previous reports[239,242,243,252]. We note that several previous studies have found the $CsPbBr_3$ NC decay profile to be biexponential, with a ~200-500 ps fast component and a longer nanosecond-to-microsecond slow component[239,242,252], so a single exponential decay over 300-4000 ps for the exciton used here may not fully capture the system dynamics. The fitting extracts a long-lived

species lifetime of ~10 μs, with this value an approximation given that it predicts a decay of <0.1% over the 4 ns TA time window. The predicted microsecond persistence of the long-lived species is consistent with the microsecond signal found using repetition time TA in the previous section. Beyond the decay dynamics, we are also able to extract and compare the full lineshapes of the exciton and long-lived species. Similar to the excitonic spectrum, the long-lived species shows a dominant GSB signal (redshifted by ~1-2 nm and slightly narrowed compared to the exciton) and a higher energy IA feature with ~50% of the GSB intensity (but a distinctly different shape than the exciton).

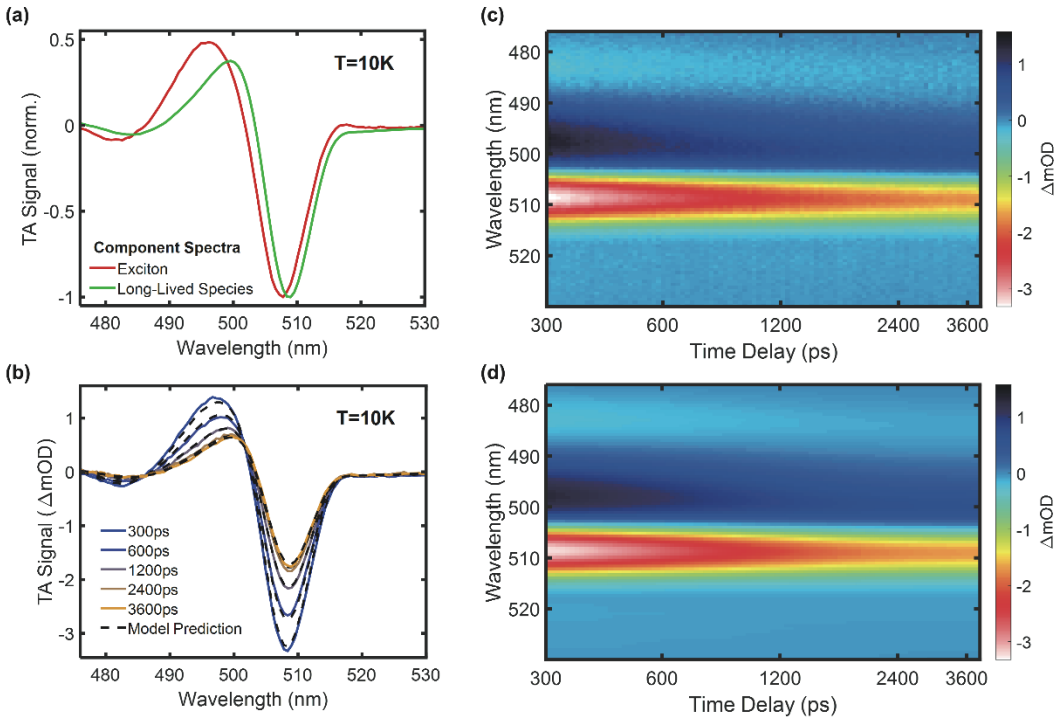


**Figure 4.6. Target analysis of 10K TA data to extract spectra and dynamics of exciton and long-lived species.** (a) Normalized fitted TA spectra of the exciton and long-lived species. (b) Raw TA time slices over the 300-3800 ps time window (solid lines) along with the corresponding model predicted curves (dashed lines). (c) Colormap of raw TA data taken at 10 K. (d) Colormap of the target analysis model prediction at 10 K.

## 4.8 Charging as the Source of These TA Dynamics

By combining the results of temperature-dependent and repetition time transient absorption spectroscopy, we have identified a long-lived species that forms in $CsPbBr_3$ nanocrystals at low

temperatures. This species has a lineshape generally similar to the exciton but with a spectral redshift, and it is capable of persisting for microseconds at cryogenic temperatures, orders of magnitude longer than the exciton lifetime. Based on these observations, we propose that the long-lived TA signal results from nanocrystal photocharging.

The process of photocharging has been previously studied in quantum dot systems and has been implicated as the primary cause of quantum dot blinking, or photoluminescence intermittency, in both traditional NC systems[245–250] and more recently in lead halide perovskite nanocrystals[244,253,266–268]. After excitation of a NC, the photogenerated electron-hole pair is split into two separated charge carriers, one remaining in the NC core while the other is transferred to an energetically and/or spatially separated trap site[250,257]. The charge separation process greatly reduces the electron-hole wavefunction overlap and suppresses electron-hole recombination until the separated carrier returns to the NC core, re-forming the neutral exciton state. Depending on the size of the barrier, neutralization can be orders of magnitude slower than exciton recombination[246], consistent with the sub-nanosecond exciton lifetime and microsecond charged NC lifetime reported here. Our results and proposed charging mechanism are also in agreement with recent work by Becker et al.[252], who performed TRPL studies on $CsPbBr_3$ NCs at 5 K and found microsecond delayed emission lifetimes assigned to a charge trapping process.

Our findings on the long-lived species' microsecond lifetime also allows us to rule out other possible sources of this TA signal. For example, NC size inhomogeneity can lead to a spectral shift over time if recombination rates change with NC diameter[159,269], but this effect should only impact lifetimes over a small range, not the 3 to 4 orders of magnitude difference in dynamics seen here. Another reasonable alternative might be that biexcitons or trions are the cause of the long-lived signal, given their reported spectral similarity to the exciton[159,270,271]. However, these species have the same recombination pathways as the exciton with the added nonradiative pathway from Auger processes, leading to a lifetime shorter than the exciton, not one significantly longer[272–275]. The close similarity in the TA spectra of the exciton and long-lived species—with GSB and IA peak energies and intensities only slightly shifted between the two—also supports that the long-lived TA signal is caused by an excited charge carrier. In contrast, an effect like a phase change is likely to have a more significant step change in the bandgap or spectral shape, as has been seen in the tetragonal to orthorhombic phase change bulk $MAPbI_3$ for example[276]. Further, the consistency

in spectral dynamics we found for the $CsPbBr_3$ NCs over a temperature range from 10 K to 100 K+ does not agree with a phase change or thermal response. A recent study from Kirschner *et al.* was only able to generate a photoinduced orthorhombic to cubic phase transition in $CsPbBr_3$ NCs at fluences 3 orders of magnitude higher than those used here[277]. Finally, recently published work found no evidence of a phase change in the same $CsPbBr_3$ NC-embedded polymer film sample over a 5-300 K temperature range[262], while a different report showed that thermal heating is negligible in this sample at low fluences.

### 4.9 Mechanistic Understanding of the Trapping Process

The exact mechanism for charging in nanocrystal systems is still subject to debate and likely varies with the material system and operating conditions, but several hypotheses have been developed. In traditional NCs, charging has been associated with undercoordinated atoms on the surface of the NC, creating energetic states within the bandgap at which carriers can become trapped[245,278]. Trap states linked to the capping ligands or the surrounding polymer matrix have also been reported.[258,259,279,280] In lead halide perovskite NCs, trapping mechanisms have similarly been tied to surface states[271,281–283], with surface passivation efforts shown to improve QY and reduce nonradiative recombination[271,282,283]. In contrast to surface and external effects, trapping at defect sites within the NC core has also been proposed as a mechanism for blinking in $CsPbBr_3$ perovskite NCs[266]. This was proposed to occur at vacancies or interstitial ions in the perovskite lattice, which are known to be common in lead halide perovskites[72,241,284] due to their uniquely high rates of ion migration[284,285].

A defining feature of the TA data set that may help provide insight into the nature of the charging mechanism is the strong temperature dependence of this process. This could be the result of either 1) the initial charging process being temperature-dependent, possibly due to a trap state density that varies with temperature, or 2) charging always occurring but the neutralization of the charged NC depending on temperature. The former would be consistent with our findings if the number of traps states or likelihood of trapping were significantly higher at lower temperatures (below ~100-200 K). Some reports in the literature support this mechanism, such as computational work studying surface defects in PbS and CdSe QDs that can form and disappear dynamically due to doping or photoexcitation[278,286], a process which might show a temperature dependence if there

were an energy barrier to creating or destroying the trap state. A separate study reported PbS QD surface trap state formation occurred preferentially at higher temperatures due to an ordered-disordered phase transition in the capping ligands[259], although this is opposite of the trend we see with temperature.

If instead the defect site density is constant with temperature and a significant population of charged NCs is always formed, it must instead be the detrapping process which exhibits a temperature dependence. This scheme better aligns our findings with a number of studies on both traditional QDs and perovskite NCs, where significant charge carrier trapping even at room temperature has been seen[244,246,247]. Temperature-dependent photoluminescence data has also been reported that suggests charging occurs at all temperatures and one or more energy barriers exist to neutralization of the charged NC state[257,287]. Other theoretical and experimental works have proposed various mechanistic schemes to describe the process of trapping and detrapping in NCs[249,250,252,260,264,268], highlighting the complexities of the system and the lack of a commonly accepted model that fully describes this process. In the temperature-dependent neutralization scenario, the room temperature TA dynamics we observe—showing monoexponential decay with no spectral shift—don't result exclusively from a population of excitons. Instead, the TA signal comes from both the exciton and charged NC populations, but the thermal energy is sufficient to allow for rapid transfer between the two states.

### 4.10 Modeling Temperature-Dependent Nanocrystal Dynamics

Next, we develop a model of this system consistent with the proposed temperature-dependent neutralization mechanism that allows us to quantify the energy barrier to neutralization. To do this, we employ a global fit that incorporates TA data as a function of time, wavelength, and temperature into a single model. We have already extracted the exciton and charged NC spectra at 10 K using the target analysis method, but spectra and the decay dynamics both vary with temperature. This creates a challenge in fitting the distinct exciton and charged NC spectra at higher temperatures, when the two populations are declining at similar rates and the combined TA spectrum appears time-invariant. To overcome this issue, we reduce the full TA spectra of each population down to a few key data points to be fitted—the intensity and wavelength of the GSB

and IA peaks—yielding four fittable parameters each for the exciton and charged NC spectra. These can then be bounded to ensure the two fitted spectra are distinct.

We developed a kinetic model to define the population dynamics as a function of time delay, similar to the target analysis of 10 K data performed previously. However, this model allows for neutralization of the charged NC state in addition to the exponential decay of the exciton. The kinetic equations for the population of the exciton ( $P_X$ ) and charged NC ( $P_C$ ) over time are shown in **Equations 4.2** and **4.3**:

$$\frac{dP_X}{dt} = -\frac{P_X}{\tau_X} + P_C A_{CX} e^{\frac{-E_{CX}}{k_B T}} \tag{4.2}$$

$$\frac{dP_C}{dt} = -P_C A_{CX} e^{\frac{-E_{CX}}{k_B T}} . \tag{4.3}$$

In this model, $A_{CX}$ and $E_{CX}$ represent the prefactor and energy barrier to charged NC neutralization, respectively. These fitting parameters are held constant at all temperatures, along with the initial conditions $P_{X,0}$ and $P_{C,0}$. On the other hand, the exciton lifetime, $\tau_X$, and the exciton and charged NC spectral parameters are independently fitted at each temperature.

TA data over a temperature range of 10-300 K and a time window of 300-3800 ps were fitted to the model using a nonlinear optimization algorithm, yielding the solution shown in **Figures 4.7** and **4.11**. The global fit gives a 104 meV energy barrier to charged nanocrystal neutralization. This is sufficiently large that effectively no charged NC neutralization occurs on a 4 ns time scale at 10-78 K, but small enough that neutralization is much faster than exciton recombination at room temperature, with a transition in the region of 130-190 K, as shown in **Figure 4.7a**. These population dynamics also fully reproduce the temperature-dependent dynamics seen in the TA data. Specifically, the model replicates the redshift seen in the IA and GSB peak positions at low temperatures but not at higher temperatures, as shown in **Figure 4.7b**. The model results also show that 42% of NCs not in the ground state are charged and 58% are populated by a neutral exciton. This is a very significant fraction of charged NCs, and is consistent with the target analysis results showing 41-58% of NCs are initially charged. However, these numbers are based

on data from 300 ps onward and extrapolated back to time zero, so they can only be considered an approximation. See **Figure 4.11** for more details on the global fitting results.

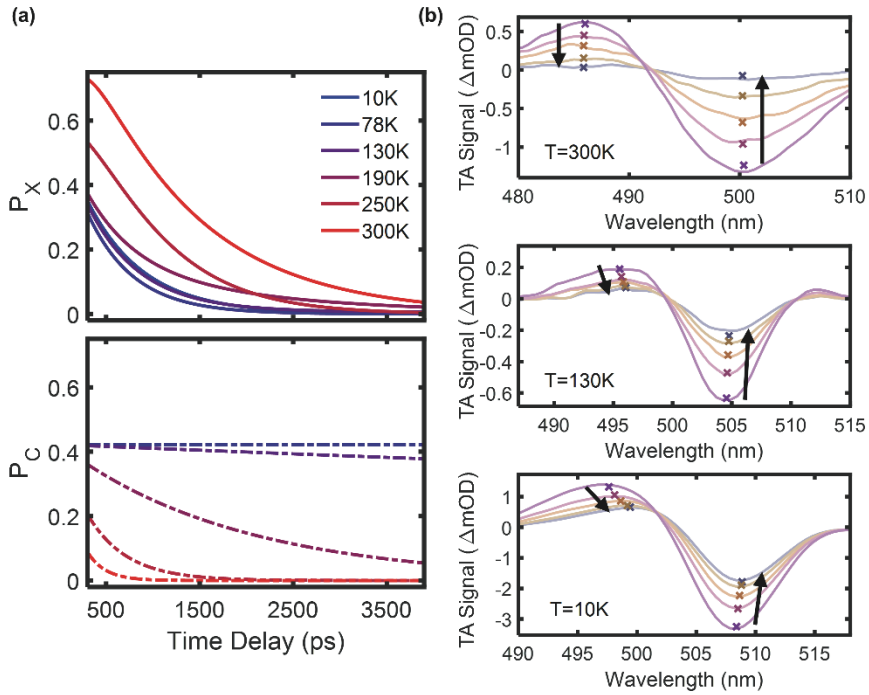


**Figure 4.7. Results of global fitting analysis for all temperatures.** (a) Exciton (top) and charged NC (bottom) populations as a function of temperature and time delay. The charged NC population shows effectively no decay at 10 K or 78 K, but almost complete neutralization by 300 ps at 300 K. (b) Raw TA data (curves) and model fits (x markers) at 300 K (top), 130 K (middle), and 10 K (bottom), showing experimental dynamics in the IA and GSB peaks are well-captured by the model. Plotted time points are 300 ps, 600 ps, 1000 ps, 1800 ps, and 3500 ps.

If the kinetic model is projected forward to microsecond time delays, the 104 meV neutralization energy barrier predicts a significant charged NC population at 5 µs for temperatures of 78 K and below, with a transition occurring at 100 K. This qualitatively matches actual trends in the temperature-dependent repetition time TA data (**Figure 4.10**). However, the TA signal intensity from 4 ns to 5 µs drops by a factor of 5-10 even at 10 K, while the model predicts no change in charged NC population under the same conditions. These dynamics cannot be reproduced using a simple kinetic model with one energy barrier to neutralization. Instead, this points to a more complex mechanism involving multiple energy barriers or neutralization that occurs *via* either overcoming an energy barrier or tunneling. These complex kinetics have been

proposed in the past[250,264] and point to multiple trapping mechanisms or trap states rather than supporting a single trap model.

### 4.11 Conclusions

We have employed temperature-dependent transient absorption spectroscopy to uncover signs of significant photocharging in $CsPbBr_3$ perovskite NCs. Our ensemble results are in contrast to some other reports on single $CsPbBr_3$ NCs showing near unity quantum yield and blinking-free photoluminescence[239]. This discrepancy highlights the different likelihood of charging occurring for different NCs, which points to a charging mechanism that depends on local conditions (e.g. surface defects). We also find the charged NC fraction shows a sub-linear dependence with excitation density (<N>), as shown in **Figure 4.4d**. This is in direct contrast with previous work attributing NC charging processes to an Auger-mediated ionization mechanism in both traditional[261,288,289] and perovskite[244] nanocrystals, which results in charging having a super-linear dependence with excitation density. Instead, we find the charged NC fraction at 10 K scales linearly with the fraction of NCs that contain exactly one exciton after photoexcitation. This may suggest a counter-intuitive mechanism by which multiply-excited NCs (e.g. biexcitons) are subsequently able to avoid forming a charge-separated state, perhaps through a trap passivation mechanism consistent with previous observations of photoactivation in lead halide perovskite nanocrystals[253,268] and thin films[290,291]. Finally, a global fit to the temperature-dependent TA data was used to study the mechanism of charged NC neutralization in this system. Fits to the 0-4 ns TA data yielded a 104 meV energy barrier to neutralization, which was found to be qualitatively consistent with repetition time TA results. However, the nanosecond and microsecond TA results together suggest it's likely that multiple energy barriers or trap states exist in $CsPbBr_3$ NCs, which will take further investigation to fully quantify.

Our findings are important to improve the understanding of charging and neutralization processes in perovskite NCs. These results can help drive synthetic improvements towards higher quantum yield, blinking-free NCs for use in device applications like LED displays. In particular, identification and passivation of the deepest trap states is of critical importance for the use of perovskite NCs as quantum emitters, which are held at cryogenic temperatures and most susceptible to the charging processes studied here[16,239].

## 4.12 Methods

**Transient absorption spectroscopy.** Transient absorption spectroscopy was performed in the same experimental setup described in **Section 3.12** under Impulsive Vibrational Spectroscopy Setup, including the same laser system, pump light generation, and data collection. The $CsPbBr_3$ perovskite nanocrystal-embedded polymer films were similarly mounted in a vacuum cryostat (Janis Research, ST-100). The exciton density per NC, <N>, was calculated using from the laser spot size, fluence, repetition rate, and absorption cross section. The absorption cross section was adapted from measurements performed by the Hens group[292] at 400 nm excitation wavelength. This value was scaled to an excitation wavelength of 450 nm using our linear absorption spectrum (**Figure 4.1a**). Further details on the TA setup have also been published previously[121].

**Target analysis modeling.** In order to extract the spectra of the exciton and charged nanocrystal at low temperatures (as seen in **Figure 4.6a**), the following method was followed. First, it was assumed that the exciton and any multi-carrier species signals have fully decayed by the end of the TA time window. Thus, the TA signal after 3ns is entirely from the charged NC, giving us the charged NC spectral shape before applying a fitting algorithm. This assumption is important given the very similar lineshapes of the exciton and charged NC spectra.

The charged NC spectrum $C(\lambda)$ is extracted by averaging the last ten time delay points (covering 3000-3900 ps), and then smoothing this data to reduce noise. A constrained optimization algorithm (fmincon in MATLAB) is then applied to extract the exciton spectrum $X(\lambda)$ and the decay dynamics of both species. The algorithm was supplied TA data taken at 10 K with <N>=0.3 over a wavelength range of 477-530 nm and a time range of 300-3800 ps. Several kinetic models were considered, but the simplest model accurately capturing the system dynamics was single exponential decay of both the exciton and the charged NC. Reasonable bounds were supplied, and the resulting parameters were confirmed not to lie at the edges of the parameter space.

## 4.13 Appendix A Additional Figures

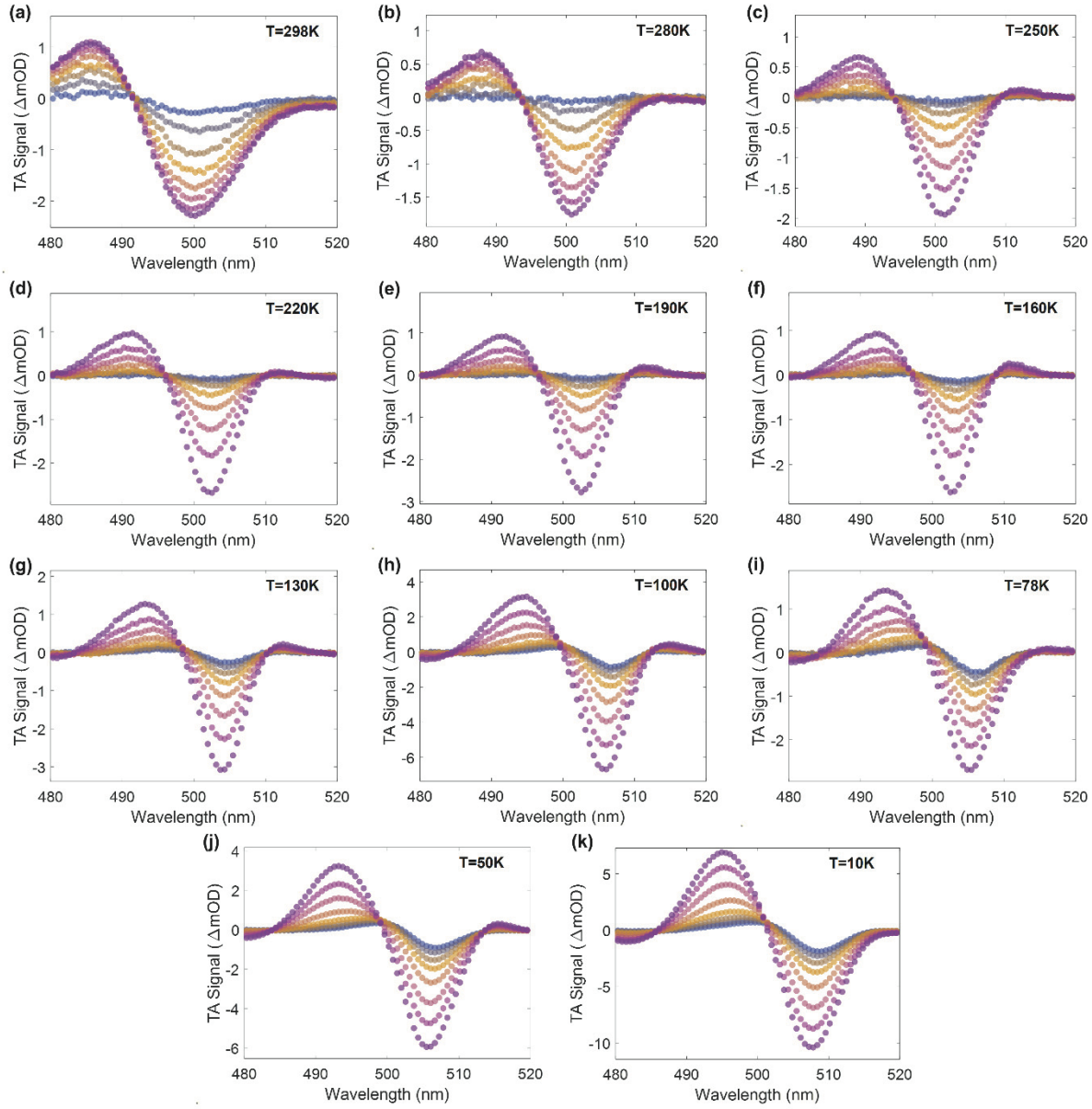


**Figure 4.8. Transient absorption spectra at all temperatures.** TA spectral slices over the first 2 ns at the temperatures inset in each sub-figure. The displayed curves (from purple to blue) were measured at time points of 10, 20, 50, 100, 200, 500, 1000, and 2000 ps.

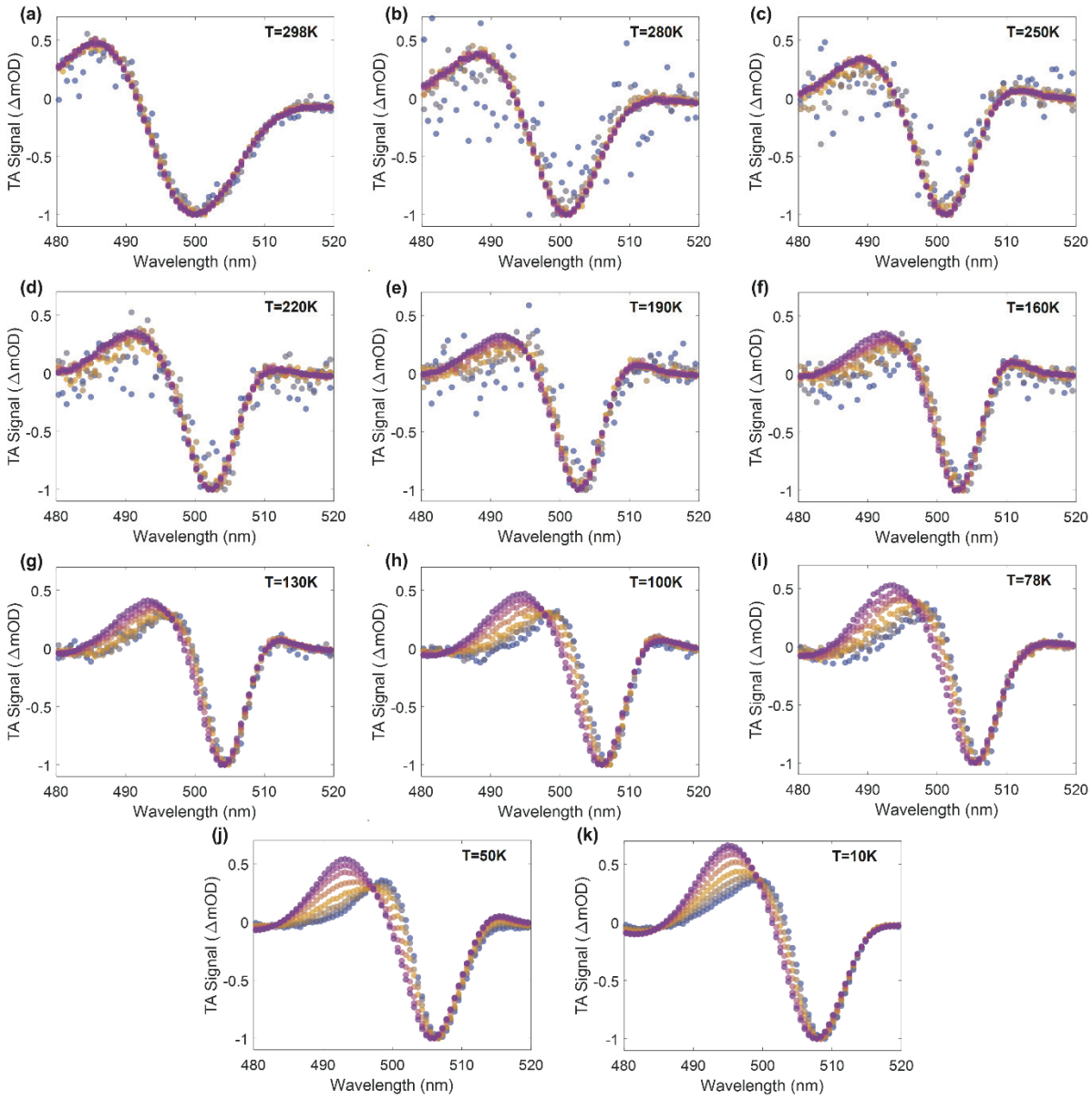


**Figure 4.9. Normalized transient absorption spectra at all temperatures.** TA spectral slices over the first 2 ns at the temperatures inset in each sub-figure. The displayed curves (from purple to blue) were measured at time points of 10, 20, 50, 100, 200, 500, 1000, and 2000 ps.

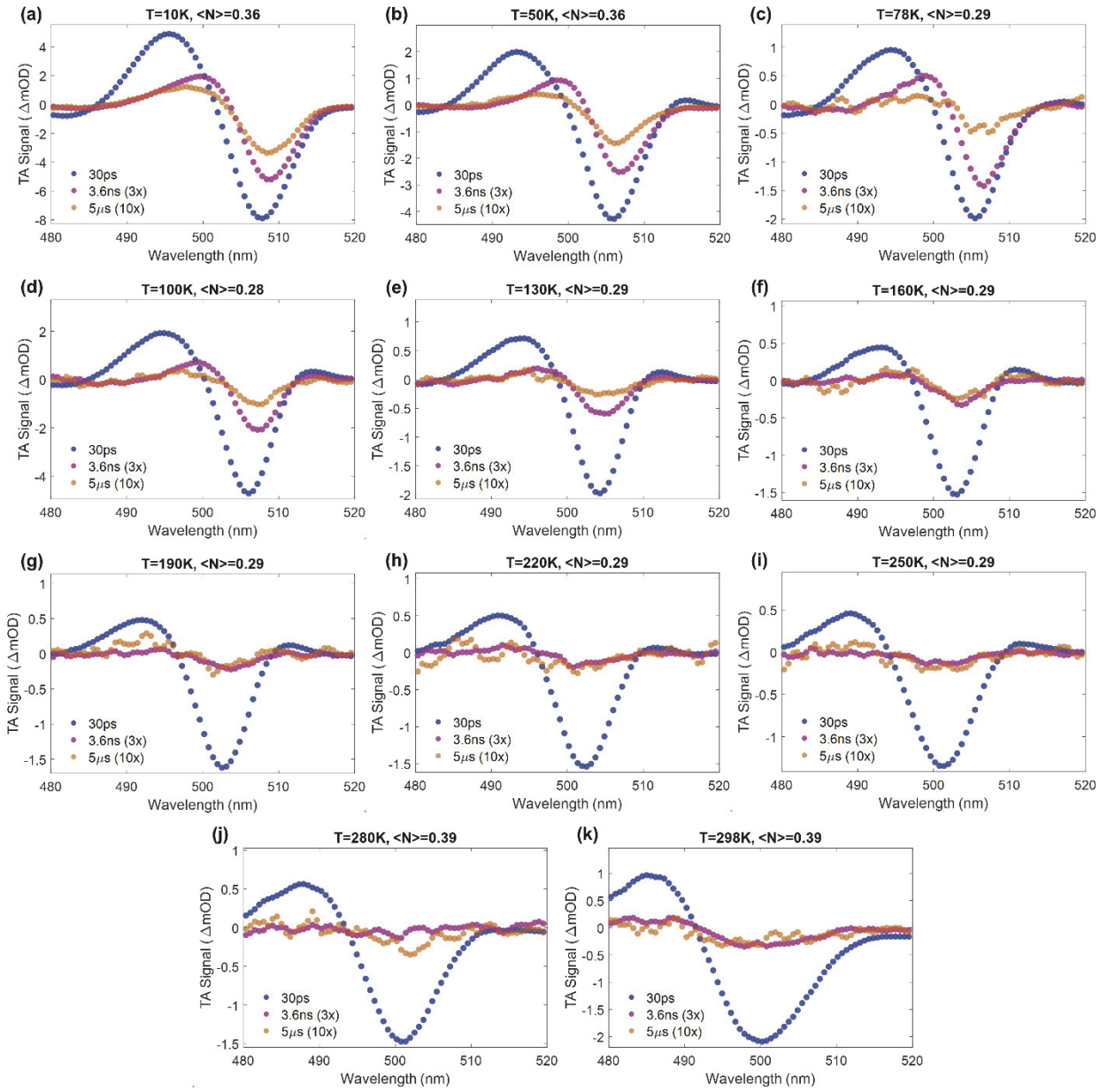


**Figure 4.10. Repetition time transient absorption spectra at all temperatures.** TA spectral slices at (blue) 30 ps, (pink) 3.6 ns, and (orange) 5 μs at the temperatures listed for each sub-figure. The intensities of the 3.6 ns and 5 μs curves are increased by factors of 3 and 10, respectively, for clarity.

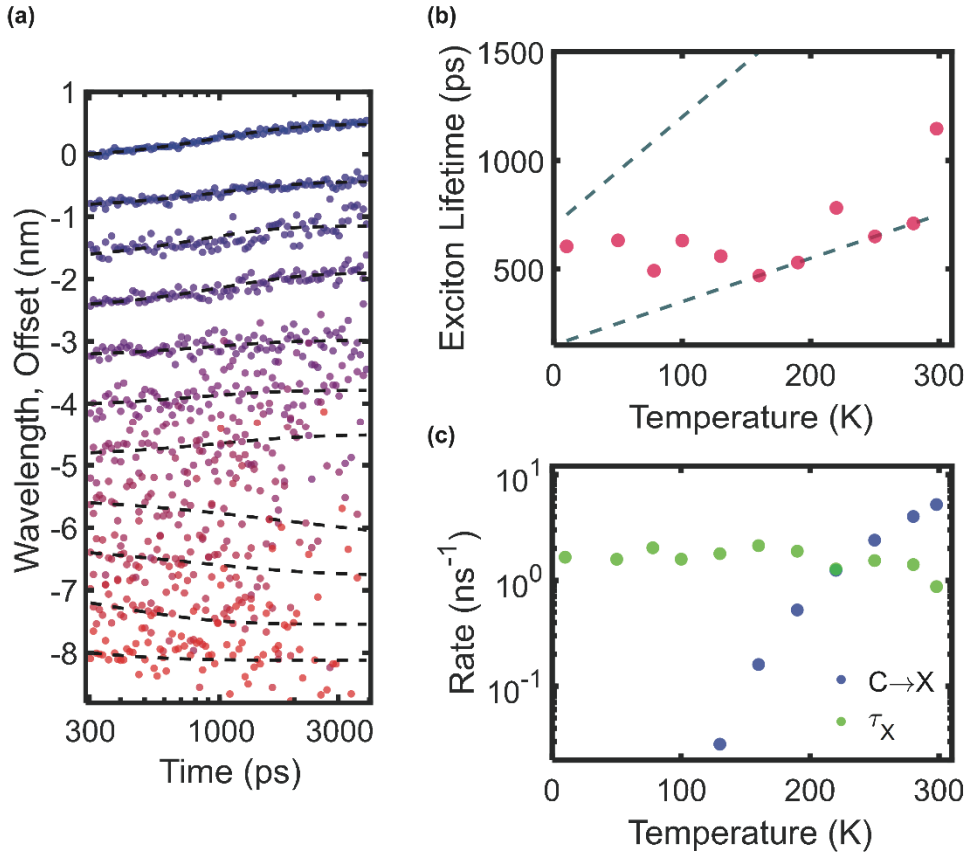


**Figure 4.11. Global fitting results.** (a) Ground state bleach wavelength shift versus time delay. Markers represent the experimental data while dashed lines show the fitted results. All fitted temperatures are shown, starting with 10 K (top, blue) and increasing temperature down the figure to 300 K (bottom, red). (b) Fitted exciton lifetimes (pink markers) along with upper and lower bounds (gray dashed lines). (c) Comparison of the rates of exciton recombination (green) and charged NC to exciton neutralization process (blue).

# Chapter 5
# Conclusion and Future Directions

*Distress not yourself if you cannot at first understand the deeper mysteries of Spaceland. By degrees they will dawn upon you.*

Edwin A. Abbott, Flatland: A Romance of Many Dimensions[293]

## 5.1 Next Steps

As my thesis comes to a close I reflect on the fact that, in scientific research, the story is never truly complete. In this chapter, I will briefly discuss some of the most interesting unanswered questions and promising future directions related to my thesis. Additional progress in these areas will further improve our understanding of the unique properties of hybrid organic-inorganic semiconductor nanomaterials.

## 5.2 Future Studies of Electron-Phonon Interactions in Metal Organic Chalcogenolates

In the study of metal organic chalcogenolates (MOCs) presented in Chapter 3, we made huge advances in our understanding of electron-phonon interactions in 2D AgSePh. We identified impulsive vibrational spectroscopy (IVS) as a powerful technique to study electron-phonon coupling in the time domain and specifically analyze coupling to the electronic excited state. We also showed the advantage of combining multiple experimental and computational techniques to glean more information about the system.

A very natural progression of this work would be to extend it to other materials, starting with other members of the MOC material family. The most obvious candidate material is AgTePh, a 2D MOC that is structurally very similar to AgSePh but exhibits substantially different optoelectronic properties[86,95,96]. The Tisdale group has synthetic capabilities to produce this material, and we have recently published a report comparing the properties of AgSePh and

AgTePh[96]. In this study, we concluded that the broad and red-shifted emission spectrum of AgTePh is likely caused by self-trapped exciton formation, a phenomenon associated with strong electron-phonon interactions and previously reported by the Tisdale group and others in 2D perovskites[121,294–296].

To further investigate exciton-phonon coupling in AgTePh, we recently collected preliminary IVS data on this material, as shown in **Figure 5.1**. The 2D colormap of raw transient absorption data for AgTePh is given in **Figure 5.1a**, with coherent oscillations clearly visible, consistent with strong exciton-phonon coupling. By applying the same methods introduced in Chapter 3, we can subtract off the electronic dynamics, leaving only the coherent vibrational data shown in **Figure 5.1b**. Next, we can select a wavelength region to sum over and compute the Fourier transform of the data, giving the IVS frequency-domain results shown in **Figure 5.1c** and **Figure 5.1d** for two different wavelength regions. Alternatively, we can fit the vibrational oscillations in the time domain to extract both the frequencies and decoherence times of the different modes, as shown in **Figure 5.1e**. For additional information on electron-phonon coupling, impulsive vibrational spectroscopy, and data analysis methods used here, see Chapter 3 of this thesis.

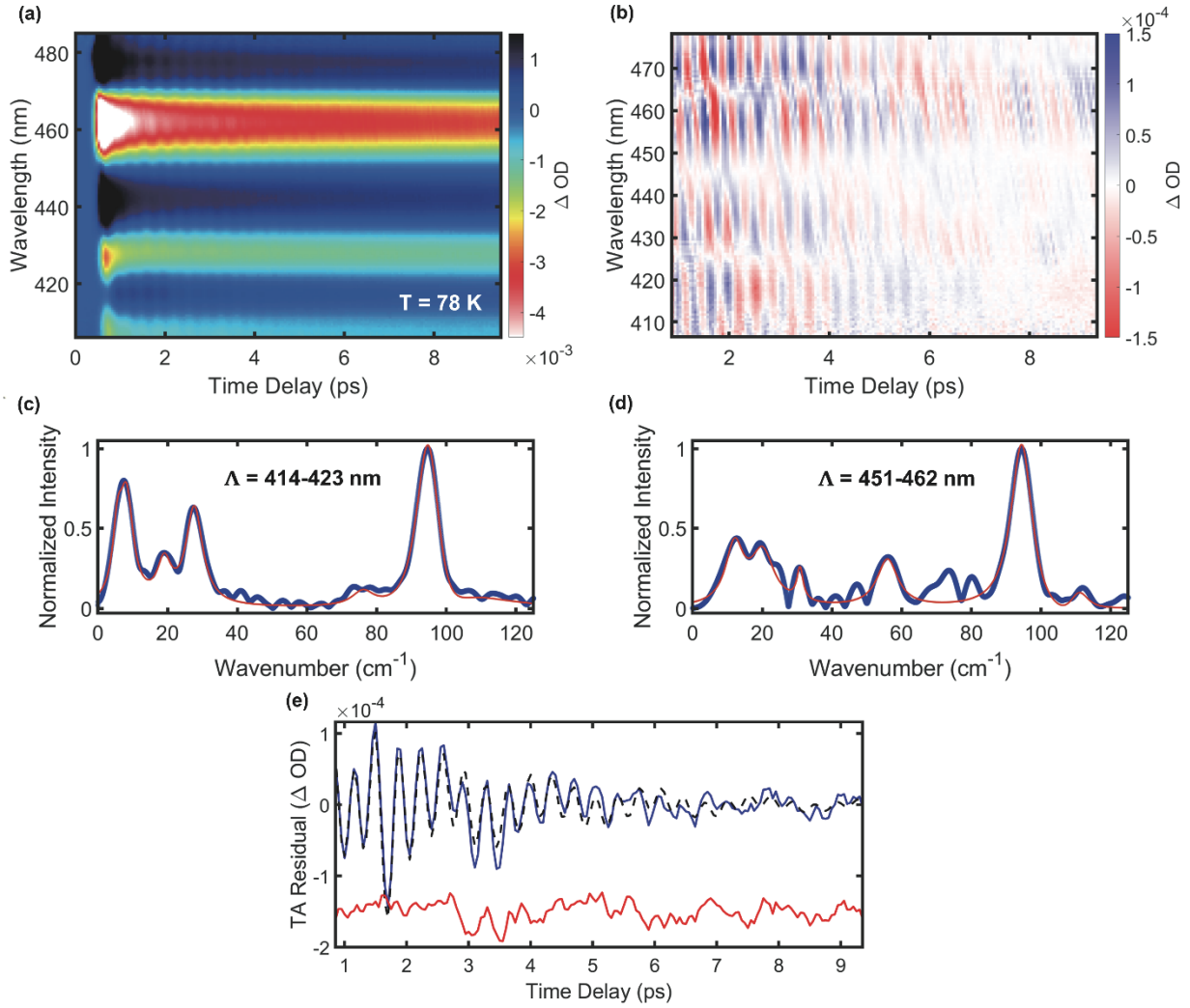


**Figure 5.1 Impulsive vibrational spectroscopy study of 2D AgTePh.** (a) IVS color map of AgTePh collected at 78 K, showing three separate excitonic features. (b) Coherent oscillations seen in AgTePh after the electronic dynamics are subtracted off. (c) IVS frequency domain spectrum of AgTePh at 78 K after performing a Fourier transform of the time-domain data over a 414-423 nm wavelength region. The blue markers represent the IVS results, while the red line is a Lorentzian fit to the data. (d) IVS frequency domain spectrum of AgTePh, equivalent to panel (c) but performed instead over a 451-462 nm wavelength region. (e) IVS time domain data (blue) summed over a 451-462 nm wavelength range. A decaying sine wave fit to the data is overlaid (dashed black line), as well as the difference between the experimental signal and fit, offset for clarity (red).

The most noteworthy feature that appears in these data is the ~94 $cm^{-1}$ vibrational mode which dominates both the short and long wavelength region IVS spectra (**Figure 5.1c** and **Figure 5.1d**). Due to its frequency and intensity, it is reasonable to suspect that this vibrational mode may be equivalent to the 99 $cm^{-1}$ γ mode found in AgSePh. The frequency shift in this mode may tell us more about structural differences between these two materials. Excluding this dominant mode,

the IVS spectrum of AgTePh is very distinct between the short and long wavelength regions, in contrast to our observations of AgSePh. This suggests significantly different vibrational coupling to the different band edge excitonic states in the system. Interpretation of this observation, as well as how self-trapped exciton formation may play a role in the IVS spectrum, is beyond the scope of this discussion. However, additional analysis and comparisons to other experimental and computational techniques may yield very interesting and insightful findings on exciton-phonon coupling in AgTePh.

More generally, IVS and the other techniques introduced in Chapter 3 can be applied to study electron-phonon coupling in other MOC systems. For example, the Tisdale group has had success synthesizing AgSePhMe, an analog of AgSePh with a methylated phenyl ring[88], as well as other MOCs with different functional groups added to the organic layer. This methodology can also be applied more broadly to other hybrid nanomaterial systems with strong electron-phonon coupling to understand the physics and optoelectronic impacts of this phenomenon.

### 5.3 Synthesis and Characterization of 2D Perovskite Heterostructures

Another area of recent interest for me has been 2D perovskite heterostructures. This particular topic represents the union of my previous co-authored study investigating 2D perovskites[121] with unpublished work on 2D-0D heterostructures from earlier in my PhD (see **Figure 5.2**). Many previous studies have been performed on 2D heterostructures comprised of 2D van der Waals materials, including transition metal dichalcogenides, graphene, hexagonal boron nitride, and others[46,54,297–301]. These structures exhibit interesting physical phenomena such as ultrafast charge and energy transfer[300], superconductivity[54], and charge-transfer or interlayer exciton formation[301,302], which motivates parallel studies of 2D perovskite heterostructures to determine if they display similar emergent properties. In fact, there have been a number of recent studies investigating charge and energy transfer in 2D perovskite heterostructures[23,303–307], although almost all of these studies have utilized "mixed n" 2D-2D perovskite samples with multiple crystal domains of different 2D layer thicknesses (e.g. "n"=2, 3, 4, and 5 lead halide octahedra per layer), likely in part due to the difficulty in synthesizing thickness-pure heterostructure samples for study. In contrast, our group's expertise in growing high quality 2D perovskites with tunable composition[50,101,308] enables us to synthesize many possible combinations

of well-controlled 2D perovskite heterostructures. We can also utilize the pick-and-place PDMS stamping method developed by Pan *et al.*[309] to form 2D perovskite heterostructures with exact control of layer thickness, location, and orientation.

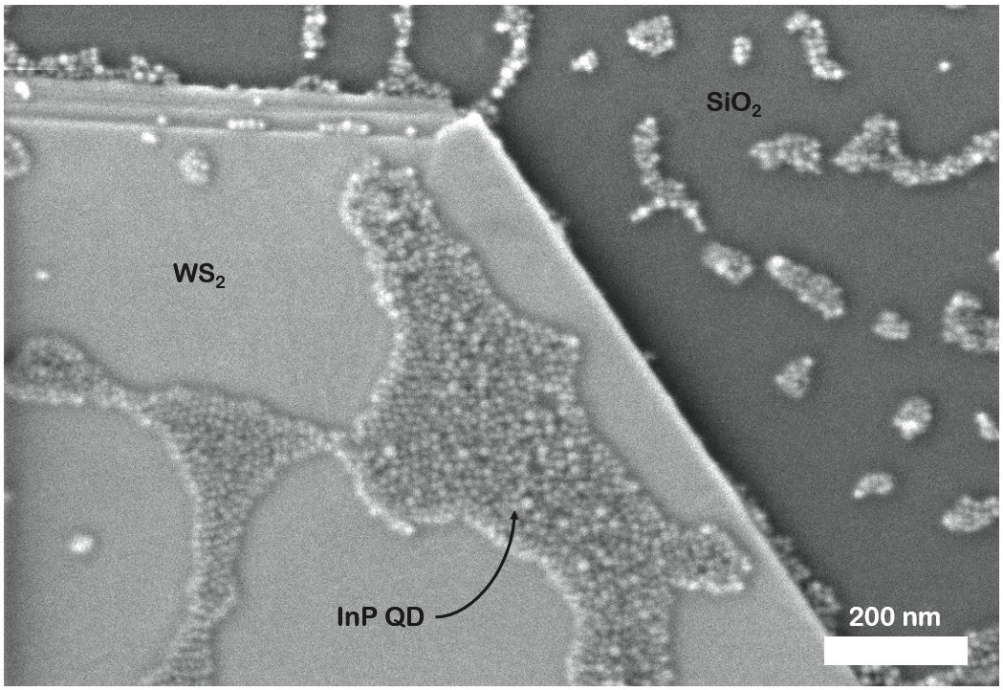


**Figure 5.2. 0D-2D InP nanocrystal on $WS_2$ heterostructure.** Scanning electron micrograph (SEM) of indium phosphide-zinc sulfide (InP/ZnS) core-shell nanocrystals or quantum dots (QDs) deposited on a few-layer tungsten disulfide ($WS_2$) sheet. Nanocrystals show sub-monolayer coverage on both $WS_2$ and on the underlying $SiO_2$/Si substrate.

Our group has begun preliminary work into synthesizing and studying these 2D perovskite structures. In collaboration with Fabio Marangi, a visiting PhD student from Politecnico di Milano, I was able to perform basic optical characterization of mixed 2D perovskite samples. We synthesized several different 2D perovskites, including n=1 HA $PbI_4$, n=1 PEA $PbI_4$, and n=1 PEA $PbBr_4$ (with n=1 denoting a single layer of perovskite lead halide octahedra, HA = hexylammonium organic spacing ligands, and PEA = phenylethylammonium organic spacing ligands). The stamp transfer method was then used to combine multiple 2D perovskites onto a single substrate. Initial results are provided in **Figure 5.3**, showing successful stamp transfer methodology and pure n=1 layer thickness based on photoluminescence spectra. However, we encountered some challenges in this process that must still be resolved. Low substrate coverage of the 2D perovskites made it difficult to create a heterostructure by chance when using the stamping

method. This may necessitate performing the stamping process in a microscopy setup to find quality microcrystals of both 2D perovskite types and ensure their alignment during stamping. Also, when attempting to generate an n=1 PEA $PbI_4$ and n=1 PEA $PbBr_4$ heterostructure, the PL emission from an isolated n=1 PEA $PbI_4$ microcrystal was green in the center of the crystal, as anticipated, but unexpectedly appeared cyan near the edges. This suggests bromide migration and ion exchange into the edges of the n=1 PEA $PbI_4$ microcrystal from trace leftover solvent used in the n=1 PEA $PbBr_4$ synthesis, another issue which will need to be addressed. Ultimately, after successful synthesis of a 2D perovskite heterostructure, we would be interested in tuning the structure to achieve desired properties such as preferential charge or energy transfer, controllable exciton binding energy, and the formation of interlayer excitons. This will be enabled by the highly tunable composition of 2D perovskites, as illustrated in **Figure 5.4a-e**.

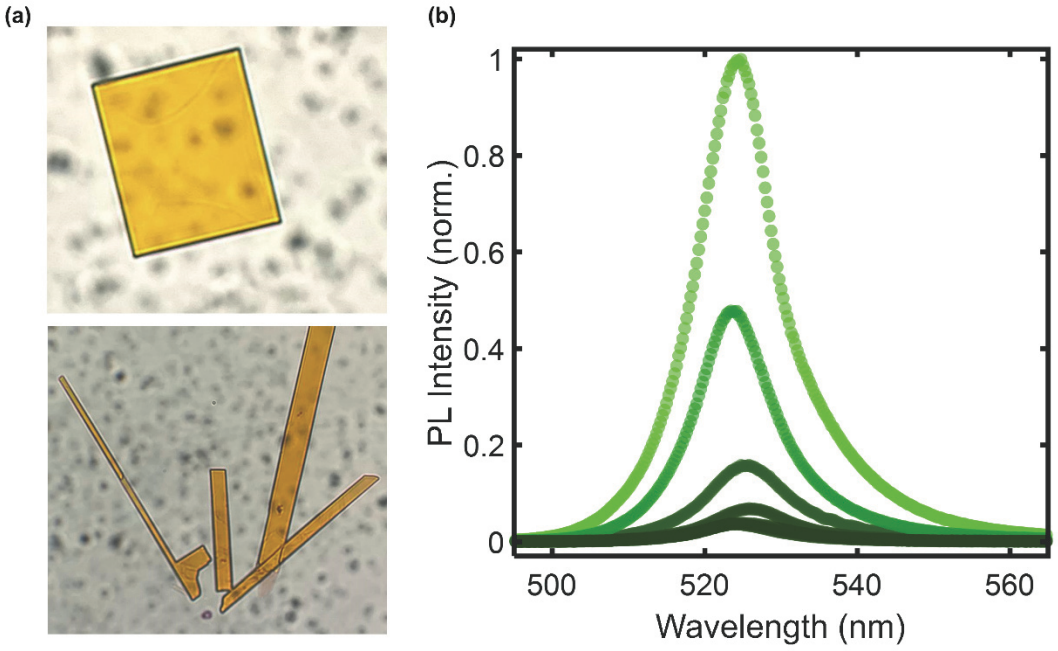


**Figure 5.3. 2D perovskite synthesis and characterization.** (a) Optical microscope images of stamp transferred n=1 HA $PbI_4$ 2D perovskite microcrystals. (b) Steady state photoluminescence (PL) collected from stamp transferred n=1 PEA $PbI_4$ 2D perovskite microcrystals. Different curves correspond to PL collected from different microcrystals, showing consistent phase pure n=1 morphology.

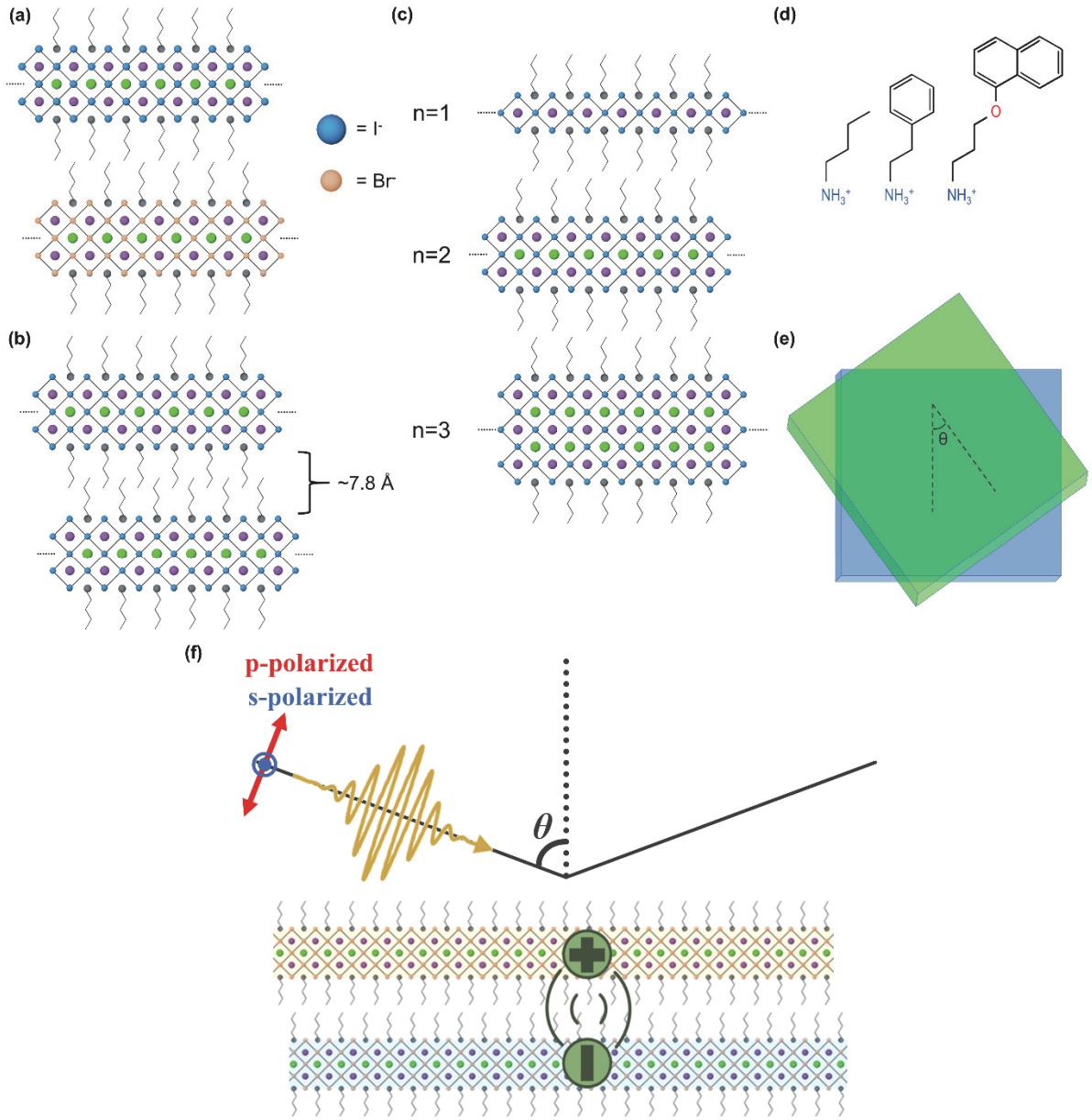


**Figure 5.4. 2D perovskite heterostructure tunability and characterization.** (a-e) Variables for tuning the properties of 2D perovskite heterostructures, including (a) chemical composition, (b) interlayer spacing, (c) layer thickness, (d) ligand chemistry, and (e) twist-angle orientation. (f) Schematic of polarization-dependent transient absorption spectroscopy (PDTA) on an interlayer exciton in a 2D perovskite heterostructure.

We are particularly interested in studying interlayer excitons (IE), which form when a charge carrier transfers across the heterostructure interface but the electron and hole remain Coulombically bound[302]. Also called charge transfer excitons, this type of exciton exhibits properties that are different from the in-plane excitons in either parent material, such as tunable

emission energy, long recombination lifetimes, and orientation anisotropy[310]. IEs have been studied in other 2D material fields such as transition metal dichalcogenides[300,311], but they have only been documented in a 2D perovskite heterostructure in one recent publication[312].

To investigate interlayer exciton (IE) formation in 2D perovskite heterostructures, we can employ polarization-dependent transient absorption (PDTA) spectroscopy, as illustrated in **Figure 5.4f**. This novel technique follows the same experimental setup as regular transient absorption (TA), but with the added dimension of varying the polarization of the probe pulse. By probing a 2D heterostructure at grazing incidence, the anisotropic transition dipole moment of an IE (oriented normal to the 2D plane) will show a stronger signal when using p-polarized probe light than s-polarized probe light. This technique allows for the unambiguous assignment of measured TA signals to the IE rather than defects, self-trapped excitons, or other excited state species.

## 5.4 Concluding Thoughts

Hybrid organic-inorganic semiconductor nanomaterials are an immensely broad and complex set of materials. I have enjoyed the role I've played using ultrafast spectroscopy to identify and interpret just a few of their unique characteristics. While there are still many years of research and development left to be done, designer nanomaterials engineered with tailored material properties have the potential to drive substantial advances in the fields of optics, electronics, communications, biotechnology, quantum information, and more.

# References


1. *The Feynman lectures on physics*. (Pearson, Addison-Wesley, 2006).
2. Green, M. A., Ho-Baillie, A. & Snaith, H. J. The emergence of perovskite solar cells. *Nature Photonics* **8**, 506–514 (2014).
3. Tsai, H. *et al.* High-efficiency two-dimensional Ruddlesden–Popper perovskite solar cells. *Nature* **536**, 312–316 (2016).
4. Ganesan, A., Houtepen, A. & Crisp, R. Quantum Dot Solar Cells: Small Beginnings Have Large Impacts. *Applied Sciences* **8**, 1867 (2018).
5. Bernardi, M., Palummo, M. & Grossman, J. C. Extraordinary Sunlight Absorption and One Nanometer Thick Photovoltaics Using Two-Dimensional Monolayer Materials. *Nano Letters* **13**, 3664–3670 (2013).
6. Dey, A. *et al.* State of the Art and Prospects for Halide Perovskite Nanocrystals. *ACS Nano* **15**, 10775–10981 (2021).
7. Adjokatse, S., Fang, H.-H. & Loi, M. A. Broadly tunable metal halide perovskites for solid-state light-emission applications. *Materials Today* **20**, 413–424 (2017).
8. Bera, D., Qian, L., Tseng, T.-K. & Holloway, P. H. Quantum Dots and Their Multimodal Applications: A Review. *Materials* **3**, 2260–2345 (2010).
9. Gao, X. *et al.* Ruddlesden–Popper Perovskites: Synthesis and Optical Properties for Optoelectronic Applications. *Advanced Science* **6**, 1900941 (2019).
10. Samuel, I. Electrifying quantum dots for lasers. *Nature Materials* **17**, 9–10 (2018).
11. Wu, K., Park, Y.-S., Lim, J. & Klimov, V. I. Towards zero-threshold optical gain using charged semiconductor quantum dots. *Nature Nanotechnology* **12**, 1140–1147 (2017).
12. Jung, H., Ahn, N. & Klimov, V. I. Prospects and challenges of colloidal quantum dot laser diodes. *Nat. Photon.* **15**, 643–655 (2021).
13. Konstantatos, G. & Sargent, E. H. Colloidal quantum dot photodetectors. *Infrared Physics & Technology* **54**, 278–282 (2011).
14. Kufer, D. *et al.* Hybrid 2D–0D MoS2–PbS Quantum Dot Photodetectors. *Advanced Materials* **27**, 176–180 (2015).
15. Wu, H. *et al.* All-Inorganic Perovskite Quantum Dot-Monolayer MoS2 Mixed-Dimensional van der Waals Heterostructure for Ultrasensitive Photodetector. *Advanced Science* **5**, 1801219 (2018).
16. Kagan, C. R., Bassett, L. C., Murray, C. B. & Thompson, S. M. Colloidal Quantum Dots as Platforms for Quantum Information Science. *Chem. Rev.* (2020) doi:10.1021/acs.chemrev.0c00831.
17. Chatterjee, A. *et al.* Semiconductor qubits in practice. *Nat Rev Phys* **3**, 157–177 (2021).
18. Aharonovich, I., Englund, D. & Toth, M. Solid-state single-photon emitters. *Nature Photon* **10**, 631–641 (2016).
19. Baig, N., Kammakakam, I. & Falath, W. Nanomaterials: a review of synthesis methods, properties, recent progress, and challenges. *Mater. Adv.* **2**, 1821–1871 (2021).

20. Ouwens, C. D. & Heijligers, H. Recrystallization processes in polycrystalline silicon. *Appl. Phys. Lett.* **26**, 569–571 (1975).
21. Geim, A. K. & Novoselov, K. S. The rise of graphene. *Nature Mater* **6**, 183–191 (2007).
22. Giovanni, D. *et al.* Origins of the long-range exciton diffusion in perovskite nanocrystal films: photon recycling vs exciton hopping. *Light: Science & Applications* **10**, 2 (2021).
23. Williams, O. F. *et al.* Energy transfer mechanisms in layered 2D perovskites. *J. Chem. Phys.* **148**, 134706 (2018).
24. Protesescu, L. *et al.* Nanocrystals of Cesium Lead Halide Perovskites (CsPbX3, X = Cl, Br, and I): Novel Optoelectronic Materials Showing Bright Emission with Wide Color Gamut. *Nano Lett.* **15**, 3692–3696 (2015).
25. Sun, L. *et al.* Bright infrared quantum-dot light-emitting diodes through inter-dot spacing control. *Nature Nanotech* **7**, 369–373 (2012).
26. Coe, S., Woo, W.-K., Bawendi, M. & Bulović, V. Electroluminescence from single monolayers of nanocrystals in molecular organic devices. *Nature* **420**, 800–803 (2002).
27. Weidman, M. C., Beck, M. E., Hoffman, R. S., Prins, F. & Tisdale, W. A. Monodisperse, Air-Stable PbS Nanocrystals via Precursor Stoichiometry Control. *ACS Nano* **8**, 6363–6371 (2014).
28. Freestone, I., Meeks, N., Sax, M. & Higgitt, C. The Lycurgus Cup — A Roman nanotechnology. *Gold Bull* **40**, 270–277 (2007).
29. Ekimov, A. I., Efros, L. & Onushchenko, A. A. Quantum Size Effect in Semiconductor Microcrystals. *Solid State Communications* **56**, 921–924 (1985).
30. Efros, Al. L. & Efros, A. L. Interband absorption of light in a semiconductor sphere. *Sov. Phys. Semicond.* **16**, 772–775 (1982).
31. Rossetti, R., Nakahara, S. & Brus, L. E. Quantum size effects in the redox potentials, resonance Raman spectra, and electronic spectra of CdS crystallites in aqueous solution. *The Journal of Chemical Physics* **79**, 1086–1088 (1983).
32. Murray, C. B., Norris, D. J. & Bawendi, M. G. Synthesis and characterization of nearly monodisperse CdE (E = sulfur, selenium, tellurium) semiconductor nanocrystallites. *Journal of the American Chemical Society* **115**, 8706–8715 (1993).
33. Weidman, M. C., Seitz, M., Stranks, S. D. & Tisdale, W. A. Highly Tunable Colloidal Perovskite Nanoplatelets through Variable Cation, Metal, and Halide Composition. *ACS Nano* **10**, 7830–7839 (2016).
34. Weidman, M. C., Yager, K. G. & Tisdale, W. A. Interparticle Spacing and Structural Ordering in Superlattice PbS Nanocrystal Solids Undergoing Ligand Exchange. *Chem. Mater.* **27**, 474–482 (2015).
35. Talapin, D. V. & Murray, C. B. PbSe Nanocrystal Solids for n- and p-Channel Thin Film Field-Effect Transistors. *Science* **310**, 86–89 (2005).
36. Dabbousi, B. O. *et al.* (CdSe)ZnS Core−Shell Quantum Dots: Synthesis and Characterization of a Size Series of Highly Luminescent Nanocrystallites. *J. Phys. Chem. B* **101**, 9463–9475 (1997).

37. Kim, S.-W. *et al.* Engineering InAsxP1-x/InP/ZnSe III−V Alloyed Core/Shell Quantum Dots for the Near-Infrared. *Journal of the American Chemical Society* **127**, 10526–10532 (2005).
38. Brust, M., Fink, J., Bethell, D., Schiffrin, D. J. & Kiely, C. Synthesis and reactions of functionalised gold nanoparticles. *J. Chem. Soc., Chem. Commun.* 1655–1656 (1995) doi:10.1039/C39950001655.
39. Fu, Y. H., Kuznetsov, A. I., Miroshnichenko, A. E., Yu, Y. F. & Luk'yanchuk, B. Directional visible light scattering by silicon nanoparticles. *Nat Commun* **4**, 1527 (2013).
40. Lee, J. H. QD Display: A Game-Changing Technology for the Display Industry. *Information Display* **36**, 9–13 (2020).
41. Winslow, S. W., Tisdale, W. A. & Swan, J. W. Prediction of PbS Nanocrystal Superlattice Structure with Large-Scale Patchy Particle Simulations. *J. Phys. Chem. C* **126**, 14264–14274 (2022).
42. Dussert, F. *et al.* Physico-Chemical Transformation and Toxicity of Multi-Shell InP Quantum Dots under Simulated Sunlight Irradiation, in an Environmentally Realistic Scenario. *Nanomaterials* **12**, 3703 (2022).
43. Kang, X. & Zhu, M. Metal Nanoclusters Stabilized by Selenol Ligands. *Small* **15**, 1902703 (2019).
44. Myong, M. S., Zhou, J., Young, R. M. & Wasielewski, M. R. Charge-Transfer Character in Excimers of Perylenediimides Self-Assembled on Anodic Aluminum Oxide Membrane Walls. *J. Phys. Chem. C* **124**, 4369–4377 (2020).
45. Khan, K. *et al.* Recent developments in emerging two-dimensional materials and their applications. *J. Mater. Chem. C* **8**, 387–440 (2020).
46. Das, S., Robinson, J. A., Dubey, M., Terrones, H. & Terrones, M. Beyond Graphene: Progress in Novel Two-Dimensional Materials and van der Waals Solids. *Annual Review of Materials Research* **45**, 1–27 (2015).
47. Gambetta, A. *et al.* Real-time observation of nonlinear coherent phonon dynamics in single-walled carbon nanotubes. *Nature Phys* **2**, 515–520 (2006).
48. Tice, D. B., Weinberg, D. J., Mathew, N., Chang, R. P. H. & Weiss, E. A. Measurement of Wavelength-Dependent Polarization Character in the Absorption Anisotropies of Ensembles of CdSe Nanorods. *J. Phys. Chem. C* **117**, 13289–13296 (2013).
49. Gao, Y., Weidman, M. C. & Tisdale, W. A. CdSe Nanoplatelet Films with Controlled Orientation of their Transition Dipole Moment. *Nano Lett.* **17**, 3837–3843 (2017).
50. Passarelli, J. V. *et al.* Tunable exciton binding energy in 2D hybrid layered perovskites through donor–acceptor interactions within the organic layer. *Nature Chemistry* **12**, 672–682 (2020).
51. Gutiérrez, H. R. *et al.* Extraordinary Room-Temperature Photoluminescence in Triangular WS2 Monolayers. *Nano Lett.* **13**, 3447–3454 (2013).
52. Poh, T. Y. *et al.* Inhaled nanomaterials and the respiratory microbiome: clinical, immunological and toxicological perspectives. *Particle and Fibre Toxicology* **15**, 46 (2018).

53. Novoselov, K. S. *et al.* Electric Field Effect in Atomically Thin Carbon Films. *Science* **306**, 666–669 (2004).
54. Cao, Y. *et al.* Unconventional superconductivity in magic-angle graphene superlattices. *Nature* **556**, 43–50 (2018).
55. Castro Neto, A. H., Guinea, F., Peres, N. M. R., Novoselov, K. S. & Geim, A. K. The electronic properties of graphene. *Rev. Mod. Phys.* **81**, 109–162 (2009).
56. Novoselov, K. S. *et al.* Two-dimensional atomic crystals. *PNAS* **102**, 10451–10453 (2005).
57. Goodman, A. J., Dahod, N. S. & Tisdale, W. A. Ultrafast Charge Transfer at a Quantum Dot/2D Materials Interface Probed by Second Harmonic Generation. *J. Phys. Chem. Lett.* **9**, 4227–4232 (2018).
58. Li, S.-L., Tsukagoshi, K., Orgiu, E. & Samorì, P. Charge transport and mobility engineering in two-dimensional transition metal chalcogenide semiconductors. *Chemical Society Reviews* **45**, 118–151 (2016).
59. Cai, Z., Liu, B., Zou, X. & Cheng, H.-M. Chemical Vapor Deposition Growth and Applications of Two-Dimensional Materials and Their Heterostructures. *Chem. Rev.* **118**, 6091–6133 (2018).
60. Bian, R. *et al.* Recent progress in the synthesis of novel two-dimensional van der Waals materials. *National Science Review* **9**, nwab164 (2022).
61. Wang, L. *et al.* One-Dimensional Electrical Contact to a Two-Dimensional Material. *Science* **342**, 614–617 (2013).
62. Liu, H. *et al.* Controllable Interlayer Charge and Energy Transfer in Perovskite Quantum Dots/ Transition Metal Dichalcogenide Heterostructures. *Advanced Materials Interfaces* **n/a**, 1901263 (2019).
63. Mao, L., Stoumpos, C. C. & Kanatzidis, M. G. Two-Dimensional Hybrid Halide Perovskites: Principles and Promises. *J. Am. Chem. Soc.* **141**, 1171–1190 (2019).
64. Wang, G.-E., Luo, S., Di, T., Fu, Z. & Xu, G. Layered Organic Metal Chalcogenides (OMCs): From Bulk to Two-Dimensional Materials. *Angewandte Chemie International Edition* **n/a**, e202203151 (2022).
65. Kojima, A., Teshima, K., Shirai, Y. & Miyasaka, T. Organometal Halide Perovskites as Visible-Light Sensitizers for Photovoltaic Cells. *J. Am. Chem. Soc.* **131**, 6050–6051 (2009).
66. Jeong, J. *et al.* Pseudo-halide anion engineering for α-FAPbI3 perovskite solar cells. *Nature* **592**, 381–385 (2021).
67. Krieg, F. *et al.* Colloidal CsPbX3 (X = Cl, Br, I) Nanocrystals 2.0: Zwitterionic Capping Ligands for Improved Durability and Stability. *ACS Energy Lett.* **3**, 641–646 (2018).
68. Kovalenko, M. V., Protesescu, L. & Bodnarchuk, M. I. Properties and potential optoelectronic applications of lead halide perovskite nanocrystals. *Science* **358**, 745–750 (2017).
69. Rehman, W. *et al.* Photovoltaic mixed-cation lead mixed-halide perovskites: links between crystallinity, photo-stability and electronic properties. *Energy Environ. Sci.* **10**, 361–369 (2017).

70. Li, Z. *et al.* Stabilizing Perovskite Structures by Tuning Tolerance Factor: Formation of Formamidinium and Cesium Lead Iodide Solid-State Alloys. *Chemistry of Materials* **28**, 284–292 (2016).
71. Manser, J. S., Christians, J. A. & Kamat, P. V. Intriguing Optoelectronic Properties of Metal Halide Perovskites. *Chem. Rev.* **116**, 12956–13008 (2016).
72. Kim, J., Lee, S.-H., Lee, J. H. & Hong, K.-H. The Role of Intrinsic Defects in Methylammonium Lead Iodide Perovskite. *J. Phys. Chem. Lett.* **5**, 1312–1317 (2014).
73. Walsh, A., Scanlon, D. O., Chen, S., Gong, X. G. & Wei, S.-H. Self-Regulation Mechanism for Charged Point Defects in Hybrid Halide Perovskites. *Angew Chem Int Ed Engl* **54**, 1791–1794 (2015).
74. Zhu, H. *et al.* Screening in crystalline liquids protects energetic carriers in hybrid perovskites. *Science* **353**, 1409–1413 (2016).
75. Stranks, S. D. *et al.* Electron-Hole Diffusion Lengths Exceeding 1 Micrometer in an Organometal Trihalide Perovskite Absorber. *Science* **342**, 341–344 (2013).
76. Dong, Q. *et al.* Electron-hole diffusion lengths > 175 μm in solution-grown CH3NH3PbI3 single crystals. *Science* **347**, 967–970 (2015).
77. Steirer, K. X. *et al.* Defect Tolerance in Methylammonium Lead Triiodide Perovskite. *ACS Energy Letters* **1**, 360–366 (2016).
78. Kambhampati, P. Learning about the Structural Dynamics of Semiconductor Perovskites from Electron Solvation Dynamics. *J. Phys. Chem. C* **125**, 23571–23586 (2021).
79. Zhu, X.-Y. & Podzorov, V. Charge Carriers in Hybrid Organic–Inorganic Lead Halide Perovskites Might Be Protected as Large Polarons. *J. Phys. Chem. Lett.* **6**, 4758–4761 (2015).
80. Chen, Z., Guo, Y., Wertz, E. & Shi, J. Merits and Challenges of Ruddlesden–Popper Soft Halide Perovskites in Electro-Optics and Optoelectronics. *Advanced Materials* **31**, 1803514 (2019).
81. Smith, I. C., Hoke, E. T., Solis-Ibarra, D., McGehee, M. D. & Karunadasa, H. I. A Layered Hybrid Perovskite Solar-Cell Absorber with Enhanced Moisture Stability. *Angewandte Chemie International Edition* **53**, 11232–11235 (2014).
82. Pan, J. *et al.* Air-Stable Surface-Passivated Perovskite Quantum Dots for Ultra-Robust, Single- and Two-Photon-Induced Amplified Spontaneous Emission. *The Journal of Physical Chemistry Letters* **6**, 5027–5033 (2015).
83. Cuthbert, H. L., Wallbank, A. I., Taylor, N. J. & Corrigan, J. F. Synthesis and Structural Characterization of [Cu20Se4(μ3-SePh)12(PPh3)6] and [Ag(SePh)]∞. *Zeitschrift für anorganische und allgemeine Chemie* **628**, 2483–2488 (2002).
84. Schriber, E. A. *et al.* Mithrene Is a Self-Assembling Robustly Blue Luminescent Metal–Organic Chalcogenolate Assembly for 2D Optoelectronic Applications. *ACS Appl. Nano Mater.* **1**, 3498–3508 (2018).
85. Yao, K. *et al.* Strongly Quantum-Confined Blue-Emitting Excitons in Chemically Configurable Multiquantum Wells. *ACS Nano* **15**, 4085–4092 (2021).
86. Maserati, L. *et al.* Anisotropic 2D excitons unveiled in organic–inorganic quantum wells. *Materials Horizons* **8**, 197–208 (2021).

87. Kastl, C., Schwartzberg, A. M. & Maserati, L. Picoseconds-Limited Exciton Recombination in Metal–Organic Chalcogenides Hybrid Quantum Wells. *ACS Nano* (2022) doi:10.1021/acsnano.1c07281.

88. Paritmongkol, W. *et al.* Size and Quality Enhancement of 2D Semiconducting Metal–Organic Chalcogenolates by Amine Addition. *J. Am. Chem. Soc.* **143**, 20256–20263 (2021).

89. Yeung, M. *et al.* Corrosion of Late- and Post-Transition Metals into Metal–Organic Chalcogenolates and Implications for Nanodevice Architectures. *ACS Appl. Nano Mater.* **3**, 3568–3577 (2020).

90. Trang, B. *et al.* Tarnishing Silver Metal into Mithrene. *J. Am. Chem. Soc.* **140**, 13892–13903 (2018).

91. Schriber, E. A., Rosenberg, D. J., Kelly, R. P., Ghodsi, A. & Hohman, J. N. Investigation of Nucleation and Growth at a Liquid–Liquid Interface by Solvent Exchange and Synchrotron Small-Angle X-Ray Scattering. *Frontiers in Chemistry* **9**, 429 (2021).

92. Popple, D. C., Schriber, E. A., Yeung, M. & Hohman, J. N. Competing Roles of Crystallization and Degradation of a Metal–Organic Chalcogenolate Assembly under Biphasic Solvothermal Conditions. *Langmuir* **34**, 14265–14273 (2018).

93. Maserati, L., Pecorario, S., Prato, M. & Caironi, M. Understanding the Synthetic Pathway to Large-Area, High-Quality [AgSePh]∞ Nanocrystal Films. *J. Phys. Chem. C* **124**, 22845–22852 (2020).

94. Paritmongkol, W. *et al.* Morphological Control of 2D Hybrid Organic–Inorganic Semiconductor AgSePh. *ACS Nano* **16**, 2054–2065 (2022).

95. Schriber, E. A. *et al.* Chemical crystallography by serial femtosecond X-ray diffraction. *Nature* **601**, 360–365 (2022).

96. Lee, W. S. *et al.* Light Emission in 2D Silver Phenylchalcogenolates. *ACS Nano* (2022) doi:10.1021/acsnano.2c06204.

97. Li, Y. *et al.* Coordination assembly of 2D ordered organic metal chalcogenides with widely tunable electronic band gaps. *Nature Communications* **11**, 1–9 (2020).

98. Han, Z. *et al.* Ultrastable atomically precise chiral silver clusters with more than 95% quantum efficiency. *Sci. Adv.* **6**, eaay0107 (2020).

99. Zhang, L. *et al.* High-performance quasi-2D perovskite light-emitting diodes: from materials to devices. *Light: Science & Applications* **10**, 61 (2021).

100. Jeong, T. Y. *et al.* Coherent Lattice Vibrations in Mono- and Few-Layer WSe2. *ACS Nano* **10**, 5560–5566 (2016).

101. Mauck, C. M. *et al.* Inorganic Cage Motion Dominates Excited-State Dynamics in 2D-Layered Perovskites (CxH2x+1NH3)2PbI4 (x = 4–9). *J. Phys. Chem. C* **123**, 27904–27916 (2019).

102. Thouin, F. *et al.* Phonon coherences reveal the polaronic character of excitons in two-dimensional lead halide perovskites. *Nat. Mater.* **18**, 349–356 (2019).

103. Rabouw, F. T. & de Mello Donega, C. Excited-State Dynamics in Colloidal Semiconductor Nanocrystals. *Top Curr Chem (Z)* **374**, 58 (2016).

104. Yaffe, O. *et al.* Excitons in ultrathin organic-inorganic perovskite crystals. *Phys. Rev. B* **92**, 045414 (2015).

105. Carey, G. H. *et al.* Materials processing strategies for colloidal quantum dot solar cells: advances, present-day limitations, and pathways to improvement. *MRS Communications* **3**, 83–90 (2013).
106. Yang, X. *et al.* Highly Flexible, Electrically Driven, Top-Emitting, Quantum Dot Light-Emitting Stickers. *ACS Nano* **8**, 8224–8231 (2014).
107. Silver, S., Yin, J., Li, H., Brédas, J.-L. & Kahn, A. Characterization of the Valence and Conduction Band Levels of n = 1 2D Perovskites: A Combined Experimental and Theoretical Investigation. *Advanced Energy Materials* **8**, 1703468 (2018).
108. Smith, M. D. *et al.* Decreasing the electronic confinement in layered perovskites through intercalation. *Chem. Sci.* **8**, 1960–1968 (2017).
109. Raja, A. *et al.* Coulomb engineering of the bandgap and excitons in two-dimensional materials. *Nature Communications* **8**, 15251 (2017).
110. Prins, F., Goodman, A. J. & Tisdale, W. A. Reduced Dielectric Screening and Enhanced Energy Transfer in Single- and Few-Layer MoS2. *Nano Lett.* **14**, 6087–6091 (2014).
111. Raja, A. *et al.* Energy Transfer from Quantum Dots to Graphene and MoS $_2$ : The Role of Absorption and Screening in Two-Dimensional Materials. *Nano Letters* **16**, 2328–2333 (2016).
112. Kittel, C. *Introduction to solid state physics*. (Wiley, 2005).
113. Liu, Y. *et al.* Dependence of Carrier Mobility on Nanocrystal Size and Ligand Length in PbSe Nanocrystal Solids. *Nano Letters* **10**, 1960–1969 (2010).
114. Gilmore, R. H., Lee, E. M. Y., Weidman, M. C., Willard, A. P. & Tisdale, W. A. Charge Carrier Hopping Dynamics in Homogeneously Broadened PbS Quantum Dot Solids. *Nano Lett.* **17**, 893–901 (2017).
115. DuBose, J. T. & Kamat, P. V. Energy Versus Electron Transfer: Managing Excited-State Interactions in Perovskite Nanocrystal–Molecular Hybrids. *Chem. Rev.* **122**, 12475–12494 (2022).
116. Mork, A. J., Weidman, M. C., Prins, F. & Tisdale, W. A. Magnitude of the Förster Radius in Colloidal Quantum Dot Solids. *The Journal of Physical Chemistry C* **118**, 13920–13928 (2014).
117. Zhou, N. *et al.* Distinguishing Energy- and Charge-Transfer Processes in Layered Perovskite Quantum Wells with Two-Dimensional Action Spectroscopies. *J. Phys. Chem. Lett.* **11**, 4570–4577 (2020).
118. Yazdani, N. *et al.* Tuning Electron–Phonon Interactions in Nanocrystals through Surface Termination. *Nano Lett.* **18**, 2233–2242 (2018).
119. Batignani, G. *et al.* Probing femtosecond lattice displacement upon photo-carrier generation in lead halide perovskite. *Nat Commun* **9**, 1971 (2018).
120. Miyata, K. *et al.* Large polarons in lead halide perovskites. *Science Advances* **3**, e1701217 (2017).
121. Paritmongkol, W., Powers, E. R., Dahod, N. S. & Tisdale, W. A. Two Origins of Broadband Emission in Multilayered 2D Lead Iodide Perovskites. *J. Phys. Chem. Lett.* **11**, 8565–8572 (2020).

122. The Nobel Prize in Chemistry 1967. *NobelPrize.org* https://www.nobelprize.org/prizes/chemistry/1967/ceremony-speech/.
123. Berera, R., van Grondelle, R. & Kennis, J. T. M. Ultrafast transient absorption spectroscopy: principles and application to photosynthetic systems. *Photosynth Res* **101**, 105–118 (2009).
124. Maiuri, M., Garavelli, M. & Cerullo, G. Ultrafast Spectroscopy: State of the Art and Open Challenges. *J. Am. Chem. Soc.* **142**, 3–15 (2020).
125. Krausz, F. From femtochemistry to attophysics. *Phys. World* **14**, 41–46 (2001).
126. Ruhman, S., Joly, A. G. & Nelson, K. A. Time-resolved observations of coherent molecular vibrational motion and the general occurrence of impulsive stimulated scattering. *The Journal of Chemical Physics* **86**, 6563–6565 (1987).
127. Polli, D., Lüer, L. & Cerullo, G. High-time-resolution pump-probe system with broadband detection for the study of time-domain vibrational dynamics. *Review of Scientific Instruments* **78**, 103108 (2007).
128. Liebel, M., Schnedermann, C., Wende, T. & Kukura, P. Principles and Applications of Broadband Impulsive Vibrational Spectroscopy. *J. Phys. Chem. A* **119**, 9506–9517 (2015).
129. Pandya, R. *et al.* Exciton–Phonon Interactions Govern Charge-Transfer-State Dynamics in CdSe/CdTe Two-Dimensional Colloidal Heterostructures. *J. Am. Chem. Soc.* **140**, 14097–14111 (2018).
130. Bionta, M. R. *et al.* On-chip sampling of optical fields with attosecond resolution. *Nat. Photonics* **15**, 456–460 (2021).
131. Li, J. *et al.* Attosecond science based on high harmonic generation from gases and solids. *Nat Commun* **11**, 2748 (2020).
132. Prince, R. C., Frontiera, R. R. & Potma, E. O. Stimulated Raman Scattering: From Bulk to Nano. *Chem. Rev.* **117**, 5070–5094 (2017).
133. Hentschel, M. *et al.* Attosecond metrology. *Nature* **414**, 509–513 (2001).
134. Klimov, V. I. Optical Nonlinearities and Ultrafast Carrier Dynamics in Semiconductor Nanocrystals. *J. Phys. Chem. B* **104**, 6112–6123 (2000).
135. Tisdale, W. A. *et al.* Hot-Electron Transfer from Semiconductor Nanocrystals. *Science* **328**, 1543–1547 (2010).
136. Mannebach, E. M. *et al.* Ultrafast Electronic and Structural Response of Monolayer MoS2 under Intense Photoexcitation Conditions. *ACS Nano* **8**, 10734–10742 (2014).
137. Kukura, P., McCamant, D. W. & Mathies, R. A. Femtosecond Stimulated Raman Spectroscopy. *Annual Review of Physical Chemistry* **58**, 461–488 (2007).
138. Ashner, M. N. & Tisdale, W. A. High repetition-rate femtosecond stimulated Raman spectroscopy with fast acquisition. *Opt. Express, OE* **26**, 18331–18340 (2018).
139. Li, S., Li, Y., Yi, R., Liu, L. & Qu, J. Coherent Anti-Stokes Raman Scattering Microscopy and Its Applications. *Frontiers in Physics* **8**, (2020).
140. Dhar, L., Rogers, J. A. & Nelson, K. A. Time-resolved vibrational spectroscopy in the impulsive limit. *Chem. Rev.* **94**, 157–193 (1994).

141. De Silvestri, S., Cerullo, G. & Lanzani, G. *Coherent vibrational dynamics*. (CRC Press, 2008).
142. Polli, D., Brida, D., Mukamel, S., Lanzani, G. & Cerullo, G. Effective temporal resolution in pump-probe spectroscopy with strongly chirped pulses. *Phys. Rev. A* **82**, 053809 (2010).
143. Bradler, M., Baum, P. & Riedle, E. Femtosecond continuum generation in bulk laser host materials with sub-μJ pump pulses. *Appl. Phys. B* **97**, 561–574 (2009).
144. Calendron, A.-L., Çankaya, H., Cirmi, G. & Kärtner, F. X. White-light generation with sub-ps pulses. *Opt. Express* **23**, 13866 (2015).
145. Dubietis, A., Tamošauskas, G., Šuminas, R., Jukna, V. & Couairon, A. Ultrafast supercontinuum generation in bulk condensed media. *Lith. J. Phys.* **57**, (2017).
146. Dharmadhikari, A. K., Rajgara, F. A. & Mathur, D. Systematic study of highly efficient white light generation in transparent materials using intense femtosecond laser pulses. *Appl. Phys. B* **80**, 61–66 (2005).
147. Huber, L., Maehrlein, S. F., Wang, F., Liu, Y. & Zhu, X.-Y. The ultrafast Kerr effect in anisotropic and dispersive media. *J. Chem. Phys.* **154**, 094202 (2021).
148. Cerullo, G. & De Silvestri, S. Ultrafast optical parametric amplifiers. *Review of Scientific Instruments* **74**, 1–18 (2003).
149. Wilson, K. & McCamant, D. W. *Guide to NOPAs*. (http://www.sas.rochester.edu/chm/groups/mccamant/assets/pdf/documents_nopa.pdf).
150. Fork, R. L., Martinez, O. E. & Gordon, J. P. Negative dispersion using pairs of prisms. *Opt. Lett.* **9**, 150 (1984).
151. Szipöcs, R., Ferencz, K., Spielmann, C. & Krausz, F. Chirped multilayer coatings for broadband dispersion control in femtosecond lasers. *Opt. Lett., OL* **19**, 201–203 (1994).
152. Kane, D. J., Weston, J. & Chu, K.-C. J. Real-time inversion of polarization gate frequency-resolved optical gating spectrograms. *Appl. Opt.* **42**, 1140 (2003).
153. Jafari, R. & Trebino, R. High-speed "multi-grid" pulse-retrieval algorithm for frequency-resolved optical gating. *Optics Express* **26**, 2643–2649 (2018).
154. Trebino, R. *Frequency-Resolved Optical Gating: The Measurement of Ultrashort Laser Pulses*. (Springer US, 2000). doi:10.1007/978-1-4615-1181-6.
155. Trebino, R. FROG Algorithm. https://frog.gatech.edu/code.html.
156. Rivett, J. P. H. *et al.* Long-lived polarization memory in the electronic states of lead-halide perovskites from local structural dynamics. *Nature Communications* **9**, 3531 (2018).
157. Zhang, B. *et al.* Polarization-dependent exciton dynamics in tetracene single crystals. *J. Chem. Phys.* **141**, 244303 (2014).
158. Tan, H.-S., Piletic, I. R. & Fayer, M. D. Polarization selective spectroscopy experiments: methodology and pitfalls. *J. Opt. Soc. Am. B* **22**, 2009 (2005).
159. Ashner, M. N. *et al.* Size-Dependent Biexciton Spectrum in $CsPbBr_3$ Perovskite Nanocrystals. *ACS Energy Lett.* **4**, 2639–2645 (2019).
160. Viswanathan, B. *Nano materials*. (Alpha Science International, 2009).
161. Furukawa, H., Cordova, K. E., O'Keeffe, M. & Yaghi, O. M. The Chemistry and Applications of Metal-Organic Frameworks. *Science* **341**, 1230444 (2013).

162. Sanchez, C., Belleville, P., Popall, M. & Nicole, L. Applications of advanced hybrid organic–inorganic nanomaterials: from laboratory to market. *Chem. Soc. Rev.* **40**, 696–753 (2011).

163. Saparov, B. & Mitzi, D. B. Organic–Inorganic Perovskites: Structural Versatility for Functional Materials Design. *Chem. Rev.* **116**, 4558–4596 (2016).

164. Stranks, S. D. & Snaith, H. J. Metal-halide perovskites for photovoltaic and light-emitting devices. *Nature Nanotech* **10**, 391–402 (2015).

165. Jena, A. K., Kulkarni, A. & Miyasaka, T. Halide Perovskite Photovoltaics: Background, Status, and Future Prospects. *Chem. Rev.* **119**, 3036–3103 (2019).

166. Wang, F. *et al.* Solvated Electrons in Solids—Ferroelectric Large Polarons in Lead Halide Perovskites. *J. Am. Chem. Soc.* **143**, 5–16 (2021).

167. Park, Y., Obliger, A. & Limmer, D. T. Nonlocal Screening Dictates the Radiative Lifetimes of Excitations in Lead Halide Perovskites. *Nano Lett.* (2022) doi:10.1021/acs.nanolett.2c00077.

168. Park, M. *et al.* Excited-state vibrational dynamics toward the polaron in methylammonium lead iodide perovskite. *Nature Communications* **9**, 1–9 (2018).

169. Guo, Y. *et al.* Dynamic emission Stokes shift and liquid-like dielectric solvation of band edge carriers in lead-halide perovskites. *Nat Commun* **10**, 1175 (2019).

170. Mauck, C. M. & Tisdale, W. A. Excitons in 2D Organic–Inorganic Halide Perovskites. *Trends in Chemistry* **1**, 380–393 (2019).

171. Blancon, J.-C., Even, J., Stoumpos, C. C., Kanatzidis, M. G. & Mohite, A. D. Semiconductor physics of organic–inorganic 2D halide perovskites. *Nat. Nanotechnol.* **15**, 969–985 (2020).

172. Ni, L. *et al.* Real-Time Observation of Exciton–Phonon Coupling Dynamics in Self-Assembled Hybrid Perovskite Quantum Wells. *ACS Nano* **11**, 10834–10843 (2017).

173. Fu, J. *et al.* Electronic States Modulation by Coherent Optical Phonons in 2D Halide Perovskites. *Advanced Materials* **33**, 2006233 (2021).

174. Veselska, O. & Demessence, A. d10 coinage metal organic chalcogenolates: From oligomers to coordination polymers. *Coordination Chemistry Reviews* **355**, 240–270 (2018).

175. Lavenn, C. *et al.* Shedding light on an ultra-bright photoluminescent lamellar gold thiolate coordination polymer [Au( p -SPhCO 2 Me)] n. *Chemical Communications* **52**, 9063–9066 (2016).

176. Ma, L. *et al.* A new Cu–cysteamine complex: structure and optical properties. *J. Mater. Chem. C* **2**, 4239–4246 (2014).

177. Veselska, O. *et al.* New Lamellar Silver Thiolate Coordination Polymers with Tunable Photoluminescence Energies by Metal Substitution. *Inorg. Chem.* **58**, 99–105 (2019).

178. Xing, G., Li, Y., Feng, Z., Singh, D. J. & Pauly, F. Copper(I)-Based Flexible Organic–Inorganic Coordination Polymer and Analogues: High-Power Factor Thermoelectrics. *ACS Appl. Mater. Interfaces* **12**, 53841–53851 (2020).

179. Yang, A.-N., Lin, J. T. & Li, C.-T. Electroactive and Sustainable Cu-MOF/PEDOT Composite Electrocatalysts for Multiple Redox Mediators and for High-Performance Dye-Sensitized Solar Cells. *ACS Appl. Mater. Interfaces* **13**, 8435–8444 (2021).
180. Maserati, L. *et al.* Photo-electrical properties of 2D quantum confined metal–organic chalcogenide nanocrystal films. *Nanoscale* **13**, 233–241 (2021).
181. Huang, Q.-Q. *et al.* Single-Component MLCT-Active Photodetecting Material Based on a Two-Dimensional Coordination Polymer. *CCS Chemistry* **2**, 655–662 (2019).
182. Jiang, H. *et al.* Organic "receptor" fully covered few-layer organic–metal chalcogenides for high-performance chemiresistive gas sensing at room temperature. *Chem. Commun.* **56**, 5366–5369 (2020).
183. Veselska, O., Podbevšek, D., Ledoux, G., Fateeva, A. & Demessence, A. Intrinsic triple-emitting 2D copper thiolate coordination polymer as a ratiometric thermometer working over 400 K range. *Chem. Commun.* **53**, 12225–12228 (2017).
184. Schmidbaur, H. & Schier, A. Argentophilic Interactions. *Angewandte Chemie International Edition* **54**, 746–784 (2015).
185. Yan, Y. J. & Mukamel, S. Femtosecond pump-probe spectroscopy of polyatomic molecules in condensed phases. *Phys. Rev. A* **41**, 6485–6504 (1990).
186. Yu, P. Y. & Cardona, M. *Fundamentals of semiconductors: physics and materials properties*. (Springer, 2010).
187. Guo, Z., Wu, X., Zhu, T., Zhu, X. & Huang, L. Electron–Phonon Scattering in Atomically Thin 2D Perovskites. *ACS Nano* **10**, 9992–9998 (2016).
188. Matsumoto, Y. & Watanabe, K. Coherent Vibrations of Adsorbates Induced by Femtosecond Laser Excitation. *Chem. Rev.* **106**, 4234–4260 (2006).
189. Kuramochi, H. & Tahara, T. Tracking Ultrafast Structural Dynamics by Time-Domain Raman Spectroscopy. *J. Am. Chem. Soc.* **143**, 9699–9717 (2021).
190. Kamali, K. *et al.* Anharmonic phonons of NaZr 2 (PO 4 ) 3 studied by Raman spectroscopy, first-principles calculations, and x-ray diffraction. *Phys. Rev. B* **86**, 144301 (2012).
191. Kaasbjerg, K., Thygesen, K. S. & Jacobsen, K. W. Phonon-limited mobility in n-type single-layer MoS2 from first principles. *Phys. Rev. B* **85**, 115317 (2012).
192. Fivaz, R. & Mooser, E. Mobility of Charge Carriers in Semiconducting Layer Structures. *Phys. Rev.* **163**, 743–755 (1967).
193. Pelant, I. & Valenta, J. *Luminescence spectroscopy of semiconductors*. (Oxford University Press, 2012).
194. Bhosale, J. *et al.* Temperature dependence of band gaps in semiconductors: Electron-phonon interaction. *Phys. Rev. B* **86**, 195208 (2012).
195. Yu, C. *et al.* Temperature dependence of the band gap of perovskite semiconductor compound CsSnI3. *Journal of Applied Physics* **110**, 063526 (2011).
196. Wright, A. D. *et al.* Electron–phonon coupling in hybrid lead halide perovskites. *Nat Commun* **7**, 11755 (2016).
197. Lee, J., Koteles, E. S. & Vassell, M. O. Luminescence linewidths of excitons in GaAs quantum wells below 150 K. *Phys. Rev. B* **33**, 5512–5516 (1986).

198. Rudin, S. & Reinecke, T. L. Temperature-dependent exciton linewidths in semiconductor quantum wells. *Phys. Rev. B* **41**, 3017–3027 (1990).

199. Porezag, D. & Pederson, M. R. Infrared intensities and Raman-scattering activities within density-functional theory. *Phys. Rev. B* **54**, 7830–7836 (1996).

200. Rojas-Gatjens, E., Silva-Acuña, C. & Kandada, A. R. S. Peculiar anharmonicity of Ruddlesden Popper metal halides: temperature-dependent phonon dephasing. *Mater. Horiz.* **9**, 492–499 (2022).

201. Vallée, F. Time-resolved investigation of coherent LO-phonon relaxation in III-V semiconductors. *Phys. Rev. B* **49**, 2460–2468 (1994).

202. Ferraro, J. R., Nakamoto, K. & Brown, C. W. *Introductory Raman spectroscopy*. (Academic Press, 2003).

203. Hase, M., Ushida, K. & Kitajima, M. Anharmonic Decay of Coherent Optical Phonons in Antimony. *J. Phys. Soc. Jpn.* **84**, 024708 (2015).

204. Hase, M., Mizoguchi, K., Harima, H., Nakashima, S. & Sakai, K. Dynamics of coherent phonons in bismuth generated by ultrashort laser pulses. *Phys. Rev. B* **58**, 5448–5452 (1998).

205. Hart, T. R., Aggarwal, R. L. & Lax, B. Temperature Dependence of Raman Scattering in Silicon. *Phys. Rev. B* **1**, 638–642 (1970).

206. Freitas Neto, E. S. *et al.* Temperature-dependent Raman study of thermal parameters in CdS quantum dots. *Nanotechnology* **23**, 125701 (2012).

207. Häfner, W. & Kiefer, W. Raman spectroscopic investigations on molecular crystals: Pressure and temperature dependence of external phonons in naphthalene- $d_8$ and anthracene- $d_{10}$. *The Journal of Chemical Physics* **86**, 4582–4596 (1987).

208. Gong, X. *et al.* Electron–phonon interaction in efficient perovskite blue emitters. *Nature Mater* **17**, 550–556 (2018).

209. Kubelka, P. & Munk, F. An Article on Optics of Paint Layers. *Z. Techn. Physik.* **12**, 593–601 (1931).

210. Kresse, G. & Furthmüller, J. Efficient iterative schemes for ab initio total-energy calculations using a plane-wave basis set. *Physical review B* **54**, 11169 (1996).

211. Kresse, G. & Furthmüller, J. Efficiency of ab-initio total energy calculations for metals and semiconductors using a plane-wave basis set. *Computational materials science* **6**, 15–50 (1996).

212. Kresse, G. & Hafner, J. Ab initio molecular dynamics for liquid metals. *Physical review B* **47**, 558 (1993).

213. Kresse, G. & Hafner, J. Ab initio molecular-dynamics simulation of the liquid-metal–amorphous-semiconductor transition in germanium. *Physical Review B* **49**, 14251 (1994).

214. Blöchl, P. E. Projector augmented-wave method. *Physical review B* **50**, 17953 (1994).

215. Kresse, G. & Joubert, D. From ultrasoft pseudopotentials to the projector augmented-wave method. *Physical review b* **59**, 1758 (1999).

216. Perdew, J. P., Burke, K. & Ernzerhof, M. Generalized gradient approximation made simple. *Physical review letters* **77**, 3865 (1996).

217. Togo, A. & Tanaka, I. First principles phonon calculations in materials science. *Scripta Materialia* **108**, 1–5 (2015).

218. Wu, X., Vanderbilt, D. & Hamann, D. R. Systematic treatment of displacements, strains, and electric fields in density-functional perturbation theory. *Phys. Rev. B* **72**, 035105 (2005).

219. Karhánek, D., Bučko, T. & Hafner, J. A density-functional study of the adsorption of methane-thiol on the (111) surfaces of the Ni-group metals: II. Vibrational spectroscopy. *J. Phys.: Condens. Matter* **22**, 265006 (2010).

220. Skelton, J. M. *et al.* Lattice dynamics of the tin sulphides $SnS_2$, SnS and $Sn_2S_3$: vibrational spectra and thermal transport. *Phys. Chem. Chem. Phys.* **19**, 12452–12465 (2017).

221. Gajdoš, M., Hummer, K., Kresse, G., Furthmüller, J. & Bechstedt, F. Linear optical properties in the projector-augmented wave methodology. *Physical Review B* **73**, 045112 (2006).

222. Gonze, X. & Lee, C. Dynamical matrices, Born effective charges, dielectric permittivity tensors, and interatomic force constants from density-functional perturbation theory. *Physical Review B* **55**, 10355 (1997).

223. Dal Corso, A., Baroni, S. & Resta, R. Density-functional theory of the dielectric constant: Gradient-corrected calculation for silicon. *Physical Review B* **49**, 5323 (1994).

224. Humphrey, W., Dalke, A. & Schulten, K. VMD: visual molecular dynamics. *Journal of molecular graphics* **14**, 33–38 (1996).

225. Gygi, F. Architecture of Qbox: A scalable first-principles molecular dynamics code. *IBM Journal of Research and Development* **52**, 137–144 (2008).

226. Harris, F. J. On the use of windows for harmonic analysis with the discrete Fourier transform. *Proc. IEEE* **66**, 51–83 (1978).

227. Swart, M., van der Wijst, T., Fonseca Guerra, C. & Bickelhaupt, F. M. π-π stacking tackled with density functional theory. *J Mol Model* **13**, 1245–1257 (2007).

228. Kamat, P. V. & Biegel, C. M. Perovskite Stories from Around the World. *ACS Energy Lett.* **4**, 879–887 (2019).

229. Rossetti, R., Ellison, J. L., Gibson, J. M. & Brus, L. E. Size effects in the excited electronic states of small colloidal CdS crystallites. *The Journal of Chemical Physics* **80**, 4464–4469 (1984).

230. Alivisatos, A. P. Semiconductor Clusters, Nanocrystals, and Quantum Dots. *Science* **271**, 933–937 (1996).

231. Hines, M. A. & Guyot-Sionnest, P. Synthesis and Characterization of Strongly Luminescing ZnS-Capped CdSe Nanocrystals. *J. Phys. Chem.* **100**, 468–471 (1996).

232. Hanifi, D. A. *et al.* Redefining near-unity luminescence in quantum dots with photothermal threshold quantum yield. *Science* **363**, 1199–1202 (2019).

233. Sun, Q. *et al.* Bright, multicoloured light-emitting diodes based on quantum dots. *Nature Photon* **1**, 717–722 (2007).

234. Chiba, T. *et al.* Anion-exchange red perovskite quantum dots with ammonium iodine salts for highly efficient light-emitting devices. *Nature Photonics* **12**, 681–687 (2018).

235. Dong, Y. *et al.* Bipolar-shell resurfacing for blue LEDs based on strongly confined perovskite quantum dots. *Nature Nanotechnology* **15**, 668–674 (2020).

236. Kim, Y.-H. *et al.* Comprehensive defect suppression in perovskite nanocrystals for high-efficiency light-emitting diodes. *Nature Photonics* **15**, 148–155 (2021).

237. Nozik, A. J. Quantum dot solar cells. *Physica E: Low-dimensional Systems and Nanostructures* **14**, 115–120 (2002).

238. Yang, H., Zhang, Y., Hills-Kimball, K., Zhou, Y. & Chen, O. Building bridges between halide perovskite nanocrystals and thin-film solar cells. *Sustainable Energy Fuels* **2**, 2381–2397 (2018).

239. Utzat, H. *et al.* Coherent single-photon emission from colloidal lead halide perovskite quantum dots. *Science* **363**, 1068–1072 (2019).

240. Schmidt, L. C. *et al.* Nontemplate Synthesis of $CH_3NH_3PbBr_3$ Perovskite Nanoparticles. *Journal of the American Chemical Society* **136**, 850–853 (2014).

241. Walsh, A., Scanlon, D. O., Chen, S., Gong, X. G. & Wei, S.-H. Self-Regulation Mechanism for Charged Point Defects in Hybrid Halide Perovskites. *Angewandte Chemie International Edition* **54**, 1791–1794 (2015).

242. Rainò, G. *et al.* Single Cesium Lead Halide Perovskite Nanocrystals at Low Temperature: Fast Single-Photon Emission, Reduced Blinking, and Exciton Fine Structure. *ACS Nano* **10**, 2485–2490 (2016).

243. Becker, M. A. *et al.* Bright triplet excitons in caesium lead halide perovskites. *Nature* **553**, 189–193 (2018).

244. Park, Y.-S., Guo, S., Makarov, N. S. & Klimov, V. I. Room Temperature Single-Photon Emission from Individual Perovskite Quantum Dots. *ACS Nano* **9**, 10386–10393 (2015).

245. Yuan, G., Gómez, D. E., Kirkwood, N., Boldt, K. & Mulvaney, P. Two Mechanisms Determine Quantum Dot Blinking. *ACS Nano* **12**, 3397–3405 (2018).

246. Rabouw, F. T. *et al.* Delayed Exciton Emission and Its Relation to Blinking in CdSe Quantum Dots. *Nano Lett.* **15**, 7718–7725 (2015).

247. Sher, P. H. *et al.* Power law carrier dynamics in semiconductor nanocrystals at nanosecond timescales. *Appl. Phys. Lett.* **92**, 101111 (2008).

248. Tachiya, M. & Seki, K. Unified explanation of the fluorescence decay and blinking characteristics of semiconductor nanocrystals. *Appl. Phys. Lett.* **94**, 081104 (2009).

249. Verberk, R., van Oijen, A. M. & Orrit, M. Simple model for the power-law blinking of single semiconductor nanocrystals. *Phys. Rev. B* **66**, 233202 (2002).

250. Ye, M. & Searson, P. C. Blinking in quantum dots: The origin of the grey state and power law statistics. *Phys. Rev. B* **84**, 125317 (2011).

251. Hu, F. *et al.* Slow Auger Recombination of Charged Excitons in Nonblinking Perovskite Nanocrystals without Spectral Diffusion. *Nano Lett.* **16**, 6425–6430 (2016).

252. Becker, M. A. *et al.* Unraveling the Origin of the Long Fluorescence Decay Component of Cesium Lead Halide Perovskite Nanocrystals. *ACS Nano* **14**, 14939–14946 (2020).

253. Swarnkar, A. *et al.* Colloidal CsPbBr3 Perovskite Nanocrystals: Luminescence beyond Traditional Quantum Dots. *Angewandte Chemie International Edition* **54**, 15424–15428 (2015).

254. Galland, C. *et al.* Two types of luminescence blinking revealed by spectroelectrochemistry of single quantum dots. *Nature* **479**, 203–207 (2011).

255. Yarita, N. *et al.* Impact of Postsynthetic Surface Modification on Photoluminescence Intermittency in Formamidinium Lead Bromide Perovskite Nanocrystals. *J. Phys. Chem. Lett.* **8**, 6041–6047 (2017).

256. Yuan, G. *et al.* The Degradation and Blinking of Single $CsPbI_3$ Perovskite Quantum Dots. *J. Phys. Chem. C* **122**, 13407–13415 (2018).

257. Jones, M., Lo, S. S. & Scholes, G. D. Quantitative modeling of the role of surface traps in CdSe/CdS/ZnS nanocrystal photoluminescence decay dynamics. *Proceedings of the National Academy of Sciences* **106**, 3011–3016 (2009).

258. Issac, A., von Borczyskowski, C. & Cichos, F. Correlation between photoluminescence intermittency of CdSe quantum dots and self-trapped states in dielectric media. *Phys. Rev. B* **71**, 161302 (2005).

259. Nelson, C. A. & Zhu, X.-Y. Reversible Surface Electronic Traps in PbS Quantum Dot Solids Induced by an Order–Disorder Phase Transition in Capping Molecules. *J. Am. Chem. Soc.* **134**, 7592–7595 (2012).

260. Efros, Al. L. & Rosen, M. Random Telegraph Signal in the Photoluminescence Intensity of a Single Quantum Dot. *Phys. Rev. Lett.* **78**, 1110–1113 (1997).

261. Cordones, A. A. & Leone, S. R. Mechanisms for charge trapping in single semiconductor nanocrystals probed by fluorescence blinking. *Chem. Soc. Rev.* **42**, 3209–3221 (2013).

262. Shcherbakov-Wu, W., Sercel, P. C., Krieg, F., Kovalenko, M. V. & Tisdale, W. A. Temperature-Independent Dielectric Constant in CsPbBr3 Nanocrystals Revealed by Linear Absorption Spectroscopy. *J. Phys. Chem. Lett.* **12**, 8088–8095 (2021).

263. Yarita, N. *et al.* Dynamics of Charged Excitons and Biexcitons in $CsPbBr_3$ Perovskite Nanocrystals Revealed by Femtosecond Transient-Absorption and Single-Dot Luminescence Spectroscopy. *The Journal of Physical Chemistry Letters* **8**, 1413–1418 (2017).

264. Nakahara, S. *et al.* Ionization and Neutralization Dynamics of CsPbBr3 Perovskite Nanocrystals Revealed by Double-Pump Transient Absorption Spectroscopy. *J. Phys. Chem. Lett.* **10**, 4731–4736 (2019).

265. Canneson, D. *et al.* Negatively Charged and Dark Excitons in CsPbBr3 Perovskite Nanocrystals Revealed by High Magnetic Fields. *Nano Lett.* **17**, 6177–6183 (2017).

266. Hou, L. *et al.* Memories in the photoluminescence intermittency of single cesium lead bromide nanocrystals. *Nanoscale* **12**, 6795–6802 (2020).

267. Li, B. *et al.* Excitons and Biexciton Dynamics in Single $CsPbBr_3$ Perovskite Quantum Dots. *The Journal of Physical Chemistry Letters* **9**, 6934–6940 (2018).

268. Seth, S., Mondal, N., Patra, S. & Samanta, A. Fluorescence Blinking and Photoactivation of All-Inorganic Perovskite Nanocrystals CsPbBr3 and CsPbBr2I. *J. Phys. Chem. Lett.* **7**, 266–271 (2016).

269. Justo, Y. *et al.* Optical Properties of PbS/CdS Core/Shell Quantum Dots. *J. Phys. Chem. C* **117**, 20171–20177 (2013).

270. Aneesh, J. *et al.* Ultrafast Exciton Dynamics in Colloidal $CsPbBr_3$ Perovskite Nanocrystals: Biexciton Effect and Auger Recombination. *J. Phys. Chem. C* **121**, 4734–4739 (2017).

271. Nakahara, S. *et al.* Suppression of Trion Formation in $CsPbBr_3$ Perovskite Nanocrystals by Postsynthetic Surface Modification. *J. Phys. Chem. C* **122**, 22188–22193 (2018).

272. Stewart, J. T. *et al.* Comparison of Carrier Multiplication Yields in PbS and PbSe Nanocrystals: The Role of Competing Energy-Loss Processes. *Nano Lett.* **12**, 622–628 (2012).

273. Sun, H. *et al.* Biexciton and trion dynamics in InP/ZnSe/ZnS quantum dots. *J. Chem. Phys.* **156**, 054703 (2022).

274. Klimov, V. I., Mikhailovsky, A. A., McBranch, D. W., Leatherdale, C. A. & Bawendi, M. G. Quantization of Multiparticle Auger Rates in Semiconductor Quantum Dots. *Science* **287**, 1011–1013 (2000).

275. Makarov, N. S. *et al.* Spectral and Dynamical Properties of Single Excitons, Biexcitons, and Trions in Cesium–Lead-Halide Perovskite Quantum Dots. *Nano Lett.* **16**, 2349–2362 (2016).

276. Appavoo, K. *et al.* Ultrafast optical snapshots of hybrid perovskites reveal the origin of multiband electronic transitions. *Phys. Rev. B* **96**, 195308 (2017).

277. Kirschner, M. S. *et al.* Photoinduced, reversible phase transitions in all-inorganic perovskite nanocrystals. *Nature Communications* **10**, 1–8 (2019).

278. Voznyy, O., Thon, S. M., Ip, A. H. & Sargent, E. H. Dynamic Trap Formation and Elimination in Colloidal Quantum Dots. *J. Phys. Chem. Lett.* **4**, 987–992 (2013).

279. Issac, A., Krasselt, C., Cichos, F. & Borczyskowski, C. von. Influence of the Dielectric Environment on the Photoluminescence Intermittency of CdSe Quantum Dots. *ChemPhysChem* **13**, 3223–3230 (2012).

280. Shulenberger, K. E., Keller, H. R., Pellows, L. M., Brown, N. L. & Dukovic, G. Photocharging of Colloidal CdS Nanocrystals. *J. Phys. Chem. C* (2021) doi:10.1021/acs.jpcc.1c06491.

281. Tachikawa, T., Karimata, I. & Kobori, Y. Surface Charge Trapping in Organolead Halide Perovskites Explored by Single-Particle Photoluminescence Imaging. *J. Phys. Chem. Lett.* **6**, 3195–3201 (2015).

282. Nenon, D. P. *et al.* Design Principles for Trap-Free $CsPbX_3$ Nanocrystals: Enumerating and Eliminating Surface Halide Vacancies with Softer Lewis Bases. *J. Am. Chem. Soc.* **140**, 17760–17772 (2018).

283. Koscher, B. A., Swabeck, J. K., Bronstein, N. D. & Alivisatos, A. P. Essentially Trap-Free $CsPbBr_3$ Colloidal Nanocrystals by Postsynthetic Thiocyanate Surface Treatment. *J. Am. Chem. Soc.* **139**, 6566–6569 (2017).

284. Lee, J.-W., Kim, S.-G., Yang, J.-M., Yang, Y. & Park, N.-G. Verification and mitigation of ion migration in perovskite solar cells. *APL Materials* **7**, 041111 (2019).

285. Akriti *et al.* Layer-by-layer anionic diffusion in two-dimensional halide perovskite vertical heterostructures. *Nature Nanotechnology* 1–8 (2021) doi:10.1038/s41565-021-00848-w.

286. du Fossé, I., Boehme, S. C., Infante, I. & Houtepen, A. J. Dynamic Formation of Metal-Based Traps in Photoexcited Colloidal Quantum Dots and Their Relevance for Photoluminescence. *Chem. Mater.* **33**, 3349–3358 (2021).

287. Mooney, J., Krause, M. M., Saari, J. I. & Kambhampati, P. Challenge to the deep-trap model of the surface in semiconductor nanocrystals. *Phys. Rev. B* **87**, 081201 (2013).

288. Efros, A. L. & Nesbitt, D. J. Origin and control of blinking in quantum dots. *Nature Nanotech* **11**, 661–671 (2016).

289. Peterson, J. J. & Nesbitt, D. J. Modified Power Law Behavior in Quantum Dot Blinking: A Novel Role for Biexcitons and Auger Ionization. *Nano Lett.* **9**, 338–345 (2009).

290. Deschler, F. *et al.* High Photoluminescence Efficiency and Optically Pumped Lasing in Solution-Processed Mixed Halide Perovskite Semiconductors. *J. Phys. Chem. Lett.* **5**, 1421–1426 (2014).

291. Stranks, S. D. *et al.* Recombination Kinetics in Organic-Inorganic Perovskites: Excitons, Free Charge, and Subgap States. *Phys. Rev. Applied* **2**, 034007 (2014).

292. Maes, J. *et al.* Light Absorption Coefficient of CsPbBr 3 Perovskite Nanocrystals. *The Journal of Physical Chemistry Letters* **9**, 3093–3097 (2018).

293. Abbott, E. A. *Flatland: a romance of many dimensions*. (Dover Publications, 1992).

294. Williams, R. T. & Song, K. S. The self-trapped exciton. *Journal of Physics and Chemistry of Solids* **51**, 679–716 (1990).

295. Hu, T. *et al.* Mechanism for Broadband White-Light Emission from Two-Dimensional (110) Hybrid Perovskites. *J. Phys. Chem. Lett.* **7**, 2258–2263 (2016).

296. Smith, M. D., Jaffe, A., Dohner, E. R., Lindenberg, A. M. & Karunadasa, H. I. Structural origins of broadband emission from layered Pb–Br hybrid perovskites. *Chem. Sci.* **8**, 4497–4504 (2017).

297. Gong, C. *et al.* Band alignment of two-dimensional transition metal dichalcogenides: Application in tunnel field effect transistors. *Applied Physics Letters* **103**, 053513 (2013).

298. Kang, J., Tongay, S., Zhou, J., Li, J. & Wu, J. Band offsets and heterostructures of two-dimensional semiconductors. *Appl. Phys. Lett.* **102**, 012111 (2013).

299. Fang, H. *et al.* Strong interlayer coupling in van der Waals heterostructures built from single-layer chalcogenides. *PNAS* **111**, 6198–6202 (2014).

300. Hong, X. *et al.* Ultrafast charge transfer in atomically thin MoS 2 /WS 2 heterostructures. *Nature Nanotechnology* **9**, 682–686 (2014).

301. Ceballos, F., Z. Bellus, M., Chiu, H.-Y. & Zhao, H. Probing charge transfer excitons in a MoSe 2 –WS 2 van der Waals heterostructure. *Nanoscale* **7**, 17523–17528 (2015).

302. Zhu, X. *et al.* Charge Transfer Excitons at van der Waals Interfaces. *J. Am. Chem. Soc.* **137**, 8313–8320 (2015).

303. Fu, Y. *et al.* Multicolor Heterostructures of Two-Dimensional Layered Halide Perovskites that Show Interlayer Energy Transfer. *J. Am. Chem. Soc.* **140**, 15675–15683 (2018).

304. Lin, D. *et al.* Unveiling hot carrier relaxation and carrier transport mechanisms in quasi-two-dimensional layered perovskites. *J. Mater. Chem. A* **8**, 25402–25410 (2020).
305. Liu, J., Leng, J., Wu, K., Zhang, J. & Jin, S. Observation of Internal Photoinduced Electron and Hole Separation in Hybrid Two-Dimentional Perovskite Films. *J. Am. Chem. Soc.* **139**, 1432–1435 (2017).
306. Zheng, K. *et al.* Inter-phase charge and energy transfer in Ruddlesden–Popper 2D perovskites: critical role of the spacing cations. *J. Mater. Chem. A* **6**, 6244–6250 (2018).
307. Shang, Q. *et al.* Unveiling Structurally Engineered Carrier Dynamics in Hybrid Quasi-Two-Dimensional Perovskite Thin Films toward Controllable Emission. *J. Phys. Chem. Lett.* **8**, 4431–4438 (2017).
308. Paritmongkol, W. *et al.* Synthetic Variation and Structural Trends in Layered Two-Dimensional Alkylammonium Lead Halide Perovskites. *Chem. Mater.* **31**, 5592–5607 (2019).
309. Pan, D. *et al.* Deterministic fabrication of arbitrary vertical heterostructures of two-dimensional Ruddlesden–Popper halide perovskites. *Nature Nanotechnology* 1–7 (2020) doi:10.1038/s41565-020-00802-2.
310. Rivera, P. *et al.* Observation of long-lived interlayer excitons in monolayer MoSe 2 –WSe 2 heterostructures. *Nature Communications* **6**, 1–6 (2015).
311. Bettis Homan, S. *et al.* Ultrafast Exciton Dissociation and Long-Lived Charge Separation in a Photovoltaic Pentacene–MoS2 van der Waals Heterojunction. *Nano Lett.* **17**, 164–169 (2017).
312. Zhang, J., Zhu, X., Wang, M. & Hu, B. Establishing charge-transfer excitons in 2D perovskite heterostructures. *Nature Communications* **11**, 2618 (2020).